Resonant Tunnelling Diode Epitaxial Wafer Design Manufacture and Characterisation

Mr. Michele Cito

Submitted in the fulfilment of the requirement for the Degree of Doctor of Philosophy

School of Engineering

College of science and engineering

University of Glasgow

May 2022

Abstract

Resonant tunnelling diodes realised using the AlAs/InGaAs lattice match to InP substrates have demonstrated promising performance as THz sources. The main limitations to deployment are imposed by the device output power, which is critically dependent on the structural quality of the epitaxial material. Future design and growth optimization require tools to characterize the thin RTD active region on different length scales and to create a link between design variables and device performance. This thesis reports a combined non-destructive characterisation scheme based on photoluminescence spectroscopy (PL), X-ray diffraction (XRD), and photoluminescence excitation (PLE) spectroscopy. The scheme improves the accuracy and reproducibility of all the RTD design parameters to provide accurate feedback for future epitaxy optimization both in R&D and in future manufacturing. A new PL technique is also proposed to investigate RTD structural imperfection on a length scale comparable with the RTD device mesa area, allowing an investigation into important growth imperfections affecting the device performance and reproducibility. Alternative RTD designs made by substituting the ternary InGaAs well with an InAs/GaAs superlattice are proposed and demonstrated in the last part of the thesis. Design criteria and simulations are reported and improvements in the structure epitaxial quality are highlighted by PL.

Table of contents

Acknowledgements

I would like to thank the following people who have helped me undertake this research:
My supervisor Prof. Richard Hogg, for his mentorship, encouragement, and patience;
Prof. Edward Wasige for his enthusiasm and support as director of the TeraApps project.
The European commission for this incredible international experience,
Prof Osamu Kojima for his kindness and help,
All the people in TeraApps project and partners organizations,
Toshikazu Mukai and the support form ROHM LTD.
The University Of Glasgow and all the members of the staff,
Dr. Razvan Baba and Dr. Matthew Steer for their contributions to my trainings and support,

Thanks to all my old friends, especially Giovanni M. for always being like a brother,
To my new friends, especially Davide C., for sharing his knowledge and for these 3 years of challenges.

To my family, for the unconditional love and support,
To Francesca, for the adventure we shared, and the ones that will come….

"The world isn't in your books and maps, it's out there."

— J.R.R. Tolkien, The Hobbit

"Think lightly of yourself and deeply of the world"

— Miyamoto Musashi, A Book of Five Rings

List of publications

Papers

"Micro-PL analysis of high current density resonant tunneling diodes for THz applications"
Cito Michele, Davide Cimbri, David Childs, Razvan Baba, B. A. Harrison, Adam Watt, T. Mukai, Edward Wasige, and Richard A. Hogg.
Applied Physics Letters 119, no. 7 (2021): 072102 https://doi.org/10.1063/5.0059339

"Photoluminescence excitation spectroscopy for structural and electronic characterization of resonant tunneling diodes for THz applications."
Cito Michele, Osamu Kojima, B. J. Stevens, T. Mukai, and Richard A. Hogg.
AIP Advances 11, no. 3 (2021): 035122.
https://doi.org/10.1063/5.0035394

Conference proceedings

SPIE PWEST2022, San Francisco CA, , United States
M. Cito, R. Baba, O. Kojima, B.J. Stevens, T. Mukai, R. A. Hogg
"PL and PLE characterization of high current density resonant tunnelling diodes for THz applications"
Proceedings of SPIE, "Terahertz, RF, Millimeter, and Submillimeter-Wave Technology and Applications XIV", DOI: 10.1117/12.2582781

SPIE Nanoscience + Engineering, 2021, San Diego, California, United States
M. Cito, R. Baba, D. Childs, B. A. Harrison, A. Watt, T. Mukai, R. A. Hogg
"Micro-photoluminescence characterization of structural disorder in resonant tunneling diodes for THz applications"
Proceedings of SPIE, Low-Dimensional Materials and Devices 2021; 118000I (2021)
DOI 10.1117/12.2594685

SPIE PWEST2021, San Francisco CA, United States
M. Cito, O. Kojima, B.J. Stevens, T. Mukai, R. A. Hogg

"Fitting of photoluminescence spectra for structural characterization of high current density resonant tunnelling diodes for THz applications "
Proceedings of SPIE, “Terahertz, RF, Millimeter, and Submillimeter-Wave Technology and Applications XIV”, DOI: 10.1117/12.2582781

List of abbreviations

AFM – atomic force microscopy
AlSb – Aluminium antimonide
CL – cathode luminescence
CMOS – complementary metal-oxide-semiconductor
CW- continuous wave
DB-QW – double barrier quantum well
DFG – difference frequency generation
FET – field effect transistor
GaAlInAs – Gallium aluminium indium arsenide
GaAs- Gallium arsenide
GaN- Gallium nitride
HEMT – high electron mobility transistor
HR-XRD- High resolution x-ray diffraction
InAlAs – Indium aluminium arsenide
InAs – Indium arsenide
InGaAs – Indium gallium arsenide
InP – Indium phosphide
InSb – Indium antimonide
LM – Lattice match
LT-PL – Low temperature photoluminescence spectroscopy
MBE – molecular beam epitaxy
MEE – migration enhanced epitaxy
Mid-IR – middle infra-red
ML – Mono layer
MMIC -Microwave monolithic integrated circuit
MOVPE – metal-organic vapour phase epitaxy
NA – Numerical aperture
NDR- Negative differential resistance
NLO – Nonlinear optics
PLE – Photoluminescence spectroscopy excitation
PVCR- peak to valley current ratio
QCL- quantum cascade laser
QW – quantum well
RHEED - Reflection high-energy electron diffraction
RTD – Resonant tunnelling diode
Rx- receiver
RF – Radio frequency
HBT – heterojunction bipolar transistor
SEM - scanning electron microscopy
SiGe- Silicon germanium
SL- Superlattice
T1, T2 – Type-I and Type-II transition energies
TEGa – triethylgallium
TEM - transmission electron microscopy
THz – Terahertz
Ti/Pi/Au - titanium/palladium/gold
TMAl - Trimethylaluminum
TMGa – trimethylgallium
TMIC – Terahertz monolithic integrated circuit
TMIn - Trimethylindium
Tx – Transmitter
UTC-PD - Uni-travelling carrier photo diode
VCSEL - vertical-cavity surface-emitting laser

Declaration

With the exception of the figures, where specified as being re-created after a [reference] in accordance to the license of the copyright holder, all work in this thesis was carried out by the author unless otherwise explicitly stated.

This project is part of TeraApps (Doctoral Training Network in Terahertz Technologies for Imaging, Radar and Communication Applications) and has received funding from the European Union's Horizon 2020 research and innovation program under the Marie Sklodowska−Curie Innovative Training Network (ITN) grant agreement No. 765426.

Chapter I: Introduction

This chapter starts with a description of the THz electromagnetic spectrum, the challenges in generating THz waves, and the current state-of-the-art in THz-sources, with a focus on electronic-based sources. Resonant tunnelling diode (RTD) technology is then introduced. This chapter details the RTD working principle, its manufacture, and its capabilities as a THz source.

Then, the chapter moves the attention to the epitaxial process and epitaxial wafer characterization techniques. These processes have critical importance in enhancing the RTD performance and for future optimization of this technology. There then follows a description of the current challenges and gaps in knowledge. The final part of the chapter briefly describes the thesis structure and its chapters.

This chapter is divided in 7 Sections.
Section 1 introduces the THz spectrum and briefly describes two approaches for signal generation: photonic or electronic.
Section 2 details the RTD working principle and its manufacture. The description includes the material system in use and the fabrication techniques.
Section 3 describes RTD-based THz oscillators and RTD device integration with the oscillator network and the antenna.
Section 4 briefly describes general concepts about the growth techniques in use for RTD epitaxial structures.
Section 5 details the importance of a wafer characterization methodology and summarise the state of the art in wafer characterization. General concepts about wafer characterization process are presented and characterization techniques are divided based on their destructive nature. The section focuses on the techniques in use in this PhD project.
Section 6 describes gaps in knowledge and the challenges to address to improve the RTD technology.
Section 7 concludes the chapter and details the thesis contents.

1.1 THz technologies: background and motivation

The THz region of the electromagnetic spectrum has a wavelength of 0.1-1mm. It lies at the boundary between electronic and photonic technologies, and consequently has historically limited solutions for practical sources and detectors, and for this reason is known as the "THz Gap"[1]. Figure 1.1 shows the frequency electromagnetic spectrum, the THz gap is highlighted by the green rectangle and lies between the electronic and photonic technologies in the range of frequency from 300GHz (sub-THz) and 10THz.

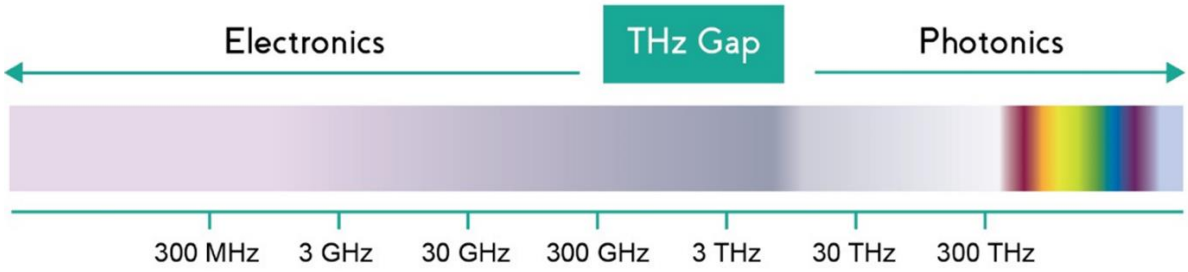

Figure 1.1 Schematic of the electromagnecti spectrum, and frequency ranges accessed by different technologies.

Bridging the THz gap has attracted great attention in recent years and researchers are working in all the complementary aspects of THz technologies (sources, detectors, applications) [2, 3]. THz generation is realized following two main approaches: photonic or electronic. Photonics involves a range of approaches from photoconductive switches and non-linear optics to direct generation in e.g., quantum cascade lasers (QCL). In the electronic approach, the THz radiation is usually generated by a diode or transistor-based oscillator, or by frequency multiplication. More details about both approaches are reported in the following section.

THz technologies find application in a wide range of fields like ultra-fast communications[4-7], biomedical and security imaging[1, 2]. Generally speaking, higher carrier frequencies imply wider modulation bandwidths and higher data-rates[8]. THz radiation is desirable for biomedical and security applications thanks to its non-ionising nature[9, 10], therefore no harmful chemical reactions are triggered. Additionally, strong absorption peaks due to water and other chemical elements (oxygen, hydrogen bonds) make THz diagnostic system very sensitive [9].

This thesis is focused on enhancing the power output and manufacturability of a single frequency source. This may be used in illumination or in wireless communications. In wireless communications, clear standards have been established in terms of requirements for the next generation of ultra-fast communication systems [11, 12]. The need for such high speed data transmiossion is driven by society, and the resultant Edholm's law of bandwidth[13], which predicts the doubling of data rate every 18 months. Following this trend, in the last two decades (2000-2020) we have seen an enormous evolution of mobile cellular networks, from the first generation (1G) to the fifth (5G). THz radiation (sub-THz) allows data rates of gigabytes per second for short-range wireless communications in the near future, and THz data rates in the further future. This can be achieved due to the wide bandwidth available at such a high frequency. The objective for the next decade is to push THz wireless communication to tens and hundreds of gigabytes per second. Current research in this direction is limited to experiments on communication links in a line-of-sight set-up. Misalignment between the source and detectors creates power loss. On this basis, electronic THz sources are not different compared to an optical communication system based on lasers or diodes. Researchers are investigating antennas in an array pattern and beam steering for the control of the irradiated power in space, that will contribute to overcoming the directional impediment imposed by misalignment between source and detectors and unlock broad area coverage. This will provide advantages offered by electronics microwave sources over those of optical laser sources.

Additional limitations are imposed by the power in output and by the atmospheric specific attenuation increasing the frequency[2, 12]. In illumination and free-space communications, the output signal is critically decreased by oxygen and humidity, especially in outdoors.

1.1.1 Photonics THz sources

Photonic THz sources may be based on the interaction of two lasers with a photoconductive device, and the process is known as photo-mixing [14, 15]. Input laser signals are generated by a pulse mode-locked laser source[5], or by an optical frequency comb generator (OFCG). In this second technique, the main element is a continuous-wave (CW) laser such as a tenable distributed feedback laser (DFB)[16, 17], vertical-cavity surface-emitting laser (VCSELs)[18], or a quantum cascade laser[7, 19, 20]. The system includes a phase modulator and a low-frequency local oscillator.

The photoconductive device for photo-mixing may be a uni-travelling-carrier photodiode (UTC-PD)[21, 22]. Indium phosphide (InP) based UTC-PDs have demonstrated signals up to 1.2THz at room temperature[4]. In terms of max radio frequency (RF) output power, 1.2mW were demonstrated at 300GHz[23]. Other approaches in THz wave generation include non-linear optics (NLO). Non-linear optical properties are generated in material under high light intensity [24], and are used to generate or manipulate THZ radiation[25]. As an example, non-linear QCL (NL-QCL) have mid infrared (mid-IR) active regions engineered to exhibit a large inter-subband nonlinear susceptibility[26]. THz generation may also be based on e.g. difference frequency generation (DFG) using closely spaced visible/NIR optical sources[22].

The inconveniences associated with the photonic approach are related to the complexity and cost of the systems. Discrete optical components are required in certain cases, making the systems bulky and introducing problems in integration and reliability. On the other hand, complex systems such as CW photo-mixers offer tuneability[14], a characteristic of critical importance in spectroscopy and sensing applications [27]. As already described in the previous section, optical sources are linked to communication line-of-sight and through waveguides (fibre optic cables). For wireless applications, the UTC-PD has demonstrated great possibilities with communication links up to 58 m depending on the modulation format [22]. However, such systems utilise many different opto-electronic device elements in order to generate the THz radiation. The main target of these wireless technologies is portable, consumable items, with the additional requirement of low power consumption. For the specific case of the UTC-PD, the TX apparatus includes an infrared laser source, an electro-optic phase modulator and a local oscillator. The carrier and the signal are modulated and directed to the UTC-PD. The modulated output radiation is then launched through the antenna. This example highlights the complexity of an optical THz source, and similar considerations are then applied to the receiver (RX) system.

1.1.2 Electronics THz sources

Transistor-based THz monolithic integrated circuits (TMICs) have demonstrated oscillation frequencies in the sub-THz (300GHz - 1THz) and above 1THz [28, 29]. Silicon complementary metal-oxide-semiconductor (CMOS) , field-effect transistor (FET)[28], and silicon germanium (SiGe) heterojunction bipolar transistors (HBT)[30] offer a maximum

cut-off frequency up to 450GHz[28] and 720GHz[30]. Better performances were obtained using InP-based HBTs, with double heterostructure HBTs and high electron mobility transistors demonstrating f_{max} (maximum unity power gain cut-off frequency) in the range 1-1.5THz[29, 31].

The inconvenience in implementing TMIC sources is in the complexity of the system and the low efficiency of DC-RF conversion [12]. TMIC systems include frequency multipliers, mixers and RF power amplifiers. These elements add to the complexity and cost of the system, with several issues related to the power efficiency and addition of noise.

Diodes based THz sources have been realized by tunnel transit-time (TUNNET) at 655GHz [32, 33], impact ionization avalanche transit time (IMPATT) diodes at 300GHz [34], and Gunn diodes 320GHz [35].

InP Gunn diodes operate based on harmonic power extraction, this method is not efficient and this impacts the device power [36]. TUNNETs are composed of a single barrier structure, in this topology of devices the capacitance reactance increases with frequency, limiting their performance[36].

Resonant tunnelling diodes (RTDs)[37] have demonstrated exceptional frequency performance in the last 10 years with highly attractive characteristics, placing them as key candidates to bridge the THz gap. Indeed, the RTD is the highest frequency semiconductor oscillator[6] with fundamental harmonics up to 1.98THz.

With respect to photonic sources, RTDs do not require external input lasers, extraneous optical components, modulators, and combiners. Similarly, by comparison to TMIC technology, RTDs are simpler to integrate and are also more compact.
More details will be discussed in the next sections.

1.2 RTD operation and manufacture

Resonant tunnelling diode are one-dimensional (1D) vertical transport unipolar two-terminal devices. This device has a non-linear I-V characteristic characterized by a negative differential resistance region (NDR). The NDR region is generated by the quantum

mechanical resonant tunnelling of electrons through the device.

The simplest RTD active region is composed of a double barrier quantum well structure (DBQW). An example of the band profile of an RTD structure is shown in figure 1.2A. The picture does not include considerations of the doping and room temperature operation is assumed. Starting from the left, the picture shows the emitter, the QW active region, and the collector. Green squares indicate the "Fermi sea" of electrons, while the red lines inside the QW mark the first and second quasi bound electron states.

The working principle is shown in the next series of picture (from A to D) and in the IV characteristic displayed in figure 1.2. Applying a bias to the structure the band profiles tilt/bend as shown in figure 1.2B. By increasing the bias the Fermi level reaches the first quasi bound states level and the electrons can flow from the emitter to the collector contact, and this is called the "resonant condition". Here the current reaches its maximum, and in the graph this point is labelled as "J_{PEAK}" with its respective bias point "V_{PEAK}". Further increasing the bias, the current starts to *drop* as the Fermi level and the e_1 are no longer aligned as shown in figure 1.2D. The negative differential resistance region (from point C to D) is indicated on the IV characteristic. Point D marks the valley point, with its respective J_{valley} and V_{valley} points.

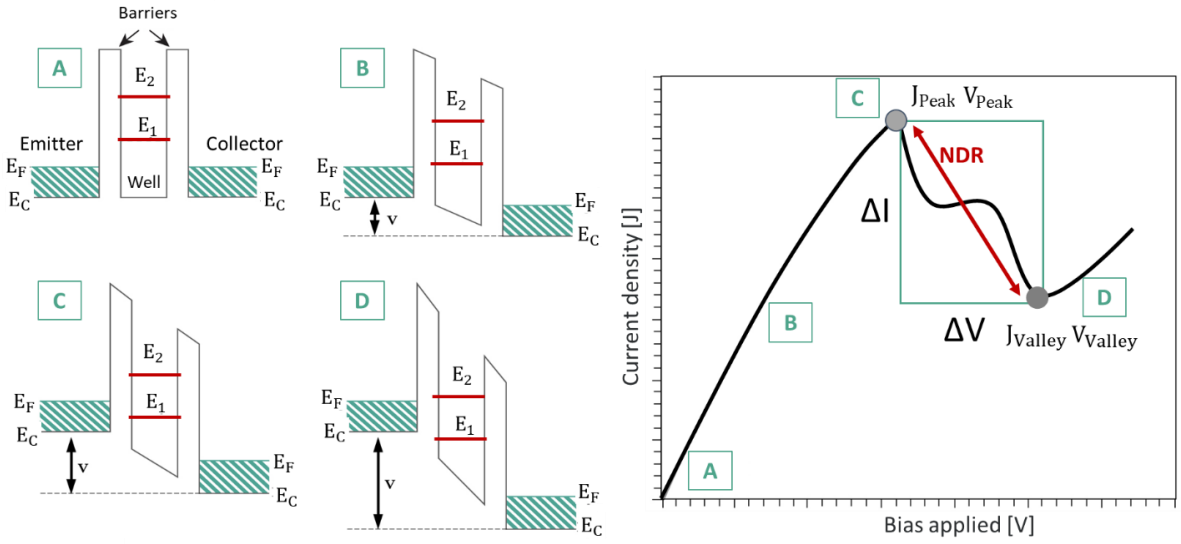

Figure 1.2 RTD working principle under an applied bias (A-B-C-D). The resonant condition is represented in C. The graph on the right side shows a typical RTD IV characteristic. The NDR region is highlighted in red. Peak and valley points are highlighted by the grey dots.

RTDs are characterized by several figures of merit (FOM) [38, 39], depending on the target frequency (and application), some FOM are more important than others. One FOM is defined as the theoretical maximum radio frequency power that can be extracted

from the RTD device, defined as $P_{RF} = \frac{3}{16} A \Delta J \Delta V$ [40] where "A" is the mesa area of the device. As RTD technology is mainly limited by the output power, this parameter is of critical importance in all applications.

The NDR region is described by $\Delta J = J_{PEAK} - J_{VALLEY}$ and by $\Delta V = V_{PEAK} - V_{VALLEY}$. Both these values have a direct impact on the P_{RF} as explained by the previous formula, this FOM contains a combination of all the most important figures of merit, but individual parameters remain important due to the following consideration. High J_{PEAK} is needed in high frequency application as more current indicates rapid electron tunnelling. Therefore, RTD designs for applications above 1THz are commonly indicated as "high J_{PEAK} designs".

J_{Valley} is associated with the RTD epitaxial quality, where interface and alloy scattering create and undesired increase of this value [41]. Epitaxial imperfections such as roughness at the AlAs barriers cause the broadening of the e_1 resonance level, which contributes to increasing J_{Valley}. This additionally creates an undesired extension of the NDR region (in voltage) and in self-heating. Other possible scattering contributions are represented by impurities (introduced by the dopants) and phonons. Additionally, scattering after the first barrier causes trapping of electrons in the QW, which subsequently tunnel incoherently [40]. This value is also dependent on J_{PEAK}, where more current density creates two main effects: (i) more scattering[41, 42], (ii) undesired tunnelling due to thermal effects[42]. Based on these considerations, the ΔI figure of merit gives several pieces of information.

V_{PEAK} indicates the bias required to reach the resonant condition and it is correlated to the first quasi bound state energy. A small V_{PEAK} is desirable to reduce the power consumption of the device. Determining the position of the first bound state is useful for future design optimization. Similar considerations to J_{Valley} are valid for V_{valley}, as it is correlated to the second bound state. To increase the output power the ideal condition is represented by a wide ΔI and a narrow ΔV. Due to current losses the output power is also increased by acting on the ΔV, especially in sub-THz designs where J_{PEAK} is usually lower with respect to full THz designs.

The peak to valley current ratio (PVCR), defined as $\frac{I_{Peak}}{I_{Valley}}$, also quantifies the quality of the device as it is the ratio between the peak current and the undesired valley current.

1.2.1 Device structure

Figure 1.3 shows the generic device and epitaxial structure, details about the material system will be discussed later in this section. From the bottom, the structure starts with a buffer layer deposited on the substrate. Subsequently, the first highly doped lattice match (LM) bulk layer (emitter) is deposited on which the bottom metal contact will be realized. The bulk material doping concentration is then reduced for the sub-emitter layer. This reduction helps in creating a ΔV in the IV characteristic. Then, the first spacer layer is deposited, consisting of un-doped bulk material. The DBQW is growth pseudo morphically on the LM spacer layer. The well material can be LM or not depending on the application. The growth continues with the deposition of the collector layer, similarly to that of the emitter. Some designs report an highly doped sub-collector layer to improve the high frequency operation by eliminating the depletion region[43, 44]. A LM or strained highly doped bulk layer concludes the growth sequence, on which the top contact will be realized.

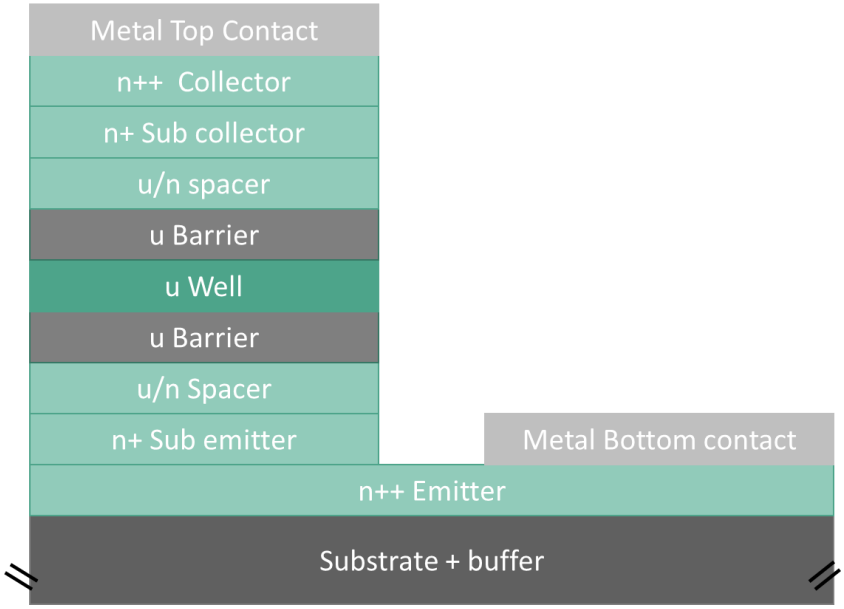

Figure 1.3 Schematic of typical RTD epitaxial structure. For convention the collector contact is reported on the top. Nomenclature: highly doped layer (n++), doped layers (n+), undoped layers (u). u/n indicates layer usually undoped.

Apart from the material system, variations in each layer thickness are found to vary widely in literature. Based on the application, barriers and well thickness are varied to the improve one figure merit whilst sacrificing others. Spacers are employed to avoid dopant diffusion

into the active region and to reduce the self-capacitance to improve the speed performance of the device[38, 45]. Symmetrical spacers are used to obtain symmetrical IV characteristic when the device is in forward or reverse bias[46]. To maximize performance, structures are designed for a forward bias and the emitter spacer is thinner with respect to the collector. The forward bias condition is obtained by connecting the negative bias to the emitter. To minimize self-heating, IV characteristics are obtained in reverse bias condition (negative bias applied to the collector). Common values reported in the literature are 20nm for the collector spacer and 2nm for the emitter spacer [6, 37, 47].

Dopant levels are optimized to reduce contact resistance and enhance current density. In ternary compounds such as InGaAs and InAlAs, the indium composition of the top contact layer is increased beyond the LM condition to reduce the band-gap and improve the top contact quality. Metal contacts are usually made by titanium/palladium/gold (Ti/Pd/Au).

1.2.3 Material system choices

Different material systems have been investigated to realize RTD structure and III-V materials have demonstrated very attractive characteristic for THz application [48]. In the active region, the critical parameters are the electron effective mass and the conduction band offset. Small effective mass leads to high electron mobility while high conduction band offsets improve the PVCR by suppressing thermally induced currents[47]. More detail about the determination of the conduction band offset will be discussed in chapter 3 [49]. In the bulk materials, a low specific contact resistance (ρ_c) is required to improve the current flow and minimize thermal effects (Joule heating). The GaAs/$Al_xGa_{1-x}As$ combination offers a $m^*= 0.067m_o$ and the $\Delta Ec=0.28$ eV. This material system was employed in early RTDs[50, 51]. The AlGaAs offers a $\rho_c = 10^{-6}\ \Omega cm^2$ which is high by comparison to other III-V materials.

The AlAs/InGaAs/InP material system demonstrates better performance as the effective mass is lower and the conduction band offset is higher with respect to the GaAs/AlGaAs combination ($m^*=0.044m_o$ and $\Delta Ec=0.65$ eV)[38]. Additionally, bulk InGaAs offers a lower contact resistance $\rho_c = 10^{-8}\ \Omega cm^2$.

The third material system investigated involves antimony (Sb) such as InAs/AlSb or InAs/GaSb. The effective mass of InAs is $0.023m_o$ and band offset $\Delta Ec=1.35$ eV (InAs/AlSb) are much better with respect to AlAs/InGaAs/InP [12]. Furthermore, the contact resistance is lower $\rho_c = (10^{-9}\ \Omega cm^2)$. The staggered Type-II conduction band offset offers additional advantages as it allows electrons to tunnel through the QW close to the valence band edge, reducing the current loss.

Recent results were obtained using the AlN/GaN material system. This material offers a large $\Delta Ec= 2.1$ eV, higher with respect to all the other material system described. On the other side, the electron effective mass is large $0.2\text{-}0.3m_o$ and poor ohmic contact $\rho_c = 10^{-6}$ Ωcm^2. Oscillation under the sub-THz at 200GHz were demonstrated[52], consequently this material system in not considered for RTD for THz sources[12].

From an epitaxial point of view, the first two material systems are preferable as InGaAs and AlGaAs can be grown lattice matched on their respective substrates (InP and GaAs). The well electronic properties can be tuned in the InGaAs material system by varying the indium mole fraction and well width. In the InAs/AlSb system, the use of binary compound eliminates the presence of ternary alloy scattering, but presents poor epitaxial quality due to the mismatch with respect to the substrate such as GaAs and GaSb. Furthermore, the lack of common Group II and Group V atoms makes epitaxy very challenging [53], more detail will be discussed in section 1.4.1. Furthermore, low intrinsic doping densities are difficult to achieve in this low-band-gap material.

Figure 1.4 shows the lattice constant vs band-gap map of the materials described above, while figure 1.5 shows the band offset vs lattice map using the InSb as a reference. The material system considered in this thesis is AlAs/InGaAs/InP. Using the epitaxial structure reported in figure 1.3 as a reference, the top collector contacts and made of strained InGaAs (indium mole fraction > 70%). Other than the QW and barriers, all the other layers are lattice match to the InP substrate.

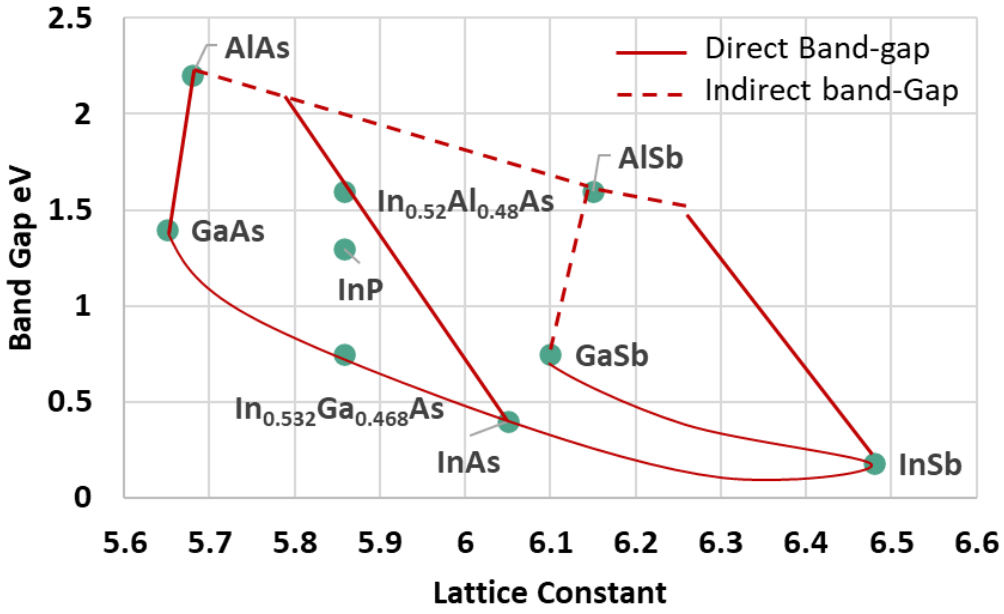

Figure 1.4 Lattice constant map of the material choices for RTD devices. Direct band-gap materials are connected by solid lines, inderect band-gap materials by dashed lines.

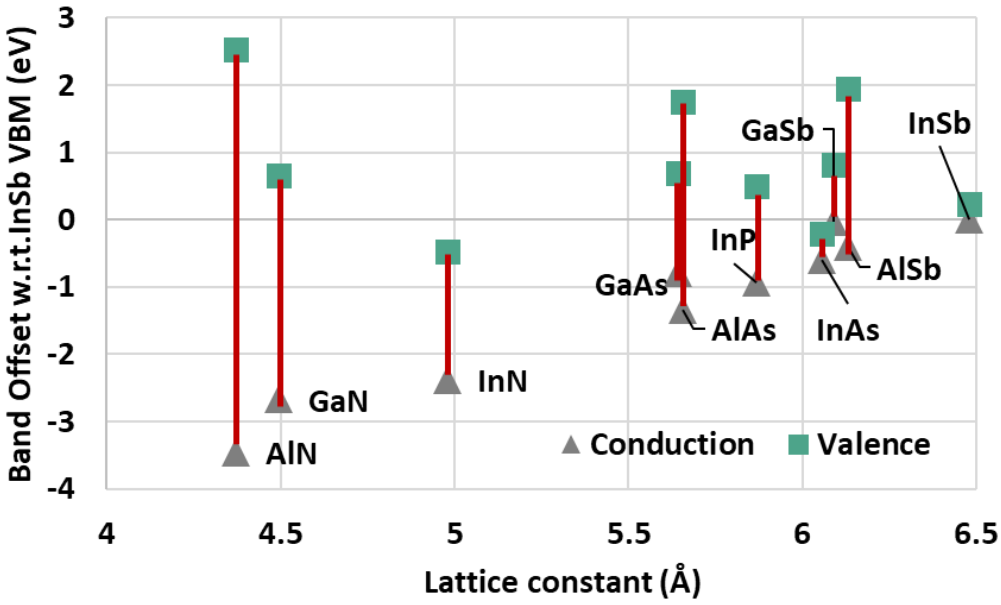

Figure 1.5 Band offset vs lattice constant map of the material involved in use for RTD.

1.2.4 Device structure

Figure 1.6 shows a schematic representation of an RTD realized using the air-bridge interconnection technology[54]. The air-bridge is widely used for high frequency devices to

reduce device capacitance[45], which is proportional to the device area[12]. Depending on the mesa area, the fabrication process involves standard i-line photolithography (micron scale) or electron-beam lithography (sub-micron scale).

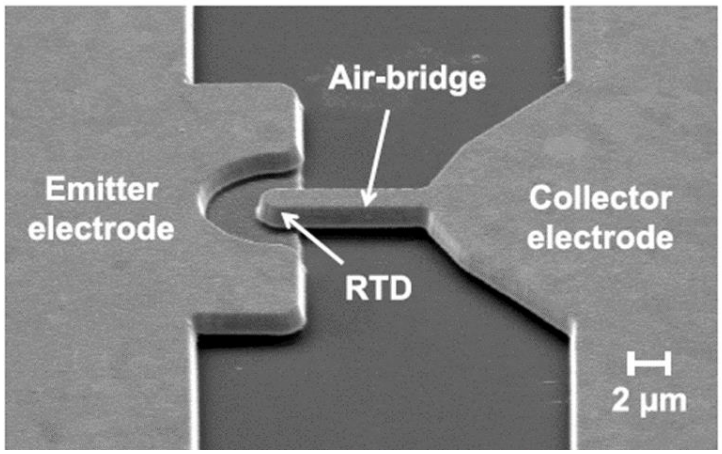

Figure 1.6 SEM of a dual pass air-bridge RTD device [41]. From the left: emitter contact, RTD structure, air-bridge, and collector contact.

1.3 RTD-based THz sources

1.3.1 History as THz sources

A GaAs/AlAs RTD-based oscillator was demonstrated for the first time by Sollner *et al.* in 1984[55], with a max frequency of 18GHz at 200K. The next important result was obtained by Brown *et al.* in 1991[56] with oscillation at 712 GHz at room temperature using the InAs/AlSb material system. The possible advantages of this material system were reported earlier in this chapter.

The InGaAs/AlAs/InP material system became popular from around 1988, not for the max frequency operation but thanks to high PVCR and ΔJ. A lattice matched InGaAs well, with an InAs sub-well increased the RTD performance thanks to low alloy scattering, high heterointerface quality and a good separation between the resonant levels. Several improvements were added during the years such as slot antennae and ring resonator [57], sheet resistors to suppress losses at low frequencies [58], and the use of arrays of devices [59].

The RTD design was improved by Suzuki *et al.* at Tokyo Institute of technology (TIT), they optimized the spacer thickness to 20nm and reduced the device mesa area to sub-micrometre.

They also abandoned lattice matching the well in favour of higher indium composition InGaAs. After that, they reported a graded emitter structure with thin barrier to reduce the electron transit time. Based on these improvement they obtained oscillation at 831GHz in 2009[60], 1.04 THz in 2010[37] and 1.45 THz in 2014[44]. Recently, the TIT research group reported the record oscillation frequency of 1.98THz[6]. The epitaxial structure utilised thin AlAs barriers of 3ML (0.879nm), a narrow well thickness of 2.5nm and a high indium composition, [In]=90%. They also added a GaAlInAs graded emitter which moves the emitter conduction band edge closer to the resonant state[12]. This reduces the bias required to reach the NDR region and therefore improve the DC-to-RF efficiency.

1.3.2 RTD oscillator system

The working principle in RTD-based oscillators follows the classical electronic one. Oscillators are composed of a resonant circuit and an active element. Under bias, the circuit internal noise generates an oscillation that is filtered by a resonant circuit (pass band filter), if the losses are compensated, a stable oscillating signal is obtained. In an NDR-based oscillator, as is the case for an RTD-based oscillator, the losses introduced by the circuit (Rs) are compensated by the device (-Rs) when it is biased in the NDR region. This condition is reached at the resonant frequency imposed by the passband filter, that defines the F_{MAX} of the RTD oscillator.

The RTD is coupled to an antenna to irradiate the RF signal. The antenna design depends on the frequency range, and in the THz range (≥ 300GHz) the most common on-chip antenna is the slot antenna [12]. The entire oscillator is realized in microwave monolithic integrated circuit (MMIC) technology and coupled with a silicon lens to irradiate the electromagnetic radiation. This is because the signal is radiated into the substrate and the Si-lens helps to extract and collimate the THz emission[54].
The oscillator network, the RTD device and the slot antenna, are realized on the same chip.

As an example, Figure 1.7 shows schematically a representation of the RTD oscillator used in [6] to reach the record frequency of 1.98THz.

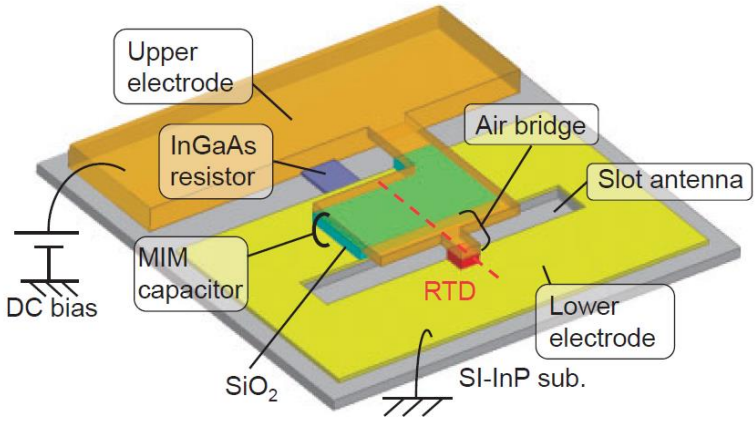

Figure 1.7 Schematic diagram of an RTD MMIC oscillator used to obtain 1.98THz emission [6]

1.4 Epitaxial Growth

This section briefly describes the two principal growth techniques employed for RTD growth, molecular beam epitaxy (MBE) and metal organic vapour phase epitaxy (MOVPE). High current density RTD structures were usually realized including a thin InAs sub-well to increase the equivalent well indium mole fraction to lower the first resonance state and increase the separation between the first and second states[61].

Due to the difficulties in growing the sub-well by MOVPE, MBE was preferred to grow RTDs[46]. Additionally, MBE is considered to offer better control in layer thickness and heterointerface abruptness in AlAs/InGaAs/InP with LM-InGaAs well. This is due to *in-situ* monitors such as reflection high-energy electron diffraction (RHEED). However, excellent RTD performance was later demonstrated by MOVPE in epitaxial structure substituting the LM-well and the sub-well with indium rich (80%) well [46, 47].

1.4.1 MBE and MOVPE

MBE is a growth technique where the semiconductor elements are heated to the point of effusion, and these liberated atoms are directed to the substrate in form of a thermal beam

from cells without any chemical change. The growth is realized in an ultra-high vacuum environment (~1E^{-9} Torr) on a heated substrate. This creates some limitations as the crystal quality depends on the level of the vacuum and the cleanness of the chamber. As a consequence, the manufacturing rate may therefore be low, due to steps required to prepare the reactor chamber, either from run-to-run, or due to maintenance where the chamber is opened to the atmosphere. Growth rates are of the order of the ~1 µm/h for bulk layers, which is reduced (expressed in terms of mono layers) to 1ML/sec for the QW layers (barriers and well).

This technique provides the advantages of *in-situ* characterization to monitor the state of the surface growth. Reflection high-energy electron diffraction (RHEED) is a technique where a soft X-ray beam is directed towards the substrate, this generates a diffraction pattern giving information about the surface, and the growth of individuals atomic layers.

Figure 1.8 shows a schematic of the main elements involved in the MBE growth.

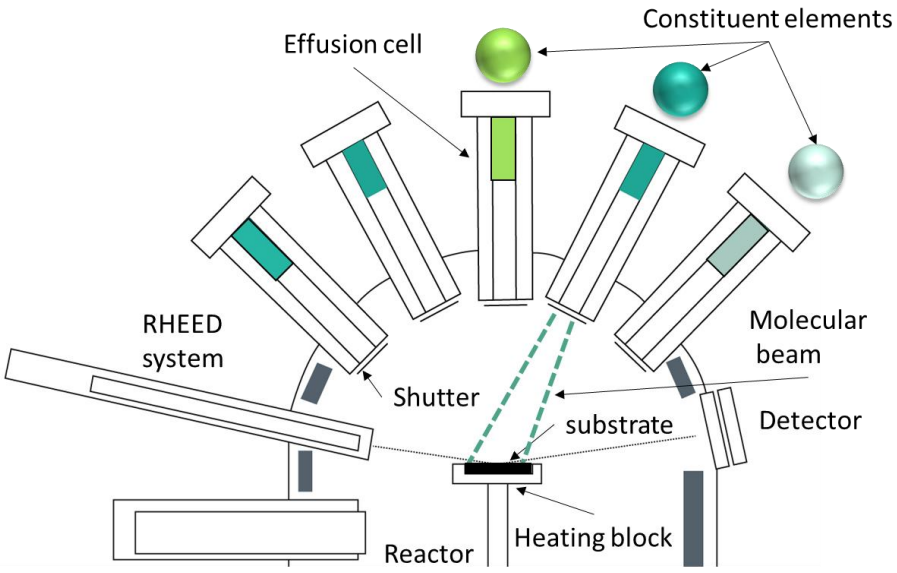

Figure 1.8 Schematic representation of the MBE reactor, and its main components.

Metal organic vapour phase epitaxy (MOVPE) is one of the most commercially employed techniques from compound semiconductors. In this growth technique, inorganic atoms (metals) are linked to organic radicals in a metal-organic molecules characterized by a weak bond energy. In the reactor, the metal-organic molecule is directed to a heated substrate,

where the temperature breaks the weak bond and the metallic atom remains on the substrate, while the gaseous organic atom is expelled from the chamber. To expel the undesired radicals, hydrogen is injected in the chamber as a carrier gas which quickly combines with the organic atoms when it is separated from the metallic ones. The reactor is designed to flow the gaseous compound from the top ("shower head") towards the reactor chamber. Wafers are on the bottom, and they rotate to ensure growth uniformity.

Precursors gases utilised are trimethylgallium (TMGa) and triethylgallium (TEGa) for the gallium. Trimethylaluminum (TMAl) for the aluminium, and trimethylindium (TMIn) for the indium. The first three are in liquid phase while the last one is solid. Each precursor is heated to reach a gaseous phase which generates a vapour pressure. The gaseous flow of the carrier gas (and hence reagent) is regulated in the reactor through a series of programmable valves.

This growth techniques suffers from two main disadvantages. The first one is related to the flow switching time. When growing thin layers (a few atoms thick) the switching rate is important to realise the desired, abrupt heterostructures. The second problem is the lack of in-situ characterization tools to control the growth rate in real time. A fundamental difference of the two techniques is that in MBE, rate of supply, and surface kinetics are separately controlled (cell temperature and substrate temperature), whilst in MOVPE they are linked, both being controlled by the substrate temperature.

Both techniques offer advantages and disadvantages, and the choice is mainly dependent on the application. MOVPE offers higher growth rates, ideal for bulk layers where the growth time of the overall structure may be reduced. MBE offers accurate control of the growth rate and fast switching, this in principle creates superior interfaces, especially in the growth of thin layers. Additional consideration needs to be made based on the material system in use, this topic will be addressed in chapter 5. In simple terms, antimonides are rarely grown by MOVPE, mainly due to the lack of a suitable precursor for high-quality films [53]. Phosphorous-containing structures are usually grown by MOVPE due to difficulties in cleaning the MBE chamber of phosphorous, which poses health and safety risks on opening the chamber if not properly addressed. For epitaxial regrowth of patterned structures, MOVPE is preferred as it is not high vacuum (dirty sample have limited impact), and automatically has hydrogen cleaning of the wafer due to the carrier gas.

It is worth mentioning the commercial differences between the growth methods. MOVPE reactor require shorter maintenance periods and provide high volume production. MBE requires longer times for growth campaigns, but material costs are lower. Large scale MOVPE reactors are commonly employed by the electronic and optoelectronic industries. The side effect relies in the disposal of the growth chamber exhaust due to its impact on the environment.

The QW perfection and uniformity are the critical aspect to minimize device variability and to make this technology commercially available. A complete characterization scheme is needed to investigate wafer uniformity and provide adequate feedback to the epitaxial process. Fluctuations in device performance are not only detrimental for the RTD device but for the entire oscillator. Apart from the output power, fluctuations in the QW have effects on the RTD equivalent capacitance, inductance, and conductance. These parameters determine the RF operational characteristics, and fluctuation in these values are detrimental for the oscillator design and for RTD-antenna impedance matching. It is clear that a reliable epitaxial and fabrication process is fundamental for future RTDs manufacture.

1.5 Epi-wafer characterization techniques

The development of a fast and non-destructive characterization method constitutes the starting point to resolve the problem presented in the previous section. Current wafer characterization state of the art relies on several technique classified in destructive and non-destructive. This section provides a summary of both types of characterization technique. This section will focus on the non-destructive characterization technique, with an emphasis on the ones used in this PhD project.

1.5.1 Destructive techniques

Destructive technique as so called because the process that is used to determine the physical properties will make the sample under test useless for future device fabrication process. On the other hand, these techniques are also known to be accurate and informative. High resolution transmission electron microscopy (HR-TEM) is the ultimate choice for layer thickness measurements. This technique is expensive, time consuming and requires sample preparation, which add a possible failure rate to the measurement. The high-quality images

(atomic resolution) provide information on the layer thickness and can also provide information about the layer composition (based on chemically-sensitive contrast differences[62]). Compositional information (mole fraction in the well) cannot be determined by standard TEM scans due to the lower resolution of the apparatus.

Electrochemical capacitance-voltage (e-CV) is a locally destructive technique where a crater is etched in the sample by an acid or alkali. During the etching, a known current flow in the sample, conductivity changes are measured to determine carrier density. This techniques was employed to determine doping densities in InGaAs and RTD structure [63, 64].

Compositional information can also be provided by secondary ion mass spectroscopy (SIMS). In this techniques ion are bombarded on the sample to etch a crater. In response, the sample ejects ions that can be analysed in a mass spectrometer. The output is a display of counts of a given atom at a given etch depth, from which the molar fraction is deduced if suitable standards exist. The accuracy is inferior as compared to HR-TEM, but higher with respect to standard TEM scans. Additionally, with respect to TEM, this technique has a simple and faster sample preparation (cleaving, cleaning and mounting).

1.5.2 Non-destructive techniques

1.5.2.1 Spectroscopic Techniques

Photoluminescence (PL) techniques are a group of technique employing a visible and near-visible pump wavelength. The laser excitation does not compromise the samples electrical or physical properties. The laser source is used to excite valence band electrons into higher energy conduction band states, and various radiative optical transitions are then produced and detected by the system. This radiative emission is linked to the physical and electronic characteristics of the sample under test (band gap, QW characteristic, doping). Experimental data are usually compared with simulation to extract more information. Photoluminescence spectroscopy and photoluminescence excitation spectroscopy (PLE) are part of the characterization scheme employed in this thesis. These techniques will be introduced and explained in detail in chapters 2 and 3 respectively.
Additional spectroscopic techniques are described as follows.

Photocurrent provides information about the absorption rather than emission. The sample is contacted with electrodes allowing for the application of an electric bias, while at the same time a suitable light source excites the sample with a given specific wavelength (energy) and power. The output displays the electrical response varying the incident light. In the case of there being no excitation energy dependence to the created photocurrent, the measured spectrum (additional current due to photo-excitation) is the same shape as the absorption spectrum (qualitative, not quantitative)[65].

Raman spectroscopy can measure the vibronic characteristics of the sample under test. The laser light interacts and scatters with the sample generating two scatter components. One as the same characteristic of the original laser source and it is filtered. The second as a wavelength that depends on the samples vibronic (phonon) characteristics. Several peaks are produced depending on the epitaxial layer structure and composition[66].

Cathodoluminescence spectroscopy is another powerful spectroscopy technique. Here the laser source is substituted by an electron gun. CL is based on a scanning electron microscopy apparatus. The electron beam has a nominal radius of ~10nm (depending on the current/voltage setting of the machine and the scattering on the sample), and for this reason this technique provides high spatial resolution as compared to a laser beam.
Similar to luminescence technique, the sample is excited and the response are optical radiative transmission associated to the material composition, band gap, or optical transition in QW structures[67, 68].

1.5.2.2 X-Ray diffractometry

X-Ray diffraction (XRD) and high-resolution diffraction (HR-XRD) are techniques employed in this thesis for the characterization of the physical structure of the RTD (i.e., providing no information directly about the electronic structure). XRD scans from RTD structure are reported through the thesis but a complete description of the apparatus is reported in this section.

Figure 1.9 shows a schematic representation of an XRD apparatus. From the left, the X-Ray tube generates the x-ray beam, which is reflected on a mirror and directed to a monochromator. The X-ray is directed on the sample block on the stage in the centre of the

picture. The sample holder is part of a goniometer, which can rotate, tilt and rock the specimen during the measurement. The diffraction beam generated by the sample is filtered by the slits and captured by the detector. In its simple form, the system is made to hit the sample with an angle ω and measure the diffraction with an angle 2θ. In this type of measurement ω=θ. To help the reader, this situation is represented by the dashed lines in the figure. Asymmetrical angles can be employed for advance measurement such as reciprocal space mapping[69, 70].

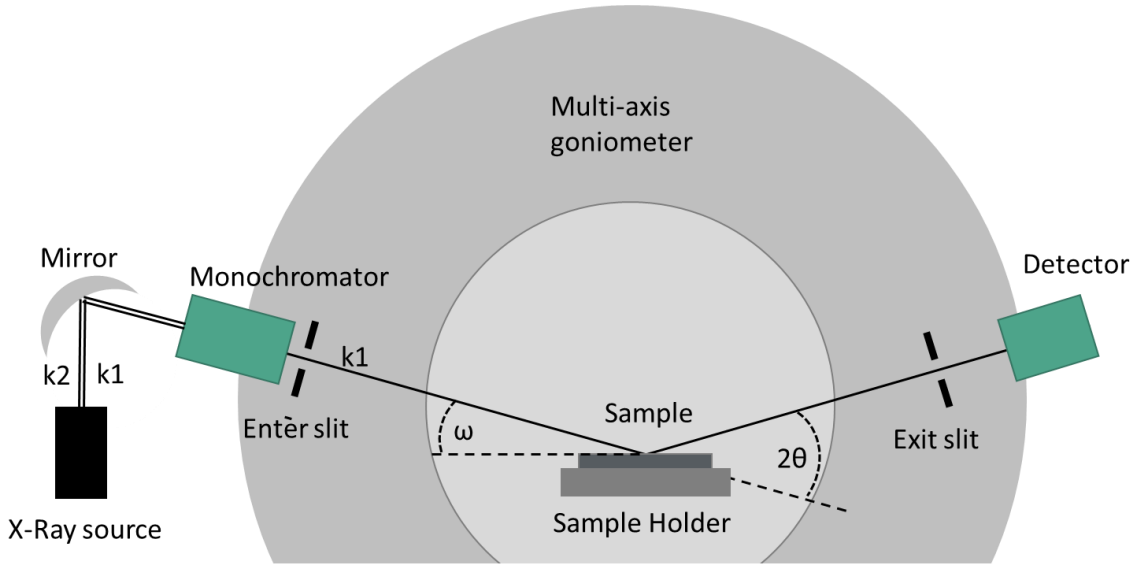

Figure 1.9 Schematic representation of XRD apparatus (Bruker D8 DISCOVER system). See text for a description of the elements.

X-rays are generated from a vacuum tube source; the emission is omnidirectional and is generated by bombardment of a copper target. The target is shielded with the exception of a circular aperture. The emission is collimated by a highly pure crystal and directed to a monochromator. The emission contains several wavelengths, as copper emits two main wavelengths $CuK_{\alpha 1}$ and $CuK_{\alpha 2}$ at ~0.1506 nm. The monochromator is composed of another crystal, upon which the beam is diffracted two or more times to filter the CuK1 component. One difference between and XRD and HR-XRD scans is the number of times the X-ray is diffracted within this crystal, (=4 for HR-XRD). Other differences are in the purity of the source and in the sensitivity of the detector. These improvements have a high impact on the cost and maintenance of the apparatus.

Entry and exit slits are selected to limit the number of scattered electrons entering the detector. Narrow slits are used to filter the electron entering the detector with angle closer to the $\omega-2\theta$. Wider slits allow more diffracted electron to enter the detector. The first case increases the accuracy of the scans reducing the S/N ratio, while the second increases the intensity but introduces more noise. During the measurement the stage rotates, and the X-ray scan plots the number of electrons as function of the angle.

X-ray propagation is highly deterministic, and several types of simulation software are available with minimum differences. X-ray rocking curve simulation is an important tool to support experimental data analysis. Jordan valley rocking curve dynamical simulation (JV-RADS) is used in this thesis to fit the experimental rocking curve and extrapolate the RTD layer thickness and the indium mole fraction.

1.6 Gaps in knowledge

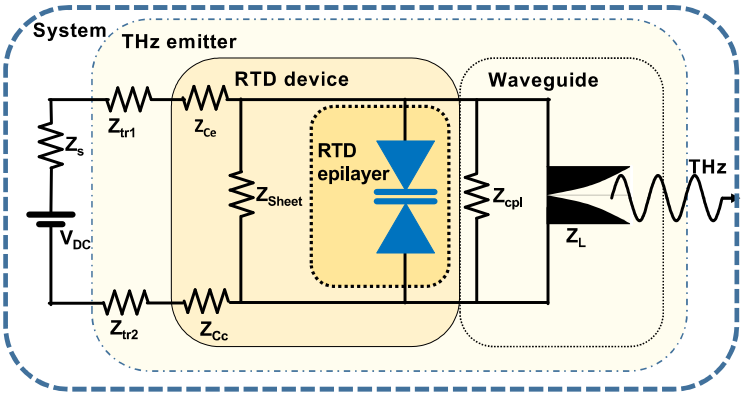

Figure 1.10 RTD-based THz source system schematic from[39]. Z are complex impedances: Z_{Sheet} caused by the mesa fabrication, Z_C by the collector and emitter contact, Z_{CPL} is the antenna coupler and Z_L the load from antenna itself, Z_{TR} includes impedance from traces, module and packaging of the system, Z_S series resistance of the DC supply.

Figure 1.10 shows a schematic of the RTD oscillator system to highlight all the sub-section that contribute to the THz wave generation. The RTD (RTD epilayer) is the core element, the RTD device is represented by the RTD epilayer plus the impedances that characterize the device (see caption for nomenclature details). On a higher level, the THz emitter schematic combines the RTD device with the waveguide sub-section, where ZL represent the antenna and its corresponding impedance. The overall system includes the DC supply and the series impedance. Each element in the schematic needs optimization to achieve

impedance matching to maximize DC-to-RF power conversion but the RTD epilayer/device remains the critical section to improve, and it is the subject of this thesis.

As previously explained, the RTD RF power depends on the ratio ΔIΔV, and maximizing both these factors (ΔI *and* ΔV) presents a challenge and requires facing several trade-offs. QW engineering is fundamental for this goal, but a clear and unambiguous link between the RTD epitaxial variables and the corresponding IV characteristic is not yet established[71]. Simulations provided limited information[72], especially for the case of high J_{PEAK} designs. Strain effects[39], the band-offset[49], and the epitaxial perfection[41, 73] play a crucial role in modifying the expected IV characteristic. Careful investigation is needed to improve the understanding and control over these variables.

Concerning the epitaxial perfection, new advanced designs are needed to address specific issues related to the material system in use and/or the growth process itself. Additionally, new epitaxial approaches are required to first improve the RTD state-of-the-art and consequently the repeatability and the manufacture of the overall MMIC structure. The last step regards the transition to a high-volume regime.

1.6.1 Non-destructive characterization schemes

A complete wafer characterization scheme is important to compare the simulated/designed wafer parameters with the real ones. This needs to be done in order to provide accurate feedback to the epitaxial process. In an attempt to maximize the RTD performance, the ability to discriminate which combination of design variables is best (e.g., compositions, thicknesses, doping) cannot be done based on the nominal (design) wafer parameters. Additionally, a clear link between the wafer properties (electrical and physical) and the device performance has not been established at the time of writing.

As explained in the previous section, the information provided during epitaxial growth are limited (MBE) or essentially zero (MOVPE). An accurate post-growth characterization is need when the structure is composed by such thin layers. The RTD state of the art presented in section 1.2 highlighted how high performance RTDs are composed by thin barriers and narrow, highly strained quantum wells. Destructive characterization techniques are expensive, produce material waste and are time consuming. Despite the accuracy they offer,

a single fit-for-purpose characterization technique does not exist, and a combination of techniques is always required to completely characterize the structure (doping, layer thicknesses, mole fraction), which increases the overall characterization time and the material wasted.

A characterization scheme can be realized using non-destructive characterization techniques, with several advantages in term of cost and time. A combination of X-Ray and PL was described by Baba *et al.* in [74] with an adequate level of accuracy. RTD structures have characteristics not entirely compatible with PL characterization. Multiple PL peaks originate from the QW and their deconvolution makes the analysis difficult. A suitable deconvolution process needs to be developed to improve the PL analysis and also to enable an in-depth characterization of the multiple peak origins.

1.6.2 Micron scale characterization

Wafer properties are known to vary across the wafer surface with fluctuations of thicknesses of a few percent being possible. On a macro scale, fluctuations may be not strong enough to impact the device reliability. Complications occur with the device mesa moves from a micron to a sub-micron scale. Section 1.3 highlighted how the RTD device performance is affected by the mesa area. Mesa areas under $1\mu m^2$ are required to reduce the RTD intrinsic capacitance in order to improve the maximum operational frequency. Consequently, micron scale characterization is needed to further explore the wafer characteristics and their fluctuation around the chip areas. Limitation here are imposed by the spatial resolution of some characterization techniques. Photoluminescence techniques are often limited by the laser spot size, usually around $\sim 100\mu m^2$ in typical wafer mapping systems. Techniques like CL or near field optical microscopy (which employ an optical fiber as a probe) are valid candidates for high spatial resolution but are inconvenient in terms of cost and the complexity of the system. An improved PL system will be the ideal solution for a cost effective and fast characterization scheme in the micron-scale.

1.6.3 New epitaxial designs and growth techniques

A brief RTD road map of the AlAs/InGaAs/InP material system was reported in section 1.3. In the last 20 years the max operational frequency moved from few GHz to 1.98THz. This

important result was obtained thanks to improvements in the RTD design and in the quality of the epitaxial processes. The RTD THz capabilities are well demonstrated now, but the lack of output power remains. To overcome this problem, new epitaxial designs need to be explored outside the standard barrier/ternary-compound/barrier scheme. Progress in crystal growth has opened the road to layer thicknesses near one atomic sheet (0.293 nm). Superlattice structures, based on the repetition of layer of different material, may represent a valid substitution of the well made by ternary compounds.

1.7 Thesis content

This first chapter describes RTD technology (from the device to the THz-source) and has set the background for the next chapters. General concepts about the epitaxial growth processes and wafer characterization techniques were also presented. Each of the following chapters introduces a characterization technique and/or address a specific growth imperfection. The thesis is composed of self-contained chapters.

Chapter 2 details the macroscopic PL characterization (spatial resolution >> RTD mesa size) of RTD epitaxial structure. The first part describes the results obtained in recent years in improving the quality and the quantity of information detectable by macroscopic PL. The chapter also reports on RTD epitaxial imperfection and their impact on the PL characterization. A PL line shape fitting methodology is presented to deconvolute the PL spectra [75]. This allows the analysis of the single peak in the spectra for the assessment of the quasi-bound state energies. The line shape fitting is presented together with the simulation suite used to support the characterization.

Chapter 3 describes PLE spectroscopy applied to epi-wafer characterisation [49] performed at the University of Kobe as part of an academic secondment. This technique is used for detecting radiative transition associated to the second quasi bound states (e_2-hh_2). The observation of these transitions allows the conduction band offset and the second resonant state energy to be determined for the first time for this class of device. The chapter describes the integration of PLE in the wafer characterization scheme based on XRD and PL. Two RTD designs are described in detail. PLE requires a careful choice of the energy detection range in the PL spectra, and results from chapter 2 are applied to obtain unambiguous results.

The chapter also discusses possible future improvements to this novel characterization scheme.

Chapter 4 changes the characterization spatial resolution scale. Previous chapters (and indeed all other work world-wide) have focused on a wafer-level and a macro scale characterization of RTD epitaxial structure. Chapter 4 moves the attention to the micron-scale, a length scale directly comparable with the RTD mesa area. The chapter describes in detail the epitaxial imperfection introduced by the growth process, with an emphasis on the effect of strain relaxation in high indium content QWs. Micron scale resolution is achieved by reducing the PL laser spot size, and detection area, utilizing photomasks. Fluctuations in the PL line shape are linked to epitaxial imperfection by considering the QW strain condition. Strain equations are applied to quantify the stress in the QW and its limits. The chapter shows a correlation between mesa-area epitaxial imperfection and the device reproducibility, by analyzing the IV characteristics obtained from 3 series of devices manufactured from this epitaxial material.

Chapter 5 compares non-destructive characterization data from nominally identical epitaxial structures grown by MBE and MOVPE. It goes on to investigates a new epitaxial designs utilizing advanced growth techniques. The chapter begins with a description of the differences between MBE and MOVPE growth processes, with an emphasis on the epitaxial imperfections caused by alloy broadening. This chapter proposes and demonstrates the substitution of the InGaAs material that constitutes the QW with InAs and GaAs layers in a novel superlattice structure. The chapter reports simulation of the band profile and strain conditions of this superlattice as part of the design process. The epitaxial wafer characterization is performed by XRD and PL, and indicates significantly enhanced uniformity as compared to standard MBE and MOVPE processes. Preliminary results on device performance are also presented.

Chapter 6 summarise the results obtained in this project and discusses possible improvements in epitaxial perfection, characterization techniques and RTD structure design. As RTD scaling is introducing more challenges, a method to characterize the QW thin barriers is proposed to limit error in the characterization.

Chapter II: Optical spectroscopy of resonant tunnelling diode epitaxial layers

This chapter describes RTD wafer characterization by low-temperature photoluminescence spectroscopy. I show how this non-destructive technique can be used to determine both the physical and electrical properties of the thin RTD active region. Careful line shape fitting is employed that incorporates the luminescence from highly doped collector and emitter layers, along with an improved simulation method for the first time. This analysis allows us to understand the extent of mono-layer fluctuations of the epitaxial material, increasing the quality of the feedback for next growth runs. This insight provides a new tool in the assessment of perfection in the RTD active region, with attractive application for volume manufacture. The line shape-fitting procedure detailed here was reported in[75].

This chapter is divided into 5 sections.
In the first part of the chapter, the PL technique is presented with a description of the advantages and disadvantages offered by luminescence characterisation techniques.
The second part describes the PL set-up employed in my PhD and its working principle. The third part describes PL applied to RTD wafers. A brief description of the challenges addressed in the past is presented, then the discussion moves to the improvements developed during my PhD.
The fourth part details the process developed to resolve the PL spectra. A set of rules are presented to fit the PL spectra line shape to increase the accuracy of the characterization. The last section summarises the improvements in PL characterisation presented in the chapter and highlights future challenges in luminescence techniques.

2.1 Low-temperature PL

Photoluminescence spectroscopy is an optical non-destructive characterization technique that uses a light source to excite the sample under test, and the detection of the optical transitions from semiconductor materials. A schematic representation of the process is presented in figure 2.1(A-B-C). A photon is absorbed, exciting electrons in the valence band to higher available electronic states in the conduction band (figure 2.1 A). For photon

energies much larger than the band-gap, hot carries are produced that relax to their respective band-edges. When the carriers recombine, (figure 2.1B), the electron and hole annihilate (the electron returns to the valence band), and a photon is emitted (figure 2.1C). This radiative emission is detected and used to characterize the physical and electrical properties of the structure.

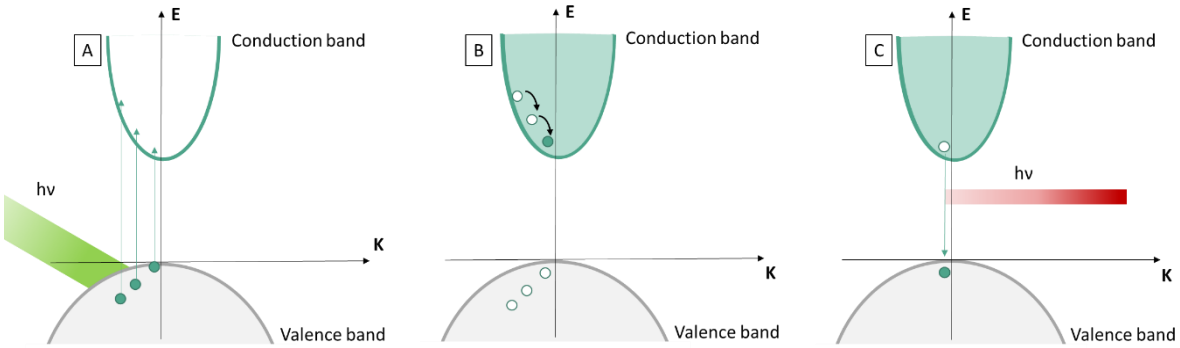

Figure 2.1 Schematic energy diagram of the PL radiative absorption/emission. (A) Laser excitation and electron transition through higher energy states, (B) Intraband transition to the minimum of the conduction band, (C) transition back to the valence band and release of the absorbed energy through photons.

This characterization technique is fast and is non-destructive, so sample preparation is not required. The main disadvantage is that the PL signal is weak and broad at room temperature, which adds the need for a cryostat, and operation at low temperature. Figure 2.2 illustrates this, showing representative temperature-dependent PL spectra obtained from a test structure in the range 300-15K. Meaningful information is only obtained as we approach 0K, and little information is observed at room temperature to due to thermal broadening and non-radiative recombination of carriers, reducing the PL intensity.

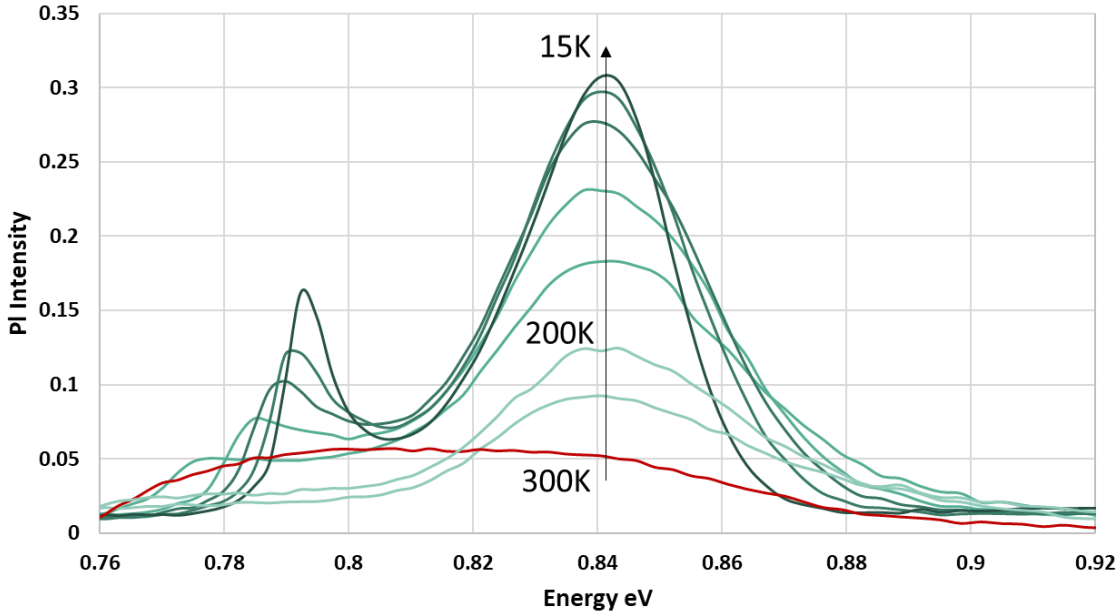

Figure 2.2 Temperature-dependent PL spectra of a typical RTD structure.

PL is uninformative at room temperature, starting from the bottom of figure 2.2 we observe a broad emission at 300K (red curve), which starts to be resolved to two different emissions after 200K. As we continue reducing the temperature, the quantum efficiency increases as nonradiative processes are suppressed [76], two peaks are then resolved at T=15K, the first one at 0.795eV and the second one at 0.84eV.

Low-temperature PL spectroscopy has previously been shown to be a powerful technique to characterize RTDs. PL was successfully employed to characterize the doping concentration[64], and the QW characteristics [63] of high current density RTD wafers. PL was also employed to determine charge accumulation in the RTD device as a function of the applied bias [77]. From this point to the end of the thesis, the term PL will be used to indicate photoluminescence spectroscopy performed at low temperatures (range 4-15 K).

2.2 PL set-up

Figure 2.3 shows a schematic representation of the PL apparatus used during my PhD. Starting from the bottom right corner, the laser beam (532nm diode pumped solid state laser) is reflected by mirrors 1 and 2 and directed to the beam expander to ensure a collimated beam is presented to the lenses within the system. In more detail, the goal is to direct the "expanded" laser light to mirror 3, which reflects the light to the collimator. The expander

assures the laser beam travels with a constant planar wavefront through the PL system. The light output from the laser has a curve wavefront, and this may create power loss at the end of the optical path. The laser passes through two sets of neutral density filters employed to vary the absorption and allow power-dependent measurements to be performed. The first dichroic mirror stops possible laser back-reflection to the source (which may result in noise and instability of the laser source). The second dichroic mirror combines the laser with the blue light from the LED. The LED light is used to illuminate the sample during the alignment of the laser and focus on the sample. The third dichroic mirror reflects the combined green and blue light to the collimator. The beam expander described earlier, assures the light is aligned with the collimator lens. The ideal condition is represented by a laser spot size equal to the lens aperture, where all the laser power is collimated to the sample. The position of the collimator can be varied vertically to focus the laser beam on the sample and improve the PL intensity from the system. This concludes the delivery of the laser light in this first path.

The collimator collects the sample PL response and the reflected blue and green beam and directs them to the return path. The mirror after the collimator reflects the blue light to the camera to observe the sample. The green excitation light is filtered by a green blocking filter positioned before the camera. The laser beam and the PL signal are directed to the dichroic mirrors, here the green pump light is filtered by the first mirror, and again by the second one (high rejection to green). The two dichroic mirrors in the PL path must be parallel in order to shift the beam back into the centre of the tube for transmission to the monochromator. This is required because each mirror introduces a shift in the beam, the parallel position assures that the first shift is corrected by the second mirror. The PL emission is free to pass through this path and reach the top mirror (parabolic mirror) that focuses the PL signal on the slits of the monochromator. The role of the slits is to control the size and position of the signal entering the monochromator, as the beam needs to be parallel to insure perfect aliment with the optics inside the monochromator. The same is true for the exit slit that allows the signal to hit the detector. The monochromator has the role to produce in output a single spectral component from the multi-wavelength input signal. To this end, a series of mirrors and dispersive grating are employed to separate the desired wavelength component from the other and to direct it through the detector. The dispersion element takes the multi-wavelength signal and reflects each wavelength differently in space as the angles are dependent upon the wavelength. This process spatially separates the component and isolates the wavelength of

choice, which is directed through the output slit and to the detector. All the other components are directed on the edge of the slits or inside the walls of the monochromator, so they are all blocked. The process is automatically controlled by software and servomotor to scan and measure the output signal intensity varying the detection wavelength. For the measurement reported in this thesis, the monochromator is a double-grating Bentham DMc150 and the detector is an InGaAs transimpedance photodetector by Thorlabs for the detection range 1100-1700nm. Si detectors may be used for the range 300-1100nm. An additional long-pass filter can be added before the monochromator to further eliminate spectral components from the pump laser.

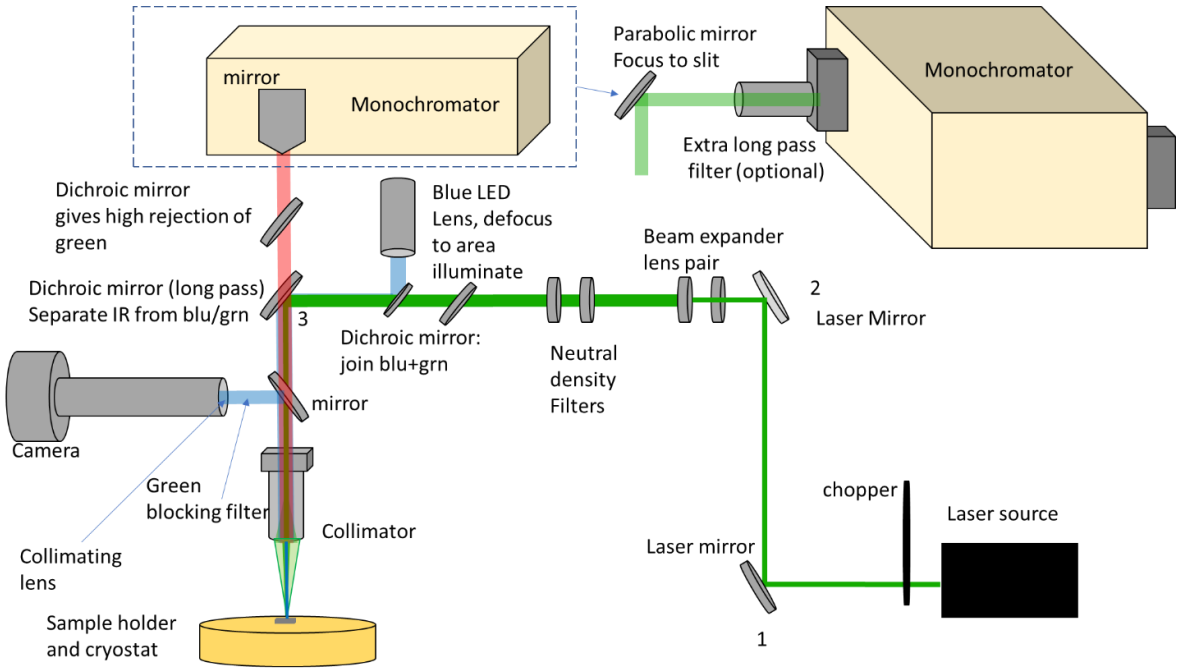

Figure 2.3 Schematic representation of the PL set-up indicating key components.

2.3 PL on RTD structures

This section introduces the basic RTD epitaxial structure to indicate which parameter we can characterize by PL. Key issues introduced by variations of structure introduced in the growth process and by the design are highlighted. Figure 2.4(A) shows a typical high J_{PEAK} RTD structure indicating the material system and the doping profile. Starting from the bottom

(substrate, dark grey), after an additional InP buffer, the growth continues with 400 nm highly n-doped $In_{0.53}Ga_{0.47}As$ ($2x10^{19}$ cm^{-3} Si) that constitutes the lower contact. A 20 nm n-doped $In_{0.53}Ga_{0.47}As$ ($3x10^{18}$ cm^{-3} Si) emitter layer is then deposited, followed by a 2 nm $In_{0.53}Ga_{0.47}As$ spacer layer. An InGaAs quantum well is formed between two 1.1 nm AlAs barriers (grey). On the collector side, a 20 nm $In_{0.53}Ga_{0.47}As$ spacer layer is grown with a 25 nm $In_{0.53}Ga_{0.47}As$ ($3x10^{18}$ cm^{-3} Si) collector layer. The epitaxy is terminated with 15 nm n-doped $In_{0.53}Ga_{0.47}As$ ($2x10^{19}$ cm^{-3} Si), and an 8 nm $In_{0.80}Ga_{0.20}As$ ($2x10^{19}$ cm^{-3} Si) (light grey) contact layer. QW parameter will be usually described in terms of monolayers (ML), 1ML=0.293 Å. For characterization purposes only, an inactive copy-QW is added at the bottom of the epitaxial structure. More details will be presented in the next chapter.

A

8nm	$In_xGa_{1-x}As$	$2{\cdot}10^{19}$
15 nm	LM InGaAs	$3{\cdot}10^{19}$
25 nm		$3{\cdot}10^{18}$
20 nm		-
4ML	AlAs	-
15 ML	$In_{0.x}Ga_{1-x}As$	-
4ML	AlAs	-
2 nm	LM InGaAs	-
20nm		$3{\cdot}10^{18}$
400 nm		$2{\cdot}10^{19}$
InP		

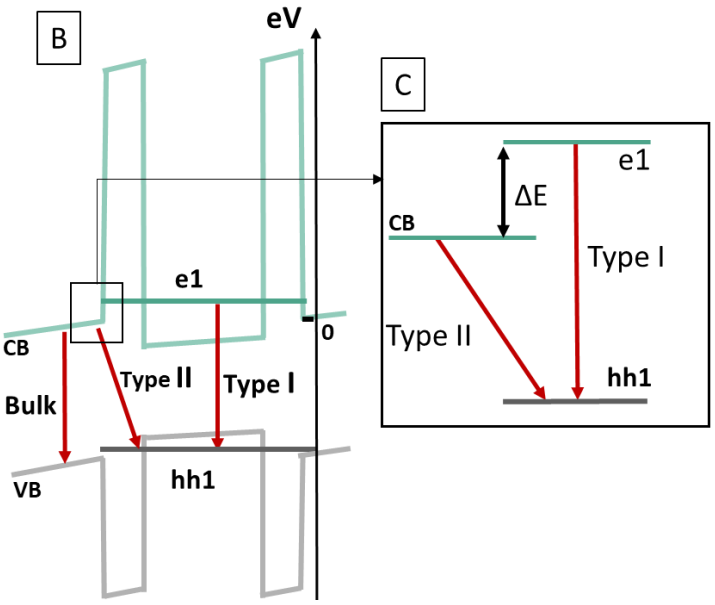

Figure 2.4 (A) RTD epitaxial structure and doping concentration, (B) RTD active region band profile, (C) Focus on the E1 energy state derived by the Type-I and Type-II emission energy difference.

The presented design has a highly doped collector and emitter which makes PL emission from the QW unfavourable[63]. The InGaAs material suffers from strong non-radiative effects caused by surface states and surface recombination[78]. The low-temperature characterization partially overcomes these issues where non-radiative emission such as surface recombination are minimized. The PL characterization of RTD wafers is based on the 3 main optical transitions shown schematically in the band profile in figure 2.4B. The conduction and the valence bands (Γ) are indicated in green and grey respectively. The

AlAs/InGaAs has a large Γ – X separation, the figure shows the band maximum at the Γ point. The schematic shows the band profile associated to the QW and the asymmetric spacer layers only, as indicated by figure 2.4A. The band curvature is representative of the effect introduced by the doping in modifying the band shape. Figures are intended to be schematic, but the energies reported are obtained by self-consistently simulating the whole region of the active region (spacer layers and doped layers), more details will be reported in section 2.3.3. The first quasi bound states e_1 and hh_1 are indicated by the coloured horizontal lines. Starting from the left, the first optical transition is denoted as "Bulk" and is due to the lattice match (LM) InGaAs bulk conduction and valence bands. The Type-II transition is due to electrons in the bulk conduction band recombining with the first heavy-hole (hh_1) state in the QW[79]. The Type-I transition is due to the first quasi bound state e_1 with the hh_1 state. Transitions energies are directly measured by PL and they are used to "indirectly" determine the position of the e_1 state, given by the difference Type-I -Type-II as described in figure 2.4(C) and marked by ΔE. The control and engineering of the e_1 state energy is essential for the RTD operation. Knowing its position in the band profile gives information about the bias required to reach the resonant condition[80] so it is a key design parameter.

2.3.1 Origin of the QW radiative transitions

Further observation of the schematic in figure 2.4 highlights of the RTD structure is not symmetric as the emitter and the collector spacer are 2nm and 20nm, respectively. This asymmetry together with the highly doped layers create an electrostatic potential in the collector region. A high electron density is present within the QW without applying any bias to the structure due to the diffusion of carriers from the highly doped layers. The Type-I recombination that due to e_1 and the hh_1 states originates from the recombination between photo-generated holes and the electrons in the QW.

The Type-II recombination is due to recombination across a Type-II band alignment[79], this happens when the band gaps of two materials present a partial overlap. High current density RTD active structures are constituted of very thin barriers, and photo-excited electrons can move outside the QW thanks to the low dwell time, while the holes are trapped in the QW valence band due to the discontinuity between the LM-InGaAs and the QW. The radiative recombination takes place between the electron in the LM-InGaAs and the holes trapped in the QW.

2.3.2 Bulk crystal perfection and doping concentration

The LM-InGaAs bulk crystal perfection is fundamental for the structural stability of the RTD[81], especially in the case of a high J_{PEAK} design where the bulk layers constitute the base material for the epitaxy of highly strained QWs. As previously reported in figure 2.4B, the bulk transition is associated with the LM-InGaAs bandgap. Any fluctuation in respect to the lattice matching condition given by a [In]=0.532 has an impact on the peak energy and shape. For a perfect LM-InGaAs, the nominal bandgap energy is 0.815 eV at 15K, observed fluctuation from this value may be caused by several factors: poor thermal bonding, strain effects, wrong mole fraction or an improperly calibrated PL system.

The presence of strain may locally affect the shape of the valence band orbitals, and thus the bandgap [82]. A more accurate analysis of the mole fraction can be obtained by combining the PL with an HR-XRD scan, which eliminates system-related uncertainty and increases the overall accuracy. The quality of the growth is assessed by looking at the shape of the bulk peak and at its full wave at half maximum (FWHM). Previous works [83] demonstrated how the FWHM of the bulk peak is dependent on compositional fluctuation ([In]). Figure 2.5 shows PL spectra from two different RTD samples, focussing on the spectral region where a signal from the bulk InGaAs is observed. This bulk-peak sits on top of wider spectral features due to the QWs. In figure 2.5A (Sample A) a bulk transition peak at 0.798eV is observed, which indicates a slightly higher molar fraction of [In]=0.54, confirmed by the X-ray diffraction characterization around the main InP substrate peak[84]. The red dashed line in the figure is a gaussian curve used to fit the bulk transition and from which an FWHM of 4.2 meV at 15K is measured, in good agreement with the limit of 3.3 meV at 0K predicted for perfect LM-InGaAs [82]. Figure 2.5-B (sample B) shows a bulk peak at 0.802 eV where the gaussian fit indicates an FWHM of ~5meV. Samples are from two consecutive growth campaign, sample A shows the improvement in compositional fluctuation using the feedback provided by B and acting on the indium volumetric flow.

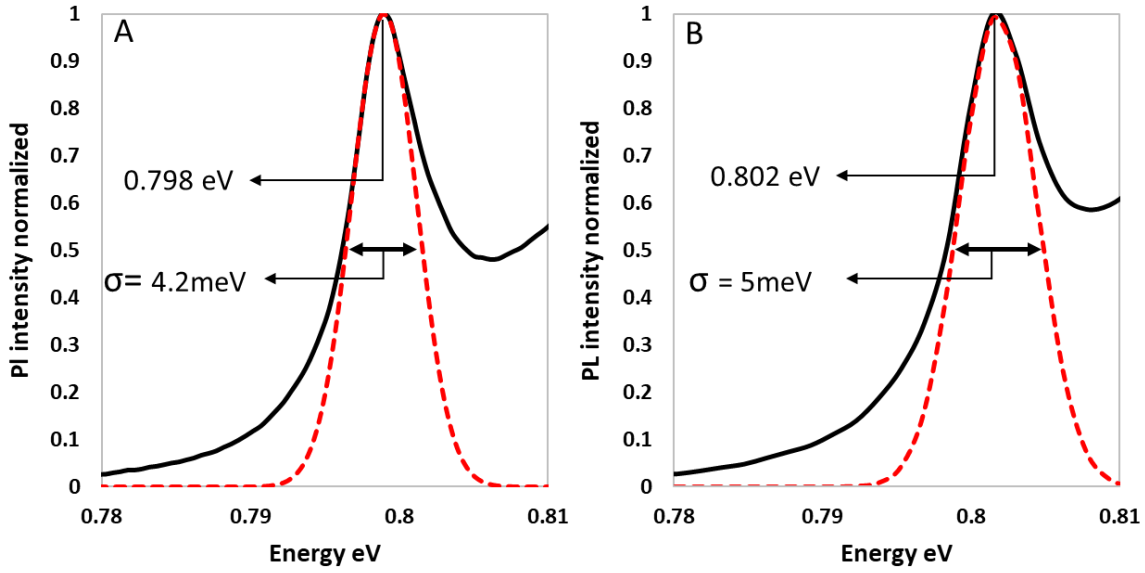

Figure 2.5 PL spectra from samples TS2483-1(A) ans Ts2473-1(B) highlighting differences in bulk LM-InGaAs PL peak position and FWHM.

The LTPL spectra also allows the non-destructive mapping of doping within the structure by measuring the Moss-Burstein[85] shift. Figure 2.6 shows the PL spectra in logarithmic scale from a structure that shares the same doping profile reported in figure 2.4A. Starting from the lower energy part of the spectra we observe the peak originated by the QW emission. A second peak associated with the band-gap of doped bulk InGaAs, and tailing is observed to higher energy. E_{max} and $\mathbf{E_{-20dB}}$ are highlighted by the red markers, their projection on the axis is indicated by the black dashed lines. For this structure the point at $\mathbf{E_{-20dB}}$ is 1.05eV to which correspond a doping concentration of $1.5 \cdot 10^{19}$ carriers/cm^{-3} derived from [64]. The range 0.85-1.0 eV has energies associated with higher order QW(n>1) and electron-light hole (lh) transitions. No clear features are observed in that range of energies, the broad PL spectrum observed in this range inis attributed to emission from the doped bulk material. More consideration about possible additional QW transitions will be reported in chapter 3. The high doping concentration layers and the low laser pump power required for this type of analysis make these transitions unlikely to occur[84].

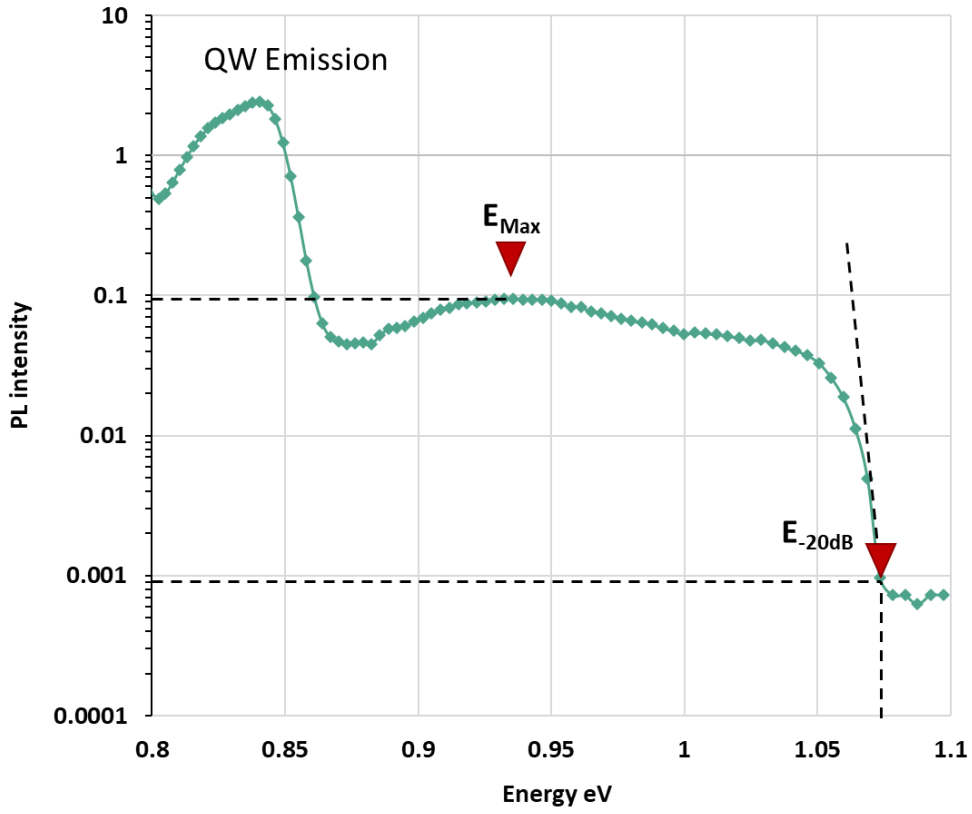

Figure 2.6 PL spectra (Logarithmic) and estimation of the doping concentration using the -20dB level Moss-Burstein shift [85].

2.3.3 Transition modelling and simulation

As explained in the previous section, Type-I and Type-II emissions are originated in the QW and their emission energies are dictated by the position of the quasi-bound states. Band profile simulations are used to calculate the energies of the quasi-bound states in the conduction band (e_1) and in the valence band (hh_1) varying the QW characteristics (QW thickness and mole fraction). This additional analysis was carried out to compare the experimental PL data against the theory. Simulations are developed in NextNano[86], first solving the strain equations and then correcting the band line-ups including the asymmetric doping profile (emitter and collector), the spacers, and the highly doped Indium-rich contact cap. On this basis, the Schrödinger–Poisson equations are solved self-consistently in the QW region. QW ternary compound effective masses are calculated considering the temperature and the strain conditions, with parameters from the work of Vurgaftman *et al.* [87].

Strain equations are fundamental to calculate the correct band profile for the structure as the mismatch in lattice constant affect the material bandgap and so, the band line-ups. The AlAs barriers are under tensile strain as the lattice constant is smaller than that of InP, this reduces the AlAs bandgap. Inside the well, on the contrary, the InGaAs is under compressive strain and the band-gap decreases. The strain moves and splits the degenerate valence band at the Γ points, in the AlAs barrier the tensile stress rises the light hole band above the heavy hole band in which the effective mass is higher, the opposite occurs in the well where the heavy holes band rises above the light hole band. Figure 2.7 shows the difference in the band structure when strain effects are incorporated.

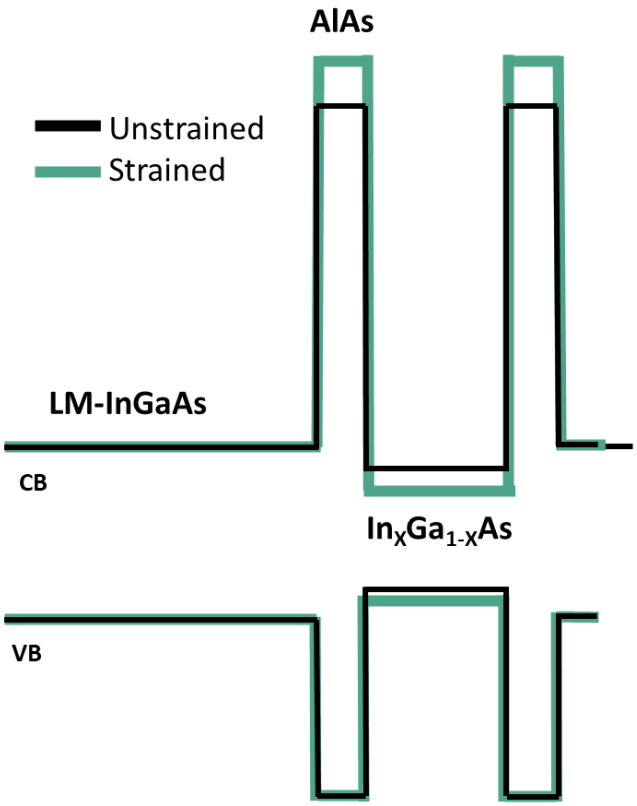

Figure 2.7 Schematic representation of the unstrained (Black lines) and strained (green) RTD band profile.

Figure 2.8(A-B) plots the Type-I and II transition energies obtained by simulation varying the InGaAs well indium molar fraction and the well thickness from 12MLs to 16ML in ML steps using a conduction band offset of Q=65%[88]. Red lines highlight ΔE between adjacent solutions, and it is observed that this is almost constant for a fluctuation of 1ML and reduces as QW thickness is increased. If the experimental PL spectra allows to discriminate the

position of each peak, the ΔE can be measured and used to determine in which range the real well thickness is positioned.

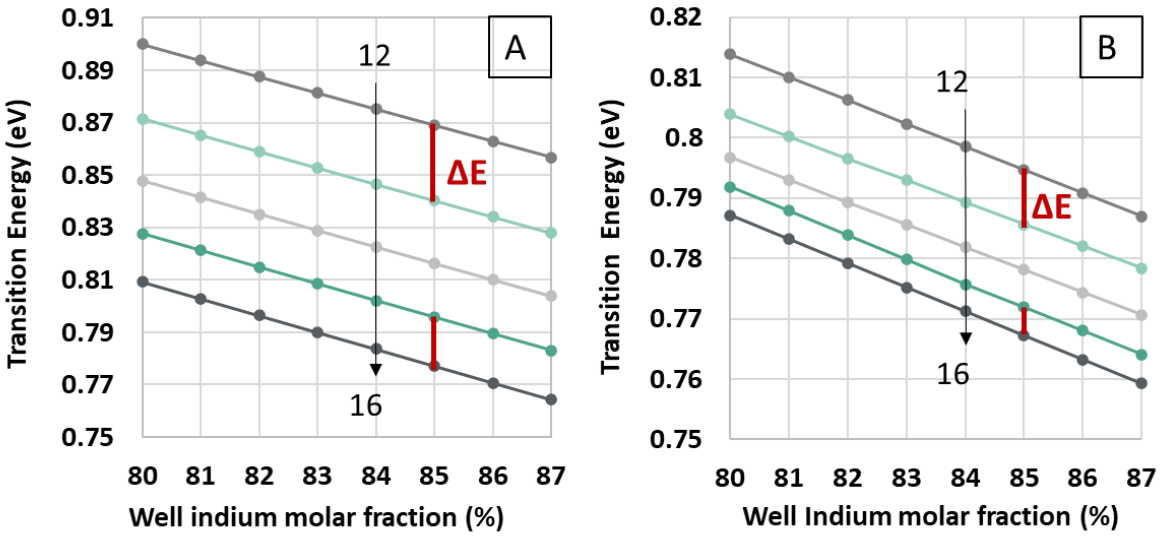

Figure 2.8 Simulated Type-I transition (A), and Type-II transition (B) varying the In mole fraction for QW thicknesses from 12 to 16 ML. Red lines are highlighting the ΔE between solutions for 1ML well width difference.

The conduction band offset (Q) plays an important role in determining the absolute value of e_1. It has an accepted value of Q=0.65[89], but this value depends upon several factors [90]. As a consequence, the bad-offset is often varied between ~0.5 and ~0.7 to ensure simulations fit experiment[90, 91]. Chapter 3 will discuss this parameter, and how it may be determined in more detail.

In terms of simulation processes laid out here, I explored the effect of the conduction band on the Type-I QW transition to highlight the need for an accurate method to determine this parameter. Figure 2.9 shows the Type-I energy varying the well thickness and conduction band offset from 75% to 55%. The graph highlights how a fluctuation of 10% in band offset may correspond to an error of 1ML in determining the QW thickness. This error is worsen considering the fluctuation in molar fraction.

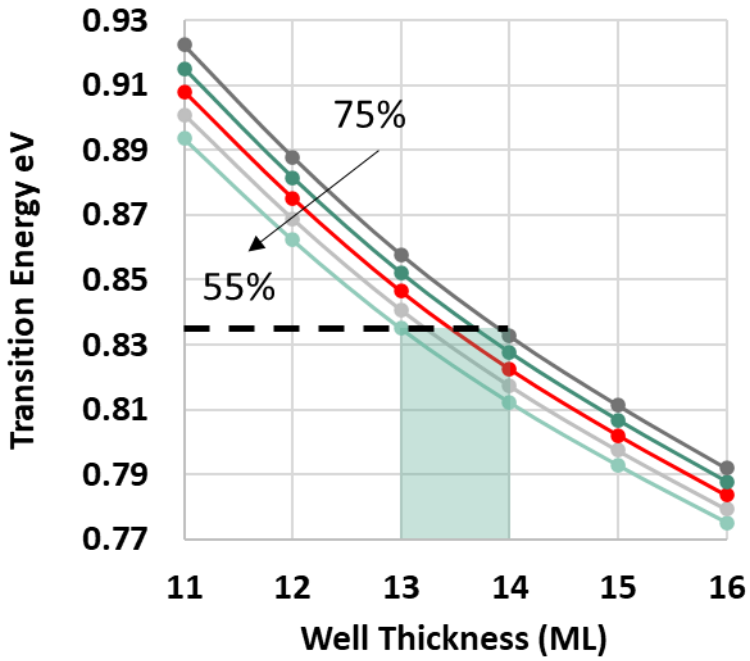

Figure 2.9 Calculated T1 emission energies for different conduction band offsets for QW thicknesses from 11 to 16ML.

2.4 PL spectra deconvolution

2.4.1 Mono layer fluctuation

RTD epitaxy can be performed using both molecular beam epitaxy (MBE)[37] and metalorganic vapour-phase epitaxy (MOVPE)[47] reactors, but despite the outstanding precision reached using these techniques, the growth process still suffer from small variations in the thickness of the layers and modulation of the heterointerfaces. Destructive and non-destructive characterization techniques demonstrated that the thickness error is not higher than 1ML (0.293 nm) which has important consequences when growing the QW, and in RTD characterisation and operation.

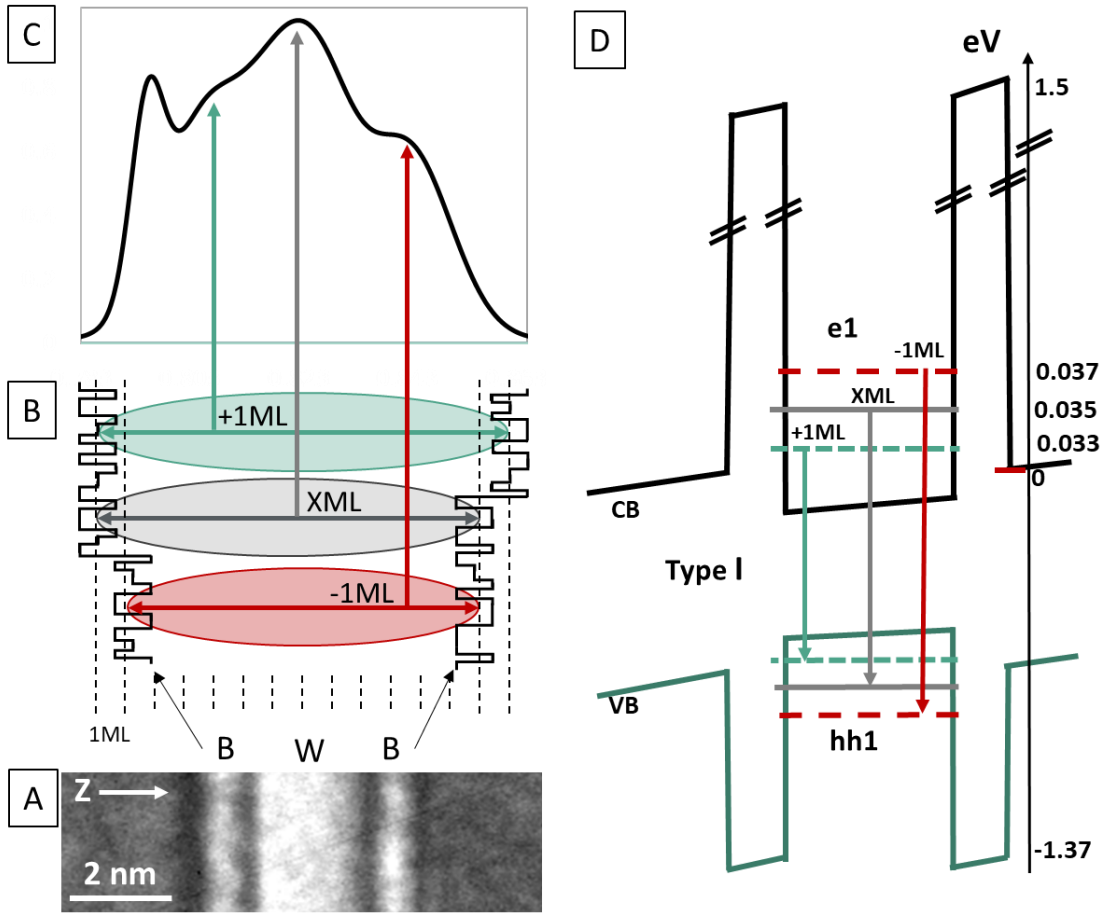

Figure 2.10 (A) Representative TEM scan of an RTD QW, labels indicate the Barriers "B", the well "W" and the growth direction "Z" from substrate to the contact cap (B) schematic representation of the heterointerface roughness and QW thickness ML fluctuation, coloured ovals schematically represent the exciton radius. (C) experimentally obtained PL spectra indicating long and short range disorder (see text), (D) not-to-scale representation of the equivalent QW band profile and additional E1/hh1 states (due to ML fluctuations) using the same colour-coding and labels from (B). Energy scale in figure D is reported to highlight the average 0.002 eV difference between the e1 states generated by the ML fluctuation.

The group of schematics and micrographs shown in figure 2.10 illustrate the mono-layer fluctuations present within our samples at the heterointerfaces and their impact on the PL characterization. Starting from the bottom, figure 2.10(A) shows a representative darkfield TEM image of the RTD active region, in which it is possible to observe the two barriers and the well region. Figure 2.10(B) shows a not-to-scale schematic of the RTD active-region, with the black lines highlighting the heterointerface roughness between the AlAs barrier and the InGaAs well. This roughness can originate from several sources: ternary imperfections (details will be presented in chapter 5), excessively high growth rate, growth temperature, lattice mismatch and strain relaxation (details will be presented in chapter 4). A high growth

rate affects the diffusion time of the constituent atoms on the substrate or on predeposited epitaxial layers. Atoms migrate/diffuse and nucleate to form the epitaxial layer, the time to complete the process depends on the temperature of the substrate and by the rate at which material is injected into the chamber. A fast process creates disorders with atoms causing roughness when the successive epilayer is deposited. This thesis will cover source of epitaxial imperfection generated by the materials involved, design choices, and strain relaxation. Growth processes are assumed to be executed by expert engineers, with the required experience to minimize human-factor errors. Similar consideration can be assumed for the imperfection related to the well layers. Vertical black dashed lines indicate the thickness in ML units while the horizontal arrows indicate the monolayer fluctuation in the well thickness, designated as XML in grey, the -1ML in dark red and the +1ML in green. Coloured ellipses indicate QW excitons (radius ~10nm [92]), which act as a probe, highlighting the length-scale of these structural imperfections [93]. Due to the low-temperature measurement condition, considerations on the exciton migration in the QW can be excluded [64].

Figure 2.10(C) finally shows typical low temperature PL spectra: we can observe 4 peaks, the first one from the left is the sharp bulk peak, while at higher energy we can distinguish another 3 peaks. The barrier roughness (length scale < exciton diameter) creates broad PL peaks while the ML-fluctuation (length scale > exciton diameter) cause peak splitting and an overall broadening of the PL trace [93]. The origin of the peak splitting is clarified numerically in figure 2.10(D): the ML-fluctuation creates 2 additional quasi-bound states (±1ML) in addition to the designed one (XML). The Type-I transition is now a triplet, and the same occurs for the Type-II transition[74]. The energy axis in 2.10(D) indicates the triplet position and highlights the average 0.002eV separation between the e_1 states. Data are obtained for a structure with 15MLs of well thickness and 80% indium mole fraction and 4MLs of barriers.

2.4.2 Peak deconvolution

The PL spectra are broadened by the QW grow imperfections (small-scale fluctuations) and peaks due to large-scale fluctuations are separated by a few 10’s of meV, as highlighted by the simulation reported in the previous section. Due to the desired QW characteristics, the peaks are distributed on the energy axis in a range that is already occupied by the LM-

InGaAs bulk and the highly doped InGaAs emissions. The overlap of spectral features makes it difficult to discriminate the exact peak emission energy, adding uncertainty in the characterization [74]. In some cases, peaks are completely “swamped” by other features and their position on the axis can only be estimated.

This section describes the PL spectra deconvolution as a method to overcome the overlapping of spectral features and obtain information on the spatial uniformity of the epitaxial wafer. PL data is compared with simulation, and a set of rules are applied to obtain a rigorous fit to the PL spectra that incorporates the short and long-range disorder of the QW.

Figure 2.11 shows sample TS1904 epitaxial structure and its PL spectra measured at 4K, obtained with 0.8 mW/cm^2 excitation at 900 nm (1.37 eV). The complete epitaxial structure includes an inactive copy-QW which does not contribute to the PL signal. More details about the copy QW will be presented in the next chapter. Four peaks are visible, starting from lower energy we observe a broad peak at 0.78 eV attributed at the Type-II transition, the central sharp peak (0.801 eV) attributed at the LM-InGaAs bulk peak, and two broad peaks (0.812 eV and 0.838 eV) associated with the Type-I transition. As described in the introduction, a triplet from both the Type-I and Type-II transition may be expected. For the Type-I transition we can observe two of the three peaks (X and -1ML), while the expected peak at lower energy (+1ML solution) is concealed between the Type-II transition and the bulk peak. Deconvolution of the spectrum is therefore required to determine the position of each radiative transition, through a step-by-step process comparing experimental data with simulations.

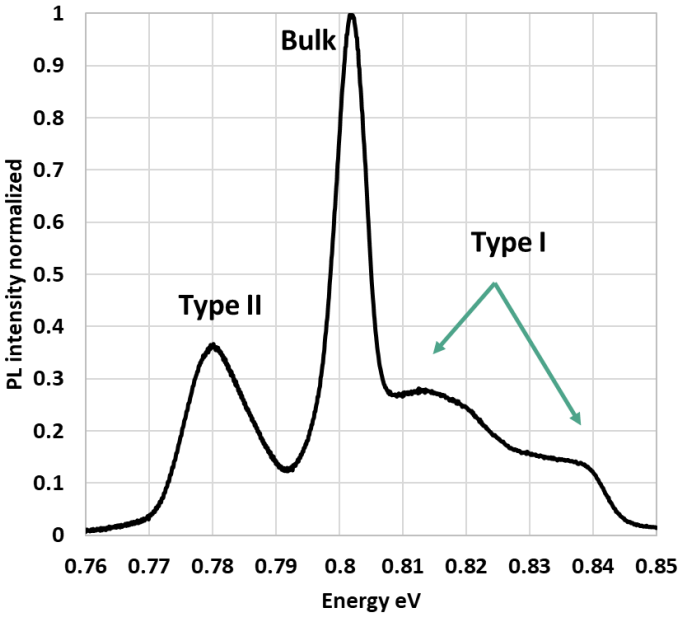

8nm	$In_{0.8}Ga_{0.2}As$	$2{\cdot}10^{19}$
15 nm	LM InGaAs	$3{\cdot}10^{19}$
25 nm		$3{\cdot}10^{18}$
20 nm		-
4ML	AlAs	-
15 ML	$In_{0.8}Ga_{0.2}As$	-
4ML	AlAs	-
2 nm	LM InGaAs	-
20nm		$3{\cdot}10^{18}$
400 nm		$2{\cdot}10^{19}$
InP		

Figure 2.11 Experimental PL spectra (left) measured from the structure reported in the table (right). Sample TS1904

2.4.3 Gap in knowledge

Several attempts were made in the past to deconvolute the PL spectra using a simulation-supported approach, but they were incomplete due to two main limitations, the solver used for the simulations and the treatment of the PL emission from highly doped layers. The infinite square model, used to simulate the quasi-bound states, cannot consider the spacers and the doped layers in the emitter and collector regions and the Type-II transition cannot be estimated. The finite square model and the transmission matrix method used in the past to simulate the RTD active region cannot into account the doping, furthermore, high J_{PEAK} designs are also characterized by thin barriers (≤4ML), a thickness that creates errors when the 1D Schrodinger equation is applied.

The simulations reported in section 2.3.3 has been shown to match the experimental data obtained from our structure with some discrepancies observed when the molar fraction is close to the 90% and the strain became excessively high. Section 2.3.1 has described how the doping concentration can be estimated by looking at the high energy tail in the PL spectra by the doped layers. This tail in the spectra occurs at lower energies to the LM-Bulk peak and it is located in the same range occupied by the QW transitions.

I reproduced the PL studies conducted previously on doped InGaAs[64] etching the RTD structure and measuring the PL response obtained by the doped layers. Figure 2.12B shows the reference structure and the etched craters from which I measured the PL signal reported in Figure 2.12A. After the bulk peak at ~0.8eV, the first curve (grey) shows a broad emission from 0.81 eV to 0.845eV. In the second curve (green) the emission reaches 0.86eV. It is easy to deduce that the shape and the broadening of these emissions affect the PL spectra when they overlap with the QW emission. The third curve (Black) is obtained by etching the structure through the doped layers where an undoped LM-InGaAs layer is deposited as a buffer before the InP substrate (not reported in the schematic). This last curve presents a weak emission after the bulk peak attributed due to some residual doped material from the previous layer left by an imperfect etch step. These results are in line with previous work and from these I deduced the need to include the doped layers emissions in the PL deconvolution.

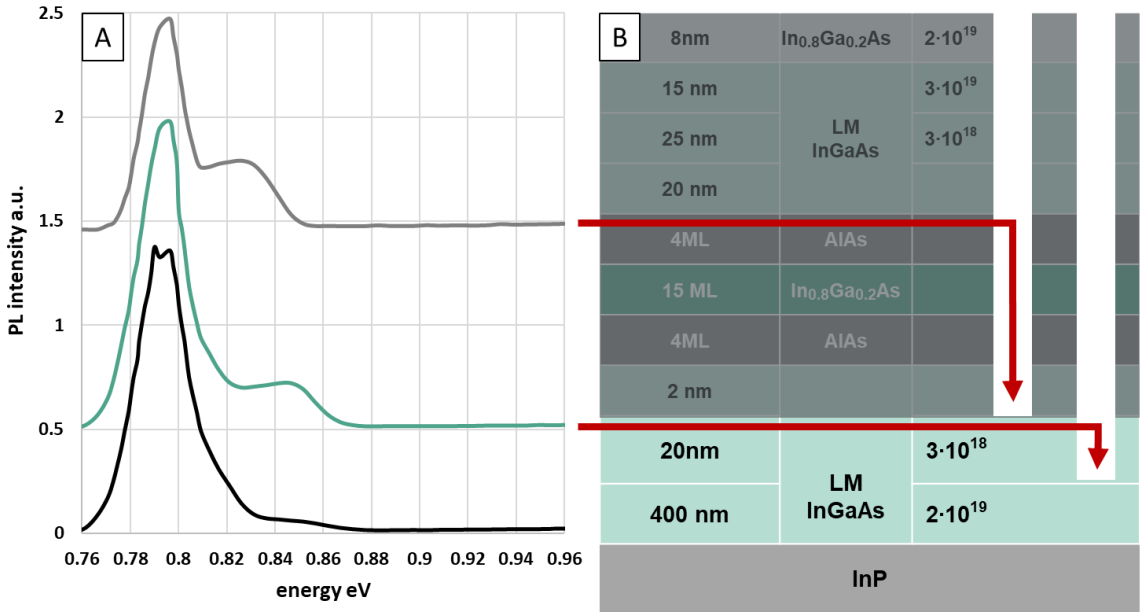

Figure 2.12 PL spectra(A) obtained by the doped InGaAs layers marked by the red arrows in the epitaxial design (B). Sample TS1904

2.4.4 PL line shape fitting

My line shape fitting is based on several constraints to regulate the position, shape, and amplitude of the peaks. The deconvolution of the Type-I emission is obtained using 3 Gaussian peaks (μ, σT1) (X ML, ±1 ML). Their position on the energy axis (μ) is based on the simulation described in Figure 2.8 (A and B). Three main rules are applied to fit the spectra:

- The energy splitting (ΔE) between transitions must be matched
- All the peaks must stay inside the experimental PL spectra
- Use the same T2/T1 intensity ratio for all the peaks to reflect the areal coverage of the fluctuations

The first two rules act as a positional constraint, the ΔE is a fit parameter as it helps in determining the emission triplet that characterizes the structure. The last rule is an energy constraint that dictates the intensity distribution between the peaks.

As mentioned earlier, assumption of the band offset creates some uncertainty. Additional simulations were carried out to test the effect of band-offset on the splitting ΔE, as it constitute a fit parameter. Figure 2.13(A) shows the simulated transition energies as a function of the well thickness for an arbitrary indium concentration (84%) with a standard conduction band offset (65%), according to the model-solid theory [89]. Well thickness is expressed in nm, with mono-layer equivalent solutions marked by the markers, while red arrows highlight the ΔE for adjacent well thicknesses. Figure 2.12(B) shows the same simulation increasing the band offset to (75%). The observed change in ΔE with respect to figure 2.4(A) is 0.3 meV. On this basis the band offset does not affect ΔE and does not contribute in confounding the fitting at this stage.

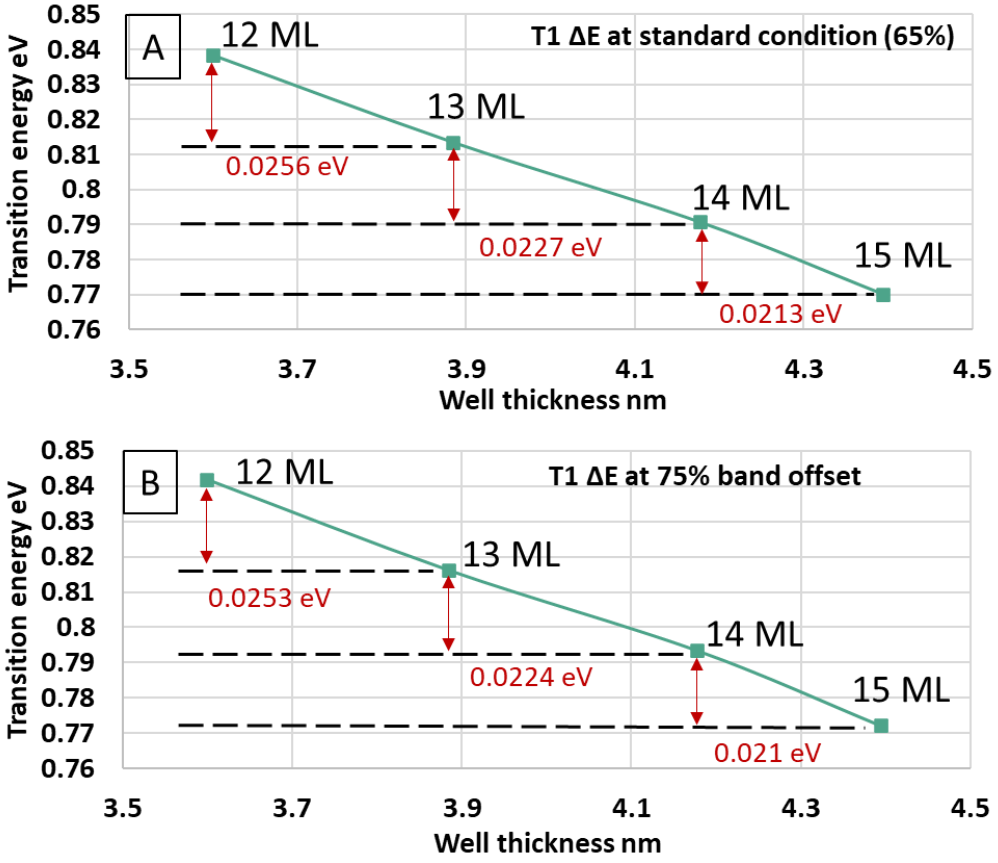

Figure 2.13 Energies of T1 transition for a typical RTD structure (sample TS1904, see text) using a standard conduction band offset of Q=65% (A) and for a higher Q=75

Based upon the essentially equal splitting of the transitions we assume an equal linewidth (σT1) for the three Type-I transitions[6]. For the Type-II transitions, we use the same rules, with 3 Gaussian peaks (μ, σT2) for the transitions (X ML, ±1 ML). Here, the energetic position is again dictated by simulation but with the linewidths (σT2) governed only by the variation in the hole transition energies[13]. In the deconvolution process, the ratio of the integrated intensity of the X, +1 ML, -1 ML transitions for the Type-I and Type-II transitions are kept constant.

Figures 2.14 illustrates schematically the fitting steps. My procedure begins by accommodating the bulk peak and the doped bulk InGaAs tail (blue curve in figure 2.14(A)), using PL characterization of doping layers extensively studied by K.J Jacobs [14]. Based on the simulation reported in figure 2.8, I then accommodate the expected 3 Type-I peaks (15ML and the ±1 ML) as shown in figure 2.14(A). The peak amplitude is arbitrary at the stage, to simply visualize their position I settled on the same intensity values for all. I note here that in this case, the +1ML peak at 0.775eV is partially outside of the spectra, the XML

peak at 0.791eV may be fitted by tuning the amplitude while the -1ML peak seems not in line with what we observe with the peak at 0.815eV (black dashed line). I found that no good fit can be obtained for the triplet 14-15-16 MLs. Figure 2.14(B) shows a possible fit using the triplet 13-14-15 MLs. Here I again obtain peaks at ~0.79 and 0.81 eV (+1ML and XML peak this time) , along with a new peak at 0.834 eV that now lies inside the envelope of the experimentally obtained curve, providing a candidate for fitting the spectrum. I am now able to accommodate the 3 Type-II peaks, albeit with the +1ML feature being partially outside the envelope of the spectrum. I note that a fit may be possible by reducing its amplitude, but the major concern is the mismatch of the XML peak, which suggests that by tuning the molar fraction I may increase the transition energy and improve the fitting. Figure 2.14(C) shows the triplets changing the molar fraction from 85% to 84%, all the peaks are inside the experimental spectra and the XML also match at 0.815eV. Once the position of the peaks has been established, their amplitudes need to be tuned, and as I previously indicated, the ratio of Type-I to Type-II emission (T1/T2) is a fit parameter. This parameter occurs as the laser may excite differently the Type-I and II transition for a given ML solution, but all the triplets from spatially separate regions of the sample are equally excited.

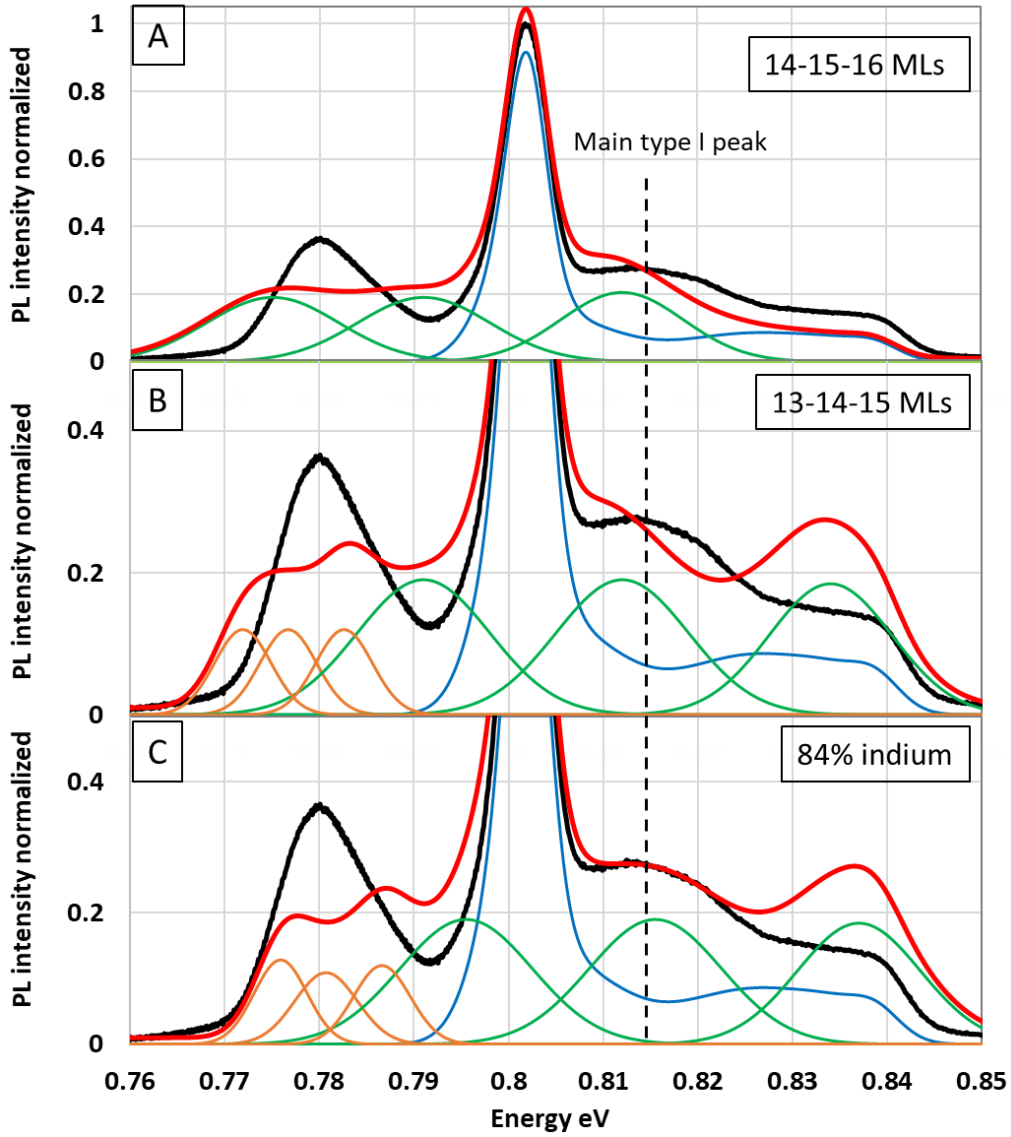

Figure 2.14 Schematic showing attempts to fit PL spectra using the process described in the text for the sample TS1904. (A) using the triplet 14-15-16 MLs as well thickness and 85% Indium mole fraction,(B) using the triplet 13-14-15MLs, [In]=85%, (C) triplet 13-14-15 and [In]=84%.

Having described the fitting process, I now move to fit the PL spectra of two different samples, combining simulation and weighting of the different peaks due to long-range disorder. Figure 2.15(A) shows the fit obtained tuning the T1/T2 ratio with minor correction on the positions of the peaks given by the variation of the band offset. The bulk peak has a linewidth of 4meV [94]. For the fitting, I used σT1=7 meV and σT2=3meV and a T2/T1 =1.57± 0.01 utilising a band-offsets of 60%. The T1/T2 ratio is the additional task to validate the positions of the peak once the PL line shape is fitted. An arbitrary assignment of the amplitudes of each peak may lead to an ambiguous combination of QW thickness, indium concentration, and band offset. The XML Type-II transition is at 0.781 eV, 1meV higher

with respect to the observed position without the line shape fitting. Similar considerations are made for the X ML Type-I transition peak, with the e1 position being 0.0345eV lower with respect to our first estimation (0.045-0.05eV) based upon standard band offsets. Figure 2.15(B) shows the fitting obtained from a second sample with a QW thickness of 13ML and 87% [In]2.3.3, in this case, the T1/T2 is 3.84± 0.01. For this sample, ΔE is wider, and peaks are more spread on the energy axis. For the fitting, we used σT1=6.5 meV and σT2=3meV, with the same band offset.

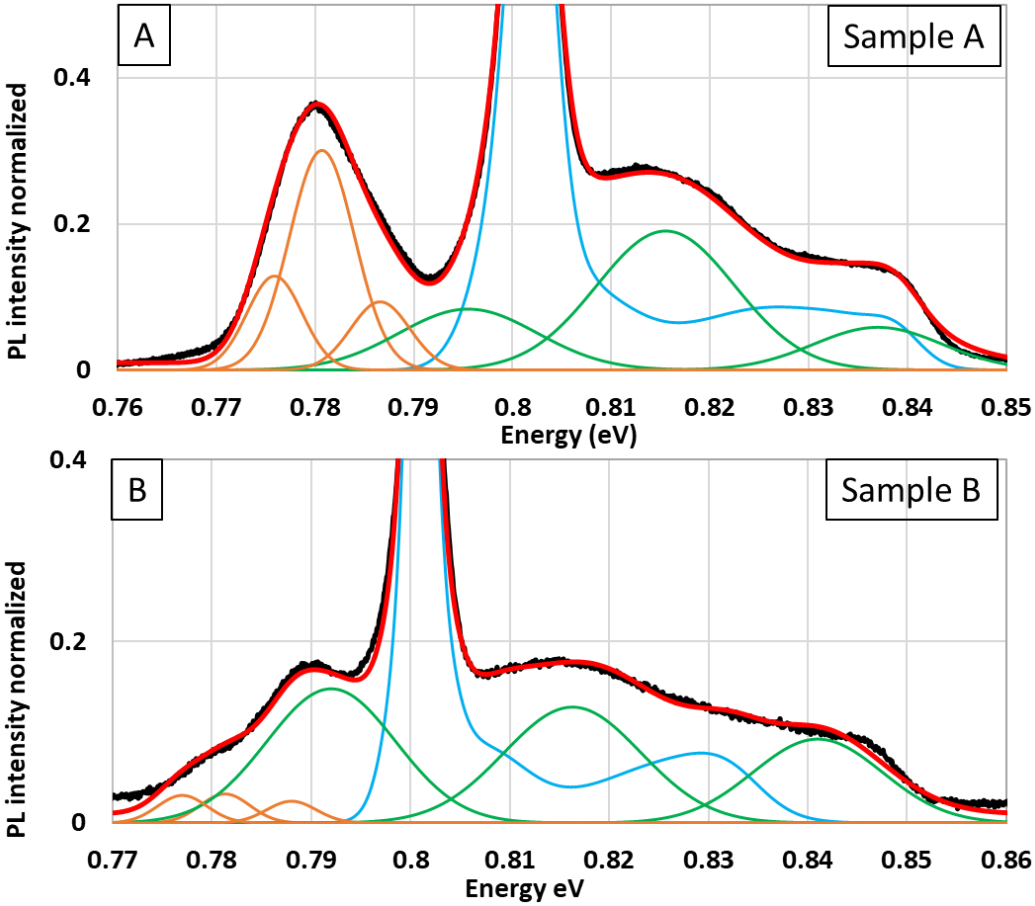

Figure 2.15 PL spectra deconvolution of the reference structure (A) sample TS1904, fitting obtained for a second structure with a QW thickness of 12ML (B) sample TS2474-1

The results show excellent agreement between simulation and PL spectra, despite some residual uncertainty. This line shape fitting process allows a constrained and hence more accurate characterization process. Additional information about the volume of material subject to long range QW fluctuation is provided by looking at the distribution of the peak intensities. Further analysis of the reported fittings highlights the follow intensity distribution between the QW transition: 57% XML, 25% +1ML and 17% -1ML. The second

sample shows more homogeneous distribution: 35% XML, 40% +1ML and 25% -1ML. This information may be used to inform growth optimisation.

2.5 Conclusions

In this chapter, the optical spectroscopy characterization of High J_{Peak} design RTD wafers growth by MOVPE was described. A review of previous work utilising PL spectroscopy in characterizing the doping concentration, the bulk crystal perfection and the QW characteristics was made, and certain elements were reproduced. My improvements in the choice of simulation method has improved the characterization of the Type-I transition while the inclusion of the doping in the band profile has improved the estimation of the Type-II transition energies.

In the final section, I described a method to fit the PL line-shape for high J_{PEAK} RTD structures and showed how this deconvolution increases the accuracy of structural characterization. The method compares simulation and experimental data to provide a set of "fitting constraints" for an unambiguous fitting of the PL spectra. Two different samples were analysed to highlight the versatility of the method in the case of wide peak splitting and low Type-II PL intensity. The fitting helps to determine the exact position of each peak increasing the accuracy in determining the e1 position obtained by the difference T1-T2.

2.6 Future work

2.6.1 Road to a full automated characterization tool

The proposed line shape fitting can represent a useful tool to set a route to future growth optimization of RTD structure. PL mapping already demonstrated its validity to the assessment of the doping concentration scanning multiple point on the wafer. Based on the same system, the inclusion of the PL line shape fitting can reveal how the wafer properties vary and quantify the statical variations of the electrical and physical properties.

Future automatization of the fitting process is required to unlock the full potential of this techniques and its inclusion in a mapping procedure. The developed algorithm for the fitting can be implemented in MATLAB.

MATLAB is one of the available computing environments that allows the user to develop

stand-alone program easy to be integrated in third-part software like LabView and directly control the hardware.

2.6.2 Room temperature PL characterization

From a manufacturing perspective, the most attractive improvement is represented by the ability to perform PL measurement at room temperature. PL apparatus are commercially available, but the main inconvenience is represented again by the cryostat. PL is labelled as a fast characterization tool but in some cases this quality is mined by the cryostat. Sample mounting requires cryo-rated vacuum grease and the cryostat needs time for the pump down and cooling time.

The fitting algorithm may be improved modelling how the PL line shape changes increasing the temperature form 15K to 300K. The bulk peak energy is associated with the InGaAs band-gap and its temperature dependent evolution is well known. About the QW optical emission, their position on the energy axis it not dependent by the temperature, but their peak intensity is extremely dependent by the temperature of the sample.

2.6.3 Micro-PL characterization

The information obtained by PL are averaged based on the volume scanned by the laser spot. The PL fitting highlighted a non-uniform intensity distribution between peaks. More experimental studies are required to reduce the PL spot to a micro scale and scan a small volume of material. Long- and short-range disorder may observe to vary differently around the wafer if the PL is reduced to few μm^2 as already highlighted by TEM scans. once again, the goal is to push further the use of non-destructive techniques an maximize PL capabilities.

2.6.4 PL excitation and overlapping free detection ranges

Photoluminescence excitation spectroscopy (PLE) is a complementary technique for PL used to identify the origin of multiple peaks features but where the peak overlapping cause confusion in the data. PL fitting can overcome this issue indicating the overlapping-free detection ranges where apply PLE. At the same time PLE can help identifying the conduction band offset to remove residual uncertainty from the PL fitting.

2.6.5 Wafer to device characterization

The characterization process indicates the real wafer characteristic and provide feedback to the epitaxy. To take full advance from the characterization, a link between the PL spectra and the future device performance needs to be set to enhance manufacturing process. The E1 states can be detected by the difference T1-T2 (see section 2.3), but the T2 transition is not always clearly observable as it may be “swamped” in the spectra. Pl fitting provides critical information, but further developments are required to univocally link PL features and device performance.

2.6.6 Comparison of growth technique

RTD are grown by MOVPE and MBE and different growth techniques/methodology were developed to improve the epitaxial quality. PL line shape fitting can highlight difference in heterointerface quality looking at the peak splitting (number of peaks) and the FWHM of each peak.

Chapter III: Photoluminescence excitation spectroscopy

The development of a complete wafer characterization scheme is an essential part of the development of a new emerging technology such as RTDs for THz applications. The scheme will inevitably involve more techniques as a fast and non-destructive scheme is the only possible one compatible with the requirements imposed by the industries and the market. More important is the double necessity to accurately characterize all the active region parameters and to do that by mapping multiple points of the wafer. The technology progression towards smaller and smaller devices increases the need of accurate growth process and characterization tool.

This chapter further explores the use of luminescence techniques for the characterization of RTD epitaxial structure. The challenge in characterization presented by these nanostructures requires the development of a characterization scheme utilising a combination of techniques. Non-destructive schemes reported in literature are based on combination of XRD and photoluminescence techniques [74, 95-97] . In my work I have added a rigorous PL line shape fitting and in this chapter, I describe photoluminescence excitation (PLE) spectroscopy to complement the non-destructive characterization. LT-PL and the spectra line shape fitting were introduced in chapter 2 and used to characterize the RTD wafer electrical and physical properties with a margin of uncertainty due to their being multiple solutions to a given emission energy, and uncertainty in the band-offsets. Based on this previous work, this chapter describes the step-by-step characterization procedure and how to photoluminescence excitation (PLE) spectroscopy may be included in the characterization scheme. The PLE study of RTD epitaxial layers was reported by me in [49].

This chapter is made up of 5 sections.
The first section introduces the proposed step-by-step characterization scheme, and how the different techniques are used in synergy to extract additional, high precision, meaningful information. The description starts with the characterization of the physical parameters of the RTD QW using HR-XRD alone.

The second section recalls the PL line shape fitting shown in the chapter 2, used to improve the characterization accuracy. This work is extended to allow the selection of emission overlap-free PLE detection ranges. This section also analyses in more detail the issues related to the conduction band offset uncertainty.
Section 3 details the PLE techniques as a tool to allow more accurate structural and electronic characterisation by the simultaneous determination of the band-offset.
Section 4 concludes the chapter while section 5 describes future areas of work.

3.1 Characterization scheme

The RTD epitaxial characterization is based on 3 main variables, the barrier thickness B_{th}, the well thickness W_{th}, the QW indium mole fraction [In %]. Based on these parameters, the position of the e_1 state can be included as a fourth variable and determined by the difference T1-T2, or by comparison with simulation (as T2 is not always observable). This variable has a critical importance for the device operation, but does not provide significant input into the structural characterization of the structure. Each characterization tool has its own level of accuracy, and combining multiple techniques with simulation, the characterization uncertainty can be reduced, as shown previously [74, 98]. However, in these works, the uncertainty in the band-offset is not addressed [99].

In my work, I introduce a determination of the band-offset as a fifth variable to further improve the characterization. PLE is the non-destructive technique of choice to obtain information about this parameter. By obtaining information about multiple electron states within the structure, an unambiguous solution to band-offset, well width, and well composition can be obtained [49, 74, 80].

A schematic diagram of the characterization process is shown in figure 3.1. Nominal growth parameters are used as a starting point for simulations and XRD data fitting. A first raw solution is obtained after the PL fitting and the simulation, with a certain margin of errors. PLE is then introduced after the PL fitting to provide additional information and remove any assumptions around the band offset. The relation between PL and PLE will be explained later in this chapter. Final structure parameters are obtained after the iterative comparison between PL fitting, XRD fitting and simulation.

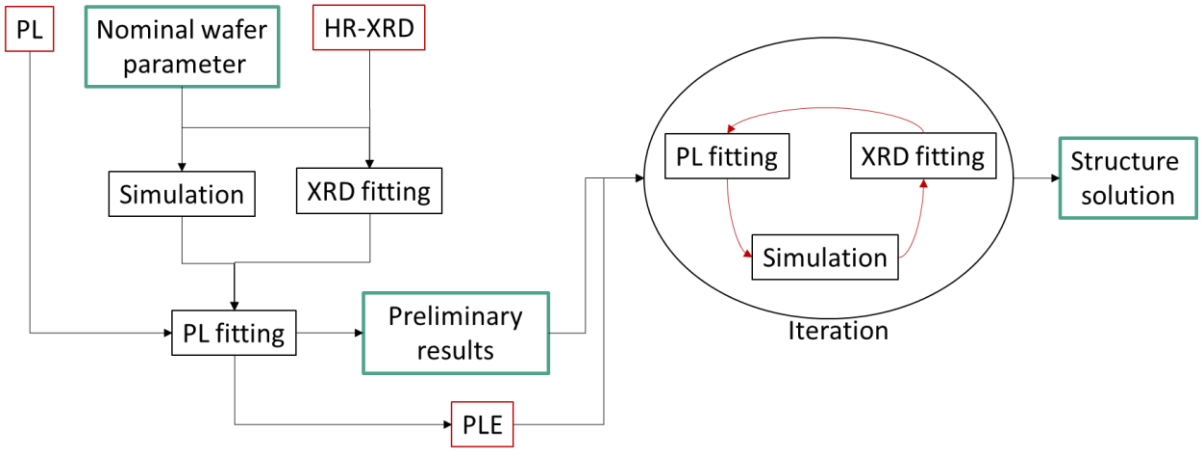

Figure 3.1 Schematic of characterization process flow to synergistically determine epitaxial physical structure and electronic band-structure.

3.1.1 XRD characterization

Figure 3.2 shows the complete epitaxial layer design of the test structure under investigation. From the top, the structure consists of the doped contact cap and the first QW, after the spacer and the collector, the structure has an undoped "copy" active region. The introduction of this additional QW has been shown to assist the structural characterization improving the S/N ratio in the XRD pattern [74]. This epitaxial structure was also employed for the samples in chapter2. The copy QW does not contribute to the PL analysis, and for simplicity, the complete epitaxial structure was omitted in the previous chapter. Section 3.3.1 will describe the laser penetration depth through the structure and the role of doping in suppressing hole diffusion near the copy QW.

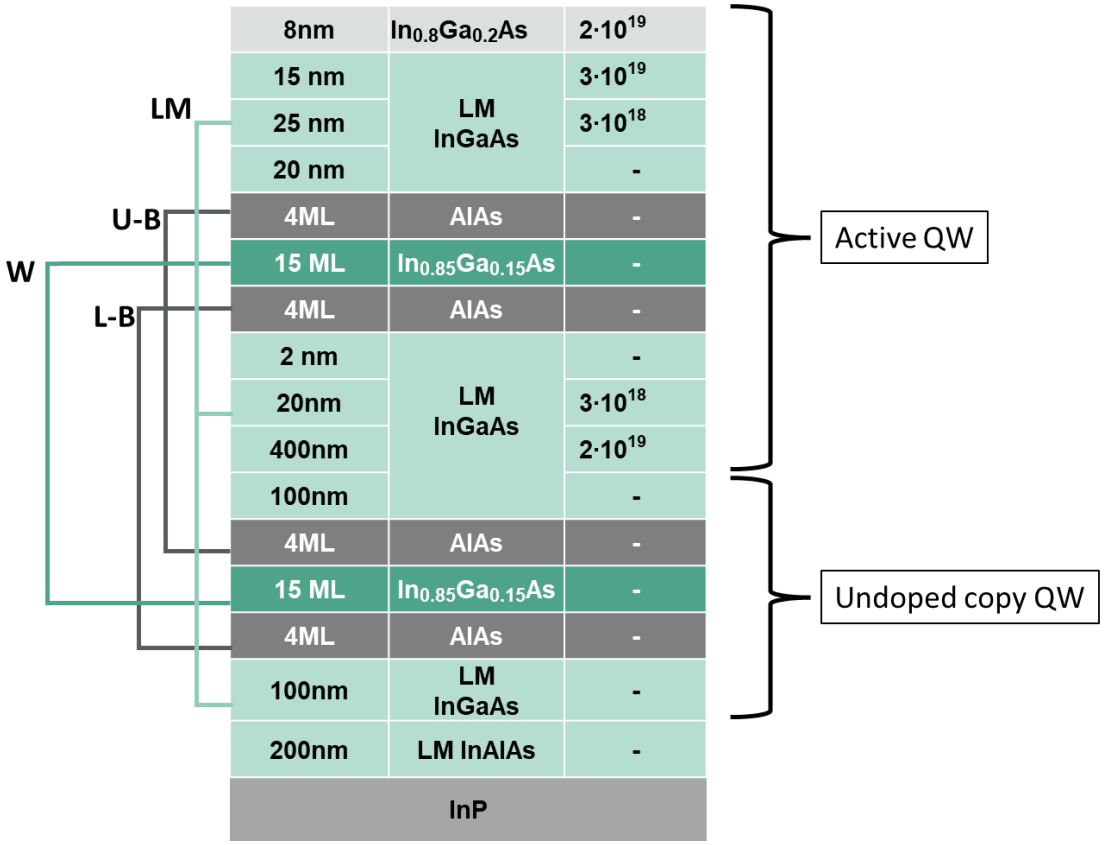

Figure 3.2 Epitaxial structure under test (sample TS1904), including the copy undoped QW on the bottom of the structure excluded in chapter 2. Coloured lines on the right side indicate the layers linked for the XRD fitting (see text).

The characterization starts with a long XRD scan in the range 29.5-34° and the data fitting to extrapolate the structure physical parameter. The data fitting is obtained by a curve fitting algorithm in Jordan Valley RADS. Here common layers are "linked" in the software as they are assumed to be affected by the same error/fluctuation[74] during the growth process. That is to say that their growth rate (proportional to thickness) and compositions are equal. These layers are the LM-InGaAs (LM), the upper barrier (U-B), the InGaAs well (W), and the lower barrier (L-B). Linked layers are highlighted in figure 3.2 while results are reported in figure 3.3.

Experimental data are reported in green while the data fitting is reported in grey, shifted to a lower position to help the reader.

From the fitting, we deduce a range of physical parameters, finding the LM-InGaAs in an excellent overlapping with the InP substrate peak, represented by the main sharp peak at 31.517° (0.153° of offset respect the 31.670° introduced by the measurement apparatus). The second peak at 31.46° indicates a slight lattice mismatch in the InAlAs layers.

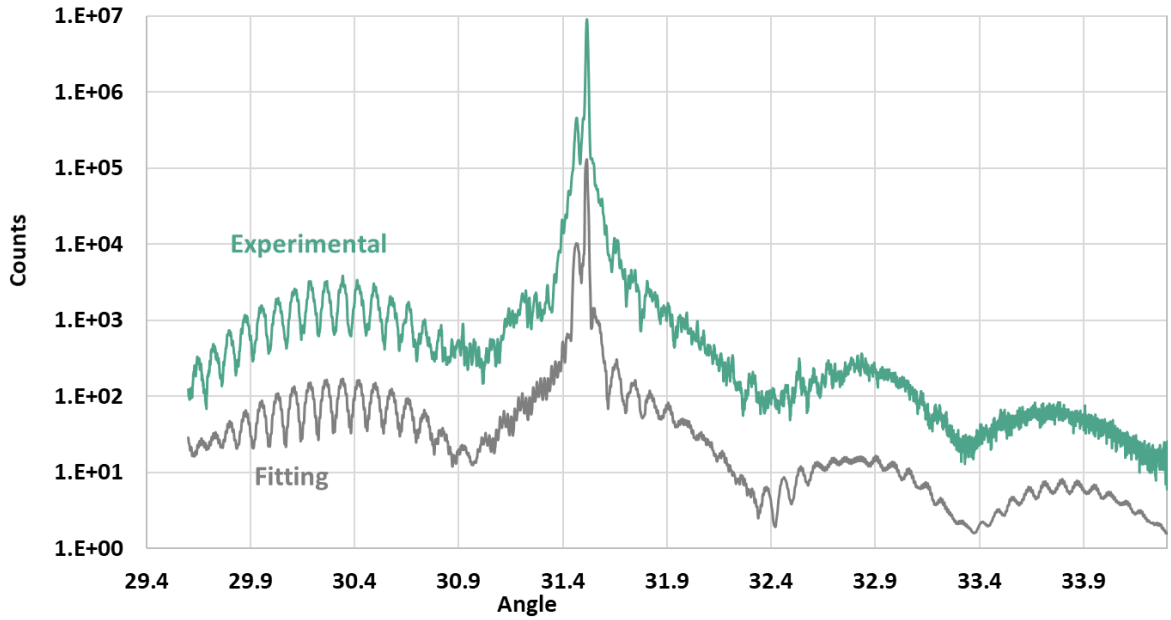

Figure 3.3 HR-XRD scan in the range 29.5-34° for sample TS1904.
Experimental curve in green, fitting data in grey. Curve are shifted to help the reader.

Due to the QW strain condition, the wells and barriers affect the XRD curve differently. The well is under compressive stress and its properties can be detected observing the left-hand side of the XRD scan in respect to the central substrate peak. An XRD sensitivity analysis based on the fluctuation in the well properties was previously conducted [84]. Thickness fluctuation lower than ±2ML and molar fraction lower than ±7% cannot been distinguished by experimental XRD data and fitting. A further reduction in uncertainty in the physical parameters of the quantum well is obtained combining XRD and PL and will be discussed in the next section. Here I focus the attention on the barrier characterization, for which the PL provides very limited information. In the fitting I introduced a ±1ML fluctuation error in barriers thickness, and the results of a sensitivity analysis are reported in figure 3.3. As the AlAs barriers are under a tensile strain, the effect on the XRD scan is mainly observed on the right side of the substrate peak. Figure 3.4 shows the XRD experimental curve (green) compared with the simulation, +1ML in grey and -1ML in red. The +1ML solution presents a strong mismatch with respect to the experimental data. For example, the pronounced valley around 31.9° and 32.4°, and the improvement in the signal intensity at 33.9°. The +1ML scenario is the best case to analyse because more semiconductor material contributes to the diffraction process, improving the signal intensity. The -1ML curve presents several similarities with respect the experimental data, but the fit

is poor for these parameters. Based on the results the variation in barriers thickness is therefore considered to be no more than ±0.5ML.

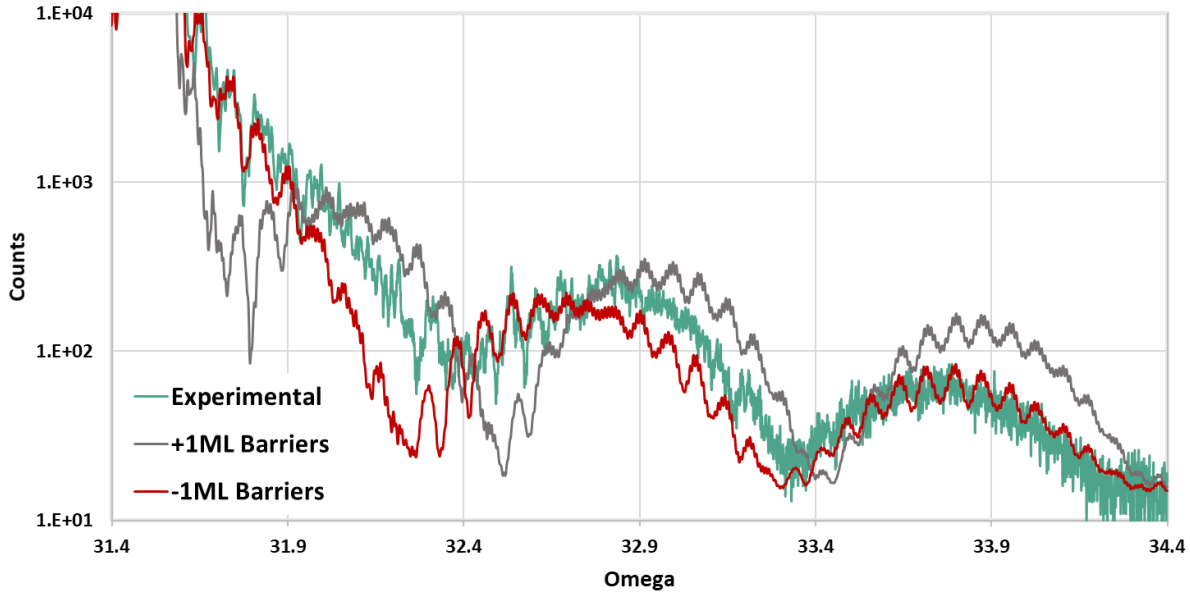

Figure 3.4 barrier fluctuation sensitivity analysis for sampleTS1904. Experimental data in green,+1ML in barrier thickness in grey and -1ML in red.

The employment of a high resolution XRD apparatus is fundamental to conduct this type of analysis where the important features are close to the noise floor. The introduction of a copy QW for characterization purpose improves the S/N [74]. One may consider the introduction of a MQW layer below the RTD structure to further assist the structural characterization. However, the QW and barriers are under high strain conditions, and an MQW risks strain relaxation and the introduction of deleterious effect on the RTD operation

3.2 LT-PL

The XRD alone cannot completely characterize the RTD active region due to the uncertainty in well thickness and more importantly, due to the low sensitivity that the XRD shows for changes in the well molar fraction. As a change in the [In] modifies the position of the quasi-bound states and consequently the electronic levels and optical transition, LT-PL further reduce the mentioned uncertainty. Figure 3.5 shows the LT-PL spectra and the line shape fitting of the structure, obtained following the fitting procedure reported in the previous chapter. The experimental curve is plotted in black, while the fitting is represented by the

red dashed line. Black arrows indicate the Type-I ML solutions, the ΔE between the solutions is also reported.

The table reports the extrapolated QW parameters and compares the accuracy obtained by combining the two characterization techniques.

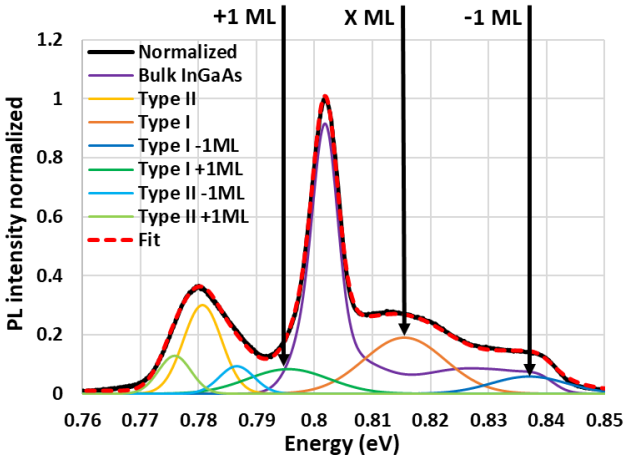

Variable	Design	XRD	XRD+PL
AlAs B_{th}	4	4 ± 1ML	4 ±0.5ML
InGaAs W_{th}	15	15 ±2ML	14 ±1ML
QW [In]	85	86 ±4%	84 ±2%
E1 [meV]	/	/	35 ± 15meV
B.offset	/	/	60% ±8%

Figure 3.5 PL line shape fitting for sample TS1904. The table shows the QW parameter and the error in characterization.

The Type-I optical transition is sensitive to a variation of both the W_{th} and the [In], section 2.3.3 already highlighted how the Type-I emission energy can be associated to several combinations of W_{th} and [In]. Using the results obtained by the experimental XRD scan as a new starting point, the PL line shape fitting is now repeated with new constraints, leading to a reduction in uncertainty for the W_{th} and [In] up to 1ML and 2% respectively. The table in figure 3.5 also reports the estimated e_1 position and the conduction band offset ratio, obtained comparing the experimental data with simulation.

3.2.1 The conduction band offset

The conduction band-offset (Q), the percentage of the band-gap difference accommodated in the conduction band, arises from the band discontinuity at the heterointerface, and it controls the electronic states and so the fundamentals of the device operation. For some semiconductor alloy pairs, band offset values have been extensively studied, e.g. for the case of AlGaAs/GaAs [100, 101]. Less information has been reported for the InGaAs/AlAs material system and there is some scatter in reported values. For InGaAs/GaAs A Q= 35%-

85% were reported in [102] for a mole fraction of [In]=<0.35. For InGaAs/GaAs with [In]=0.5 the conduction band offset varies in the range Q=57%-90% [87]. For AlAs/InGaAs a range of Q=63-56% for [In]=0-0.35 was measured using a series of RTD IV characteristics [103]. This method includes device fabrication, with all the associated variations due to this process, and the reported results are affected by an uncertainty of ~10% when [In] approaches 35%. Band-offset values have been mostly deduced from optical techniques, but optical transitions have shown low sensitivity to this parameter[104]. In my measurements, this is confirmed by the ±10% error obtained after the PL fitting. This value leads to a possible fluctuation of few meV in the Type-I peak position which cannot be deconvoluted from possible fluctuations in molar fraction or fractional ML fluctuations in the well thickness.

PLE finds its space in the characterization process as a method to detect additional higher order optical transitions (e.g., e2-hh2 transitions). This provides an additional data point that must also be solved by the same structural parameters and band-offsets as for the fundamental transitions observed in PL. The comparison of this additional data with simulation [90, 105] provides additional accuracy. A correct band-offset for highly strained InGaAs (In>0.7) is essential to future engineering of high J_{PEAK} RTD structure and to realise new designs.

3.3 Photoluminescence excitation spectroscopy

PLE is a complementary technique to PL. In PL the sample is excited using a fixed excitation wavelength and the intensity of the wavelength resolved signal is made to form a spectrum. In PLE, the detection wavelength is fixed, and the excitation wavelength is varied. As a consequence, the absorption spectrum is probed. Using this technique it is possible to determine the energies of higher order optical transitions.

3.3.1 Laser penetration depth

In the work presented here, the PLE analysis is carried out varying the excitation wavelength in the range 700-920nm in steps of 5nm. In this range the laser penetration depth is expected to vary considerably. Using the top of the structure as a reference, the RTD active region is positioned approximately 65nm deep, below doped and undoped InGaAs, while the copy

QW is around 600nm deep. A laser penetration depth analysis was carried out before the measurement to verify that the laser penetration depth. At the same time I verified that for the highest penetration depth the laser does not excite the copy undoped QW. The analysis was conducted taking into account the doping concentration, the different semiconductors involved and the angle of incidence. The laser penetration depth is defined as the depth at which 1/e (37%) of the total incident light is transmitted [106]. This value is derived by the Beer-Lambert law of absorption [106]:

$$P_T = \alpha P_I (1 - R) e^{-\alpha x} \qquad \text{(eq. 3.1)}$$

Where P_T is the transmitted power, P_I is the incident power, and R is the reflection coefficient. α is the absorption coefficient that depends on the extinction coefficient k and the radiation wavelength λ.

A doping-dependent refractive index study is reported in [24] on several layers of lattice match InGaAs with doping concentration from $1e^{15}$ to $3e^{19}$. For doping concentrations like the ones of the sample discussed here, the refractive index changes only for radiation with an energy close to the energy gap (0.796-0.802 eV). The PLE laser radiation lies in the range 1.34-1.78 eV, on this basis I excluded the doping from the analysis.

The PLE set-up was designed to excite the sample with an incident-angle of β=30°. The snell and Fresnel equation were computed to calculate the transmission/reflection coefficient at each heterointerface and the overall QW. I started the analysis from the worst-case scenario, represented by the InGaAs/AlAs at λ =700nm, which has the highest refractive index. In the reported condition the calculated reflection coefficient is $R_{InGaAs/AlAs}$= 0.0016, meaning that the vast majority of the light is transmitted. With regard to the AlAs barrier, the AlAs extinction coefficient is α ~0 in my PLE range, on this basis the laser absorption through the barriers can be overlooked. In conclusion, for the worst-case scenario the overall QW produces a transmission coefficient T_{QW}~1 and I deduced that the penetration depth is not affected by the QW.

Based on the above consideration, I computed in MATLAB the equations to calculate the energy absorption rate and the penetration depth increasing the excitation wavelength. Figure 3.6 shows the energy absorption rate for each wavelength, the total transmitted power

is represented by the area under each curve, normalized at 1 in the graph. Using the 700nm wavelength as reference, the laser penetration depth is indicated by the red dot at 80nm, more than 10nm after the QW indicated by the grey and green rectangle. The inset in figure 3.6 shows the laser penetration depth varying the excitation wavelength (primary horizontal axis) or decreasing the excitation energy (secondary horizontal axis, top). Using the energy reference, the graph highlights that the penetration depth is higher with decreasing the excitation energy, meaning that bulk InGaAs after the active region participates in the luminescence process. The max depth is 290nm, approximately 300nm before the copy QW, this therefore excludes emissions from the bottom part of the sample. Additionally, due to the high levels of doping, electron-hole recombination in the thick bulk material blocks the diffusion of holes near the copy QW. As reported in figure 3.2, there is 400nm of doped InGaAs (after the first QW) in which absorption and recombination occurs before the copy QW. The PLE peaks analysis in the next section will show the correlation between the bulk emission and penetration depth.

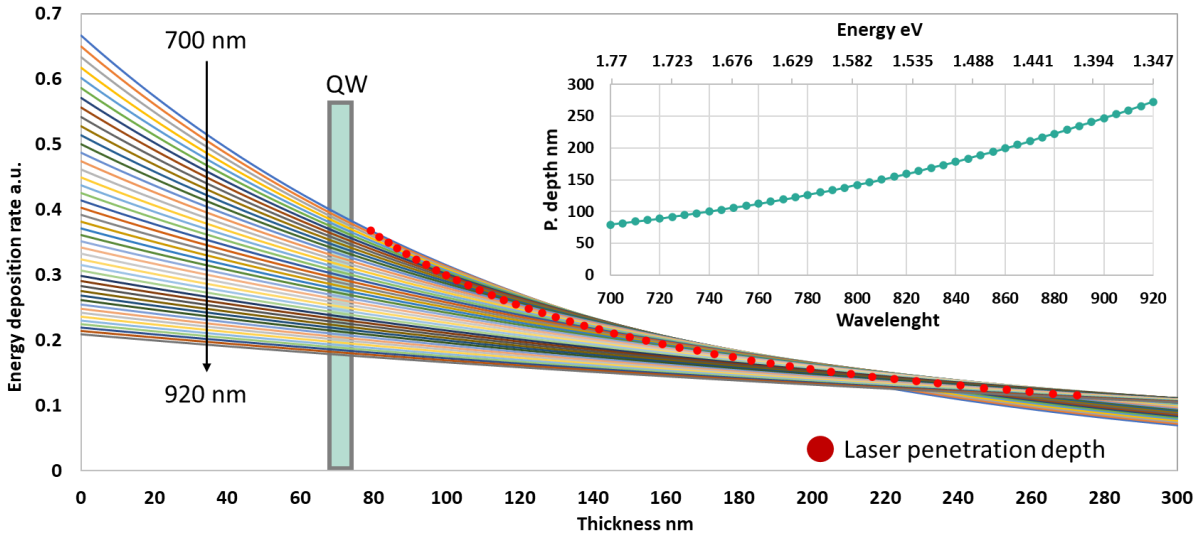

Figure 3.6 Structure thickness and laser energy absorption rate varying the excitation wavelength from 700 to 920nm. The laser penetration depths are marked by the red dots and compared with the QW position, highlighted by the grey and green rectangle. The inset shows the penetration depth with a varying excitation wavelength/energy.

3.3.2 PLE detection range

LT-PL is used to detect emission related to the n=1 quasi bound states, PLE is used to determine the energy of higher order transitions and study the higher (n=2) electron and hole confined states [105]. In the case of high J_{PEAK} RTD structures this may lead to confusion in the results. The thin and single QW RTD active region is characterized by a ML fluctuation that creates additional peaks. Line shape fitting has highlighted that these undesired peaks strongly overlap, and their intensities are comparable, making the deconvolution difficult.

In order to provide unambiguous results, careful choice of the PLE detection range is required to avoid peak overlap that may disrupt the analysis. Figure 3.7 recalls again the PL line shape fitting for the structure under analysis, this time I have added coloured arrows and rectangle to mark the 3-detection ranges of choice.

Starting from the left, the green curve is located on the Type-II peak, in the region between 0.781 eV and 0.782 eV. This detection range does not correspond to the local maximum in the raw PL spectrum, but to the expected (fit) peak for the Type-II for XML solution. In the centre of the PL spectrum, the red zone is on the bulk peak between 0.801-0.802 eV. The bulk peak presents the highest intensity compared to the surrounded peaks and I expect minimum interference from them in the PLE spectra. The last detection range is in the region between 0.815-0.816 eV, close to the peak in the XML Type-I peak. The detection energy is slightly higher than this peak energy to minimise overlap with other states. In this region there is additional overlap with the doped InGaAs tail that may confound the PLE analysis.

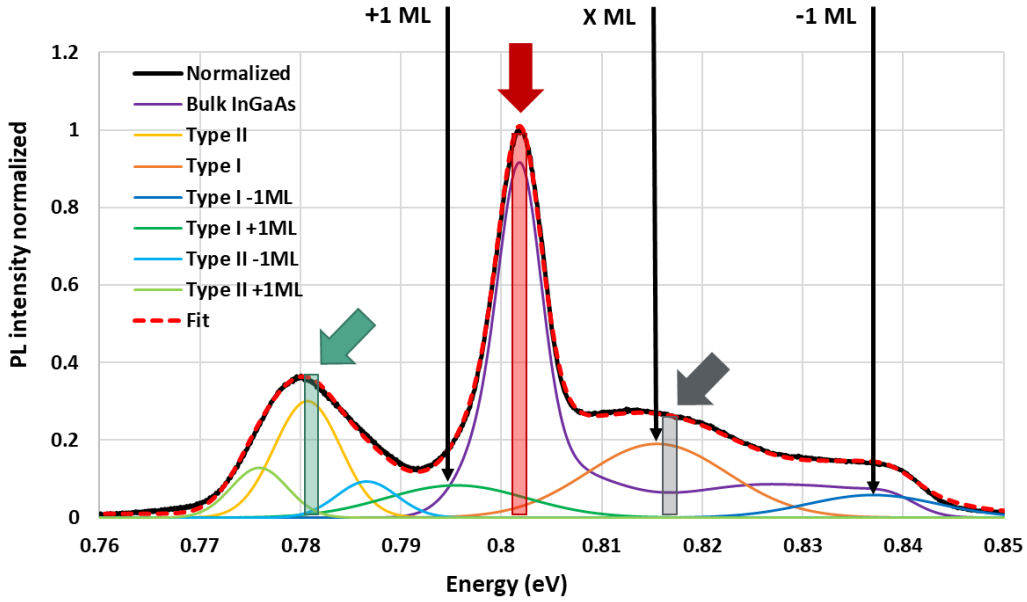

Figure 3.7 PL fitting and candidate PLE detection ranges marked by the rectangle and the arrow for sample TS1904.

Figure 3.8 shows the PLE spectrum obtained scanning around the bulk peak. With increasing excitation energy the PLE intensity decreases, in line with the predicted laser penetration depth. The graph compares the bulk PLE spectra (red) and the laser penetration depth (grey). As the excitation energy is increased, the laser penetration depth is reduced, this results in a gradual decrease in bulk InGaAs material excited by the laser. Several signal fluctuations are observed, but the peak intensity is too weak to distinguish possible features in the signal. Some of them may be attributed to fluctuations in the laser pump power or be caused by the overlapping with the doped InGaAs, the -1ML Type-I and the XML Type-I solutions.

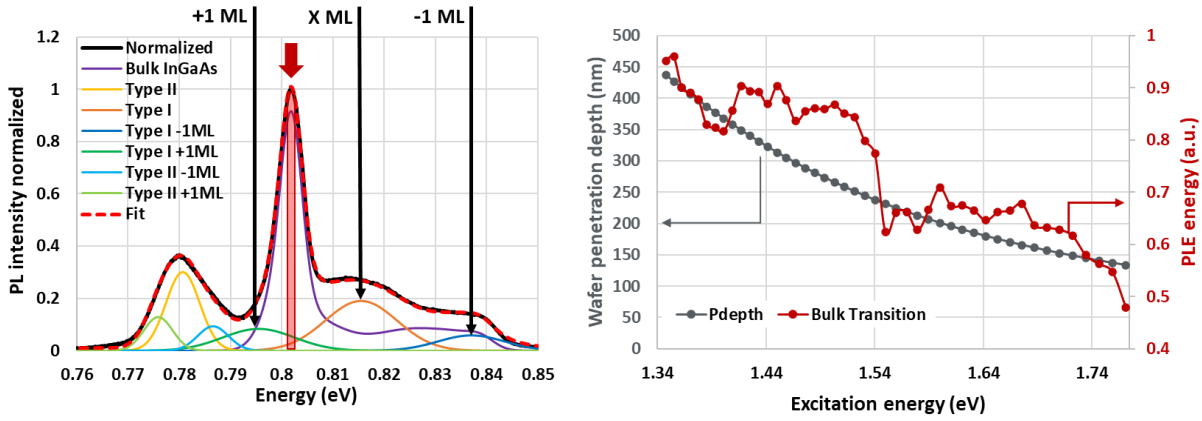

Figure 3.8 (Left) deconvoluted PL spectrum for sample TS1904 with detection energy for PLE indicated. (Right) Associated PLE spectrum and plot of calculated penetration depth (grey)

3.3.3 n=2 related transitions

In figure 3.8 I move attention to the XML emission and the graph compares the PLE detected from this detection range (0.815 eV ±0.0005 eV) with the bulk one. Both spectra have similar features in the range 1.34-1.54 eV. This is in line with these fluctuations being due to variations in the laser power, or enhanced emission from both features due to enhanced absorption in the sample. In the higher energy region (energy >1.54eV) the XML PLE spectra increase, showing a clear peak at 1.71eV. This energy value is very close to that predicted by simulation for the e2-hh2 transition. However, due to the overlap with the doped InGaAs tail in the detection window, more evidence was sought to confirm the origin of this feature.

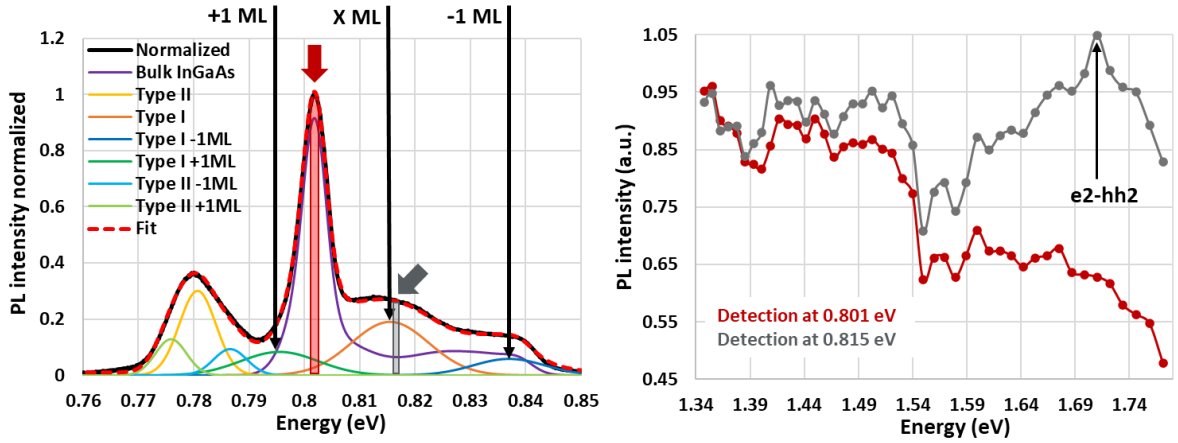

Figure 3.9 (Left) As Figure 3.8, but with detection energy selected for the e1-hh1 transition. (Right) PLE spectra for detection at the bulk transition as in Figure 3.8 (red), and the X ML e1-hh1 transition. The peak associated with X ML e2-hh2 is identified.

The last PLE trace is detected in range 0.781eV, in this range the overlap between the expected (fit) peak and other spectral features is minimized. Figure 3.10 compares the three PLE spectra, the bulk in red, the XML in grey and the XML Type-II in green. The green curve reveals a new feature at 1.42eV and the feature at 1.71eV becomes more pronounced.

The feature at 1.42eV has an energy close to the simulated e_1-hh_4 Type-I (~1.44 eV) and the e_1-hh_4 Type-II (~1.40 eV), both for the -1 ML solution. No experimental data are reported in the literature for such recombination, and the transition selection rules [84] identify these transitions as unlikely to occur. Due to the peaks overlapping in the PL spectra, this emission cannot be confirmed and is excluded from further analysis. The coincidence in energy at 1.71 eV and its enhanced prominence with reduced spectral overlap with other features, along with its absence for the bulk emission lends significant confidence that it is the e2-hh2 transition. The e2-hh2 feature exhibits a linewidth of ~50m eV. Considering the linewidth of the Type-I PL transition being ~14meV ($\Delta E/E = 0.017$) double this value is expected for the e2-hh2 transition (0.058 eV), in very good agreement with observation.

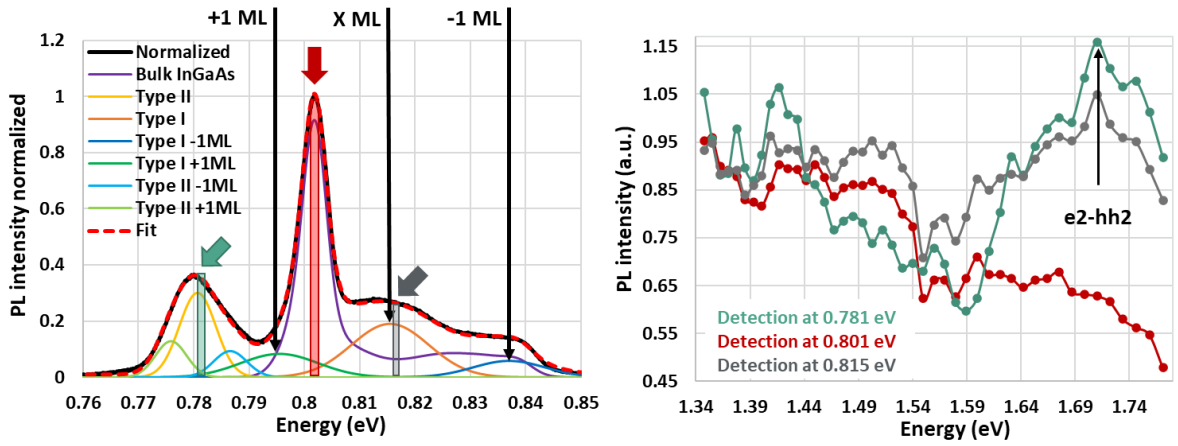

Figure 3.10 (Left) as Figure 3.8 & 3.9, but with additional PLE detection energy for the Type-II e1-hh1 transition identified. (Right) as Figure 3.9, but with additional trace for Type-II PLE. Coincidence of the peaks confirms the peak identification.

In order to add further confidence, I subsequently explored 2 additional PLE detection ranges close to the Type-II peak as a final demonstration of our findings. Figure 3.11 shows an explode view of the PL spectra and the deconvoluted peak in the range 0.76-0.8 eV, cantered on the Type-II peaks. The rectangles mark the detection ranges, 0.7805 eV ±0.0005 in grey, 0.7815 eV ±0.0005 in green and 0.7825 eV ±0.0005 in red. The detected PLE spectra are reported in the same figure using the same colour coding. The prominence of the features at 1.42 and 1.71eV reduce with increasing "crosstalk" due to the detection window having increased contribution from other spectral features.

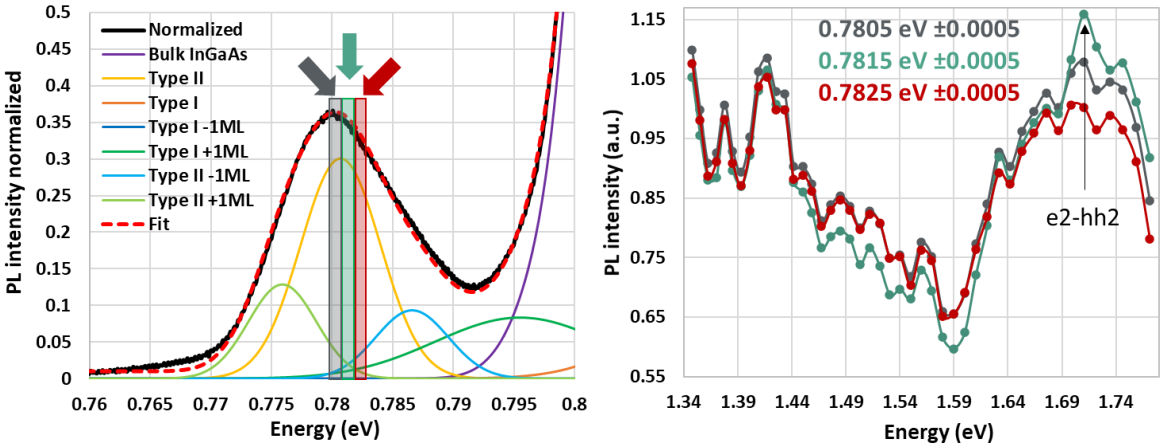

Figure 3.11 (Left) Additional PLE detection ranges around the Type-II XML e1-hh1 detection energy (corresponding to minimum overlap). (Right) Associated PLE spectra. Maximum signal intensity is obtained where minimal PL overlap is obtained.

This last analysis highlights how the simulation and the line shape fitting allow the ideal PLE detection energy range to be determined. Consequently, the n=2 quasi bound states transition can be detected to determine critical information about the conduction band offset in thin and high strained QW.

The analysis presented so far was conducted on PL spectra that presented a strong overlap between peaks due to the small ΔE between adjacent ML fluctuations. The simulation reported in chapter 2 section 2.3.3 already highlighted how this ΔE decreases when the number of well MLs increases, leading to stronger overlap between peaks. Figure 3.12 recalls the line shape fitting obtained for the second structure presented in section 2.3.3. designed with 12ML well thickness.

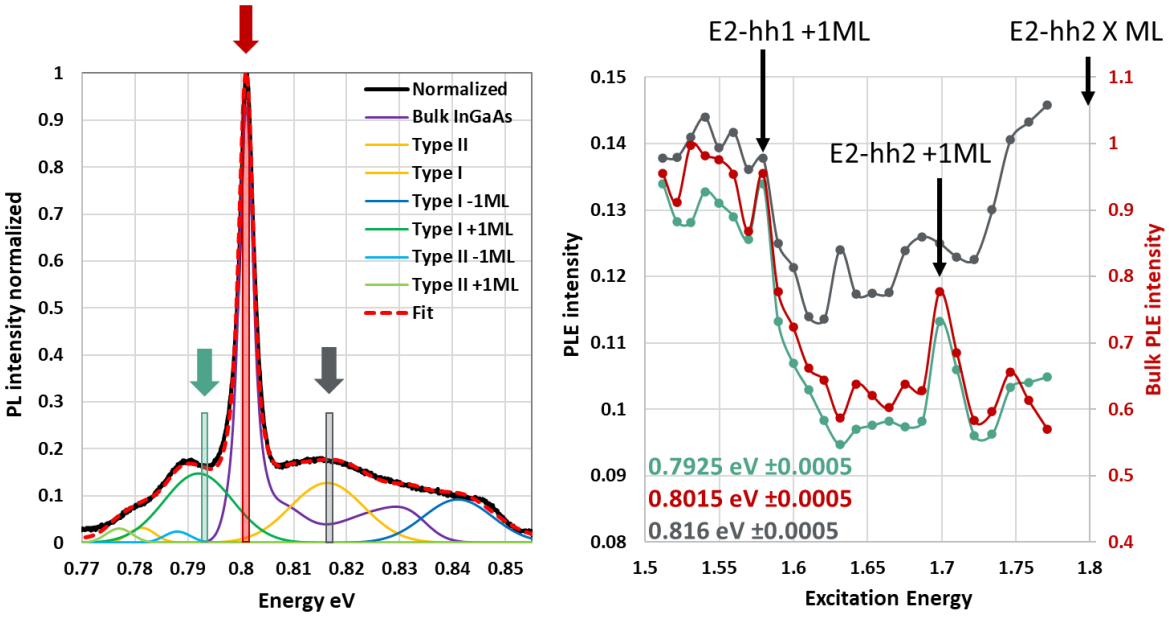

Figure 3.12 PL deconvolution, and PLE detection range for the second sample (TS2474-1). (right) Associated PLE spectra. A feature at 1.69eV is observed and associated with the e2-hh2 transition for the +1ML solution.

In order to extract useful PLE spectra, isolated PL features in the deconvoluted spectra are required making the choice of the PLE detection energies quite deferent in this particular case to those in the previous sample. With reference to figure 3.12, starting from low energy, the green range 0.7925 ±0.005 eV is positioned on the +1ML Type-I, in a region of the spectra with minimum overlap. The second range in red is again positioned on the Bulk peak at 0.8015 ±0.005 eV, as was the case for the previous sample. I note that this detection range overlaps with the +1ML Type-I peaks. The last detection range is centred on the predicted XML Type-I transition peak at 0.816 ±0.005 eV, again noting the overlap with the doped bulk tail. Based on the simulation and the characterization scheme, for a W_{TH}=13ML ±1 and [In]=86±4% the e2-hh2 transition is around 1.8eV, outside our range of observation. The -1ML transitions is expected to have a transmission energy even higher, for this reason the -1ML Type-I peak is excluded from the PLE analysis despite being in a spectral range that is potentially free of overlapping peaks. The only expected e2-hh2 PLE transition is associated to the +1ML solution, expected around 1.69eV±0.05eV (considering the ±4% in [In]).

The PLE spectra are in the range 1.5-1.77eV. The green trace (detecting the +1ML Type-I PL) exhibits a peak at 1.7 eV, in strong agreement with the predicted value of the +1 ML e2-hh2 optical transition. The red trace (centred on bulk InGaAs emission) also exhibits a feature at 1.7 eV associated with the contribution of the +1ML Type-I spectral feature to this

PLE detection band. Both red and green PLE spectra have a feature at 1.579 eV coincident with the +1ML e2-hh1 transition. The grey trace (detecting at the X ML Type-I emission) shows a qualitatively different PLE spectrum The spectrum increases in intensity to higher excitation energies, attributed to the X ML e2- hh2 transition expected at 1.8 eV that it is unfortunately out of our range of observation.

3.4 Combination of XRD, PL, PLE

The complete structural characterization has required a combination of techniques to measure critical physical parameters by XRD and electrical parameter by photoluminescence techniques, synergistically with the results obtained from simulation. Figure 3.13 shows a schematic representation of the iterative process that outputs three radiative emission energies values to finally determine an unambiguous solution.

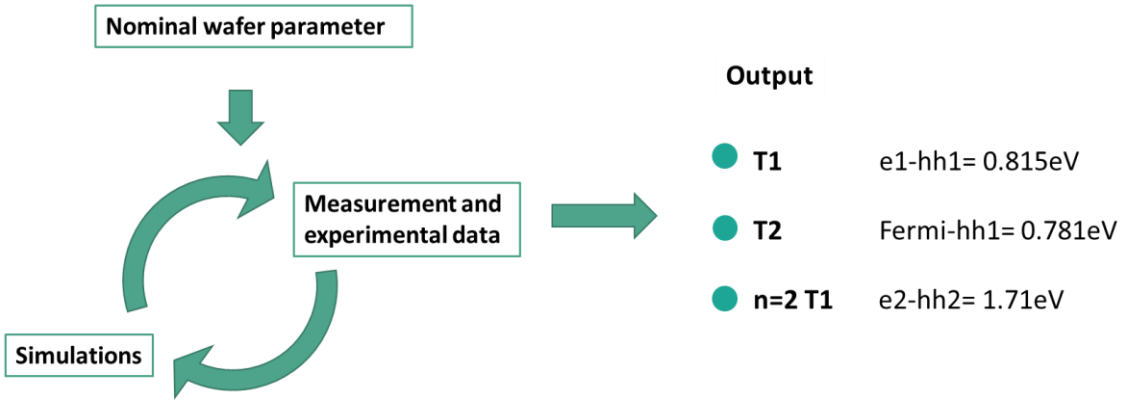

Figure 3.13 schematic of the characterization process (see text) and associated output energy values

With measured energies for Type-I e_1–hh_1, Type-I e_2–hh_2, and the Type-II transition between the bulk LM-InGaAs conduction and holes bound within the quantum well (hh_1), I am now able to uniquely determine the band-offset, quantum well width, and composition. Figure 3.14 plots the required band-offset, indium composition, and thickness of the well to realize the observed energies for the aforementioned optical transitions.

The n=2 Type-I transition is plotted by the dot-dashed line, the e_2–hh_2Type-I transition by the solid line and the bulk CB-hh1 Type-II transition by the dashed line. For a 14 ML quantum well, with 83.9% indium and a band-offset of 58.8%, I observe an intersection (marked with a red circle), indicating that these are the structural and electronic

characteristics of our structure as they simultaneously satisfy all available results for the sample.

The table shows the characterized parameters for the structure following this process. With respect to the XRD, and XRD+PL analysis, the uncertainty is drastically reduced but not eliminated due to the accuracy of the measurement system.

Accuracy in the determination of barrier thickness is around ±0.5ML. The use of a buried well increases the XRD S/N by a factor of 3dB[74], which may move the signal above the noise floor to improve the fitting. Measurement data always contains quantization noise, which may ultimately limit measurement accuracy. The accuracy in the well characterization can be made as small as ±0.5ML thanks to the combination of techniques. Optical transitions detected in PLE are more sensitive to fluctuations in well thickness (e_2-Type-I) as compared to the ones detected by PL (Type-I and Type-II). This additional energy value helps to discriminate energy shifts caused by fluctuation in the pump power, impurities in the material, and exciton broadening.
Low pump power measurement and cryo-temperatures are fundamental to keep the uncertainty low. Due to the diameter of the laser spot size and the broadening of the exciton, the measurements are spatially averaged and the accuracy cannot go lower that the reported value. More detail about this will be discussed in the next chapter. Similar considerations are applied to the QW indium mole fraction, the concentration is expected to vary of few percentage around the wafer as indium tend to accumulate in indium rich pockets[107]. More details about the indium segregation in InGaAs QW will be discussed in chapter 5. As the accuracy in determining barrier thickness, well thickness, and indium composition increases, the confidence in the PL line shape fitting is improved together with the accuracy in determining the e_1 state energy. The difference Type-I – Type-II already gives a good estimation of the e1 position, but additional information from PLE its important for the following two reason.

The Type-II transitions are not always observable, in this case the additional information on electronic level energies by the e2 transition improves the comparison with the simulation and so the characterization.

The second case is already analysed here, where all the transitions have been detected. In this case we can clearly associate the obtained e1 state energy to a combination of well and barriers thickness and molar fraction. This is fundamental for future design optimization and for design reproducibility. As already explained, different combinations of variables may give the same e1 state energy, but the RTD performance is dependent on several other variables as explained in chapter 1.

The accuracy in assessing the band offset takes into account the inevitable differences between simulation and the real structure, which is affected by the imperfection already mentioned for the well thickness and the molar fraction.

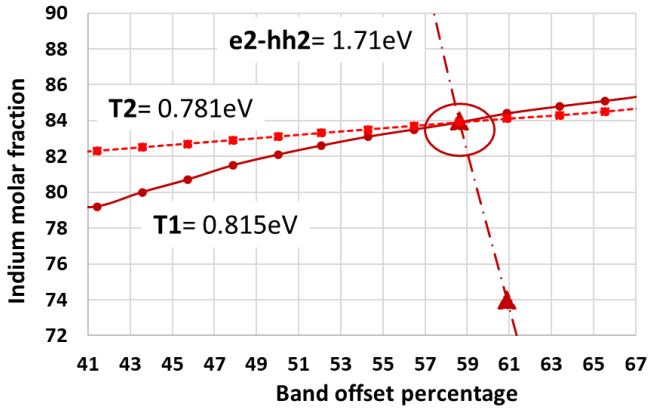

Variable	Design	Measured XRD+PL+PLE
AlAs B_{th}	4	4 ± 0.5ML
InGaAs W_{th}	15	14 ±0.5ML
QW [In]	85	84 ±0.5%
E1 [meV]	-	35 ± 2meV
Band-offset	-	59% ±1%

Figure 3.14 Contour plot showing the indium mole fraction and band-offsets required to match the experimentally observed transition energies for Type-I e1hh1 PL, Type-II elhh1 PL transitions and the PLE transition for e2-hh2 for both these transitions. The structure solution (indium composition and band-offsets give agreement for all three transitions) is marked by the red circle (see text). The table indicate the measured parameter and the associated error in structural characterization.

I now extended the analysis looking for other possible candidates that may confound this analysis (i.e. provide multiple plausible solutions). Figure 3.15 shows the previous contour-plot adding the energy values considering a 1ML fluctuation in well thickness. The green square indicates a region where possible intersection of all the energy transition may be considered. Two intersection points are marked by the black triangles and denoted as 1 and 2 that correspond to parameters that provide simultaneous solutions for 2 of the 3 observed features. Inspecting the graph the following consideration can be made. These possible intersections are related to a well thickness solution of 13ML. Both possible solutions require a conduction band offset ratio around 49%, significantly lower that any value reported in the

literature. The two intersection points are separated by a change in the indium mole fraction of 1.5%, a possible match of these solution will require an error of 0.023eV in the peaks position in the PL spectra. These three factors (no simultaneous intersection for all three observations, much lower than expected band-offset, unreasonable structural difference in the two points) are enough to confirm the 14ML as a solution for the structure but to definitely exclude these additional points, I separately assumed one of these solution as possible and I moved the analysis backwards (contour plot→PL fitting→XRD) with the following results:

A well thickness of 13 ML implies a ML fluctuation in the range 12ML-14ML

- Point-1= a line shape fitting cannot be obtained without breaking the fitting constrain
- Point-2 = with those values for the [In] and Q the 12ML Type-I transition is out from the experimental PL spectra.

On this basis we excluded these points from the solution confirming the parameter in figure 3.14 as solution for the proposed structure.

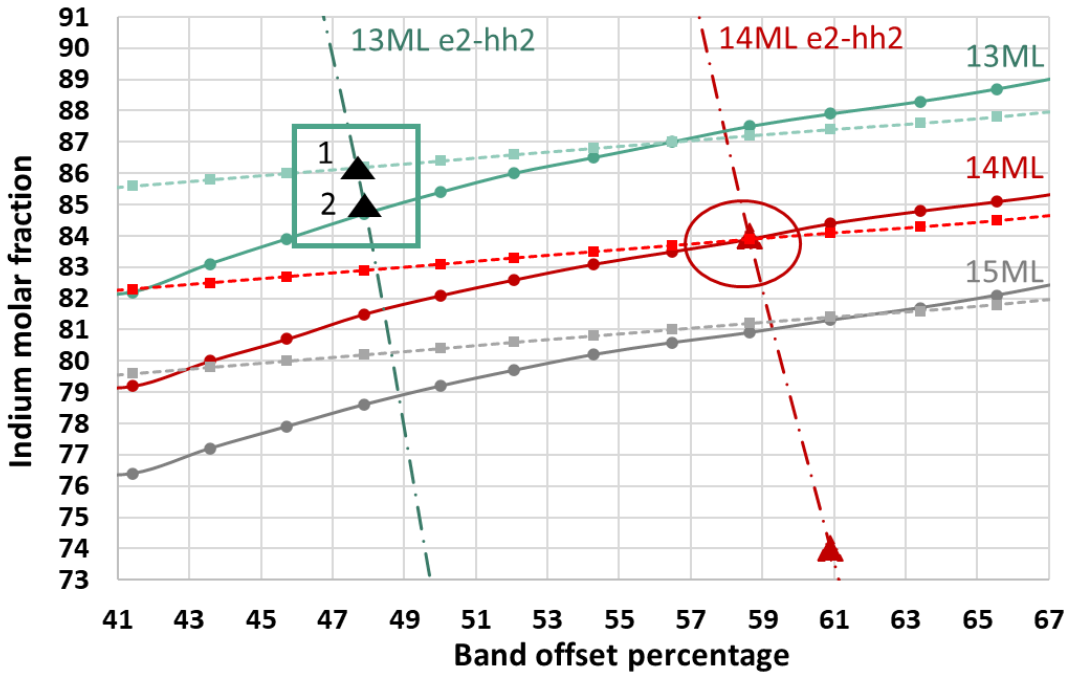

Figure 3.15 Contour plot with possible solution for the +1ML (15) and -1ML (13). Black markers indicate solution that may confound the analysis (see text).

3.4 Conclusions

HR-XRD has been used to provide a first estimation of the realised epitaxial structure which is used for simulation and LT-PL line shape fitting. The uncertainty in physical structure and electronic band-structural using XRD alone and combined XRD and PL was discussed. The importance of the band-offset has been highlighted, particularly in regard to the position of the e_1 transition energy with regard to the emitter energy level, critical for future device yield. Careful PL line-shape fitting has allowed PLE to be employed on RTDs for the first time to allow wafer level characterisation. The use of XRD, PL, PLE allows increased accuracy to the structural characterisation, and a significant increase in accuracy in determining e_1.

3.5 Future work

3.5.1 Extending the PLE excitation wavelength

The PLE study described in this chapter was conducted at the University of Kobe as part of an academic secondment. The available Ti:sapphire laser source allowed PLE scans in the range 700-920nm (1.34-1.77eV). As highlighted earlier, some of the radiative optical transition from the RTD active region are out of this range. To extend the analysis to the e_2-Type-II emission excitation energies lower than 1.34eV are required. Similar considerations are valid from the e_2-Type-I transition. As highlighted in figure 3.12, the expected e_2-hh_2 transition from sample B was outside our range of observation at 1.81eV.

As introduced in chapter 1, a high separation between the e_1 and e_2 states is desirable to increase the voltage span ΔV in the IV characteristic, and consequently the output power. Based on these considerations, future design optimization will require the e_2 state to be moved up in energy, which will correspond high e_2-hh_2 transition energy. To detect these transitions a tuneable source above the 1.77eV will be required.

A wide tuneable source may be desirable for a PLE set-up, but is also true that only a specific range of energies are of interest depending on the design under test. Therefore, for high

J_{PEAK} RTD design a PLE system should be optimized around the e_2-hh_2 transitions in the range 1.6-2 eV.

3.5.2 Band-Offset Analysis

Band offset variation as function of the mole fraction, and consequently the strain, has an important impact on the design and the simulation of those devices. The study of multiple structures with different concentration of indium (strain) can extend the knowledge of this heterostructure. Results may improve RTD device simulation, where discrepancies between the experimental and simulated IV characteristic are always observed and attributed to epitaxial variations, strain induced effects, fabrication error and ambiguous semiconductor parameters.

3.5.2 High performance THz RTD design

The e_1 state is the principal factor responsible for the device operation, and its engineering is critical for improving the output current and minimize the power consumption. The application of PLE is therefore of significance due to its contribution in the characterization of this parameter. However, to maximize all the RTD figures of merit, a complete knowledge of the active region properties is required. The e_2 state position effects the valley voltage point, to maximize the voltage span ΔV (and so the output power), so this point needs to be shifted far from the peak voltage. As described in the previous section, PLE can constitute an important tool to future design optimization.

3.5.3 Automation for Manufacturing Feedback

Chapter 2 described the PL capabilities for RTD characterization, one of them was the wafer-level scan, defined as PL map, to scan PL intensity variation around the wafer. An automated system can be designed to perform a PLE map of the sample focusing the PLE emission range around the expected (simulated) transition energy. While the emission energy can be tuned automatically by a system, human interaction is currently required to tune the system to the desired emission energy and power, this is particularly true when a wide range is required. As highlighted in these last sections, an optimized range of emission energies

informed by the simulation can reduce human interaction avoiding the need for tune the laser intensity and automate the emission energy

3.5.4 More Complex Tunnel Structures

The structures presented in this chapter are standard QWs in the AlAs/InGaAs material system. Complex structure involving InAs sub-wells are under investigation as alternative design, further work will be necessary to adapt the characterization process to these designs. The sub-well thickness is composed by few ML of InAs, too thin to appreciate by the XRD measurements. The sub well increases the equivalent indium molar fraction in the well, moving up the e_2 state energy and down the e_1 state. While the shift on the e_1 state is of few meV (similar to the one introduced by the well ML fluctuation), the shift on the e_2 state is higher, an example is reported in [39]. Based on this consideration, PLE will be more suitable that PL in characterize these structures.

Chapter IV: Micro PL characterization of RTD epitaxial structure

This chapter details a study of the characterization of the lateral extent of the ML fluctuations in the RTD active region. Previous chapters have illustrated these growth imperfections and their effect on wafer characterization. Imperfections were distinguished based on their length scale with regard to the exciton radius, but in both cases their characterization is affected by the resolution of the measurement system. XRD has a highly focused beam, but RTD XRD scans have a poor S/N ratio due to the QW thin layers. Chapter 2 discussed the line-shape fitting of macroscopic PL characterization where the PL spot sampled several/many regions of material with different quantum well thickness that contributed to the final emission spectrum. In this chapter I describe the limitation of this method and I introduce the use of a mask to reduce the laser excitation and detection spot size and increase the PL spatial resolution. The experimental data highlights the presence of long-range structural disorder in some of my structures attributed to strain induced effects. I extend my analysis of observed differences in the spatial extent of the well width fluctuations to RTD devices. A correlation between uniformity in the epitaxial perfection (i.e. no observed variation in the PL spectrum with reducing mask aperture) and scalability of device characteristics with area is observed. The results presented in this chapter were reported in [108] and [73].

The first section of this chapter introduces the ML islands and how they originate during the growth process. In the second section micro-scale PL spectroscopy is presented and used to characterize 3D growth imperfections in two epitaxial designs. The experimental data is discussed in terms of the strain relaxation limits with the help of standard mathematical models. In section 3 micro-scale PL is used to map the imperfections on a test wafer. The fourth section moves the discussion to RTD operating characteristics. Previous sections have demonstrated the presence of ML islands, leading to the possibility of large statistical distribution of the electrical properties of devices based upon how the device mesa samples the epitaxial structures. This chapter demonstrates he connection between a strong spatial variation in the emission spectra and hence local electronic band-structure and randomness in the RTD device operating characteristics that leads to a loss of scaling of certain

parameters with device area. Section 5 summarise the additional insight gained by employing micro-scale PL and section 6 describes future improvements and work.

4.1 Macro scale vs Micro scale

Is PL on a micro scale equivalent to PL on the macro scale?

Section 2.4 presented the QW imperfections differentiated by their length scale, the barrier roughness (length scale < exciton diameter), the ML-fluctuation (length scale > exciton diameter), and their impact on PL characterization. Considering the ML fluctuations, no information about the length scale beyond ">exciton diameter" is extracted. Only the relative frequency/population of regions of different terrace heights can be deduced through comparison of the line-shape fitting results. Figure 4.1 recalls a schematic of the QW imperfection and shows a 3D representation of the ML regions on a RTD sample and the broadening on the PL spectra. ML regions are highlighted using different colours, -1ML regions in red, XML regions in grey and +1ML regions in green. The origin of each peak in the PL spectra is marked by using the same colour coding and the vertical arrows. Apart from the doping concentration, macroscopic PL wafer mapping (100µm diameter excitation/detection) does not show a change in the PL spectra when changing the measurement point, this indicates that standard macro-PL cannot excite and detect emission from one ML region alone. It does indicate that ML fluctuations occur on a length scale <100um. Summarising knowledge of the length scales involved, ML fluctuations occur in islands/terraces of scale >20nm, and <100um.

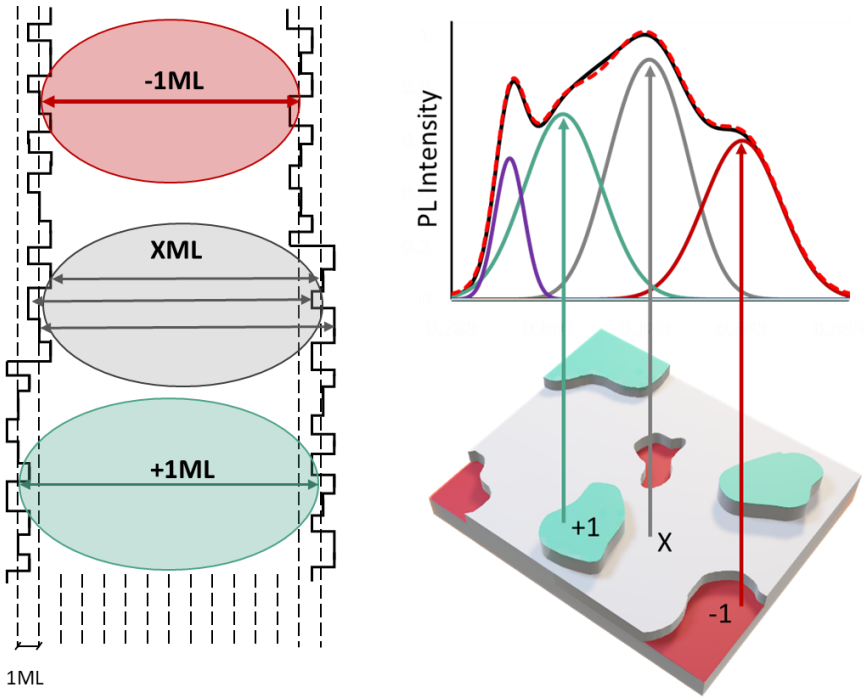

Figure 4.1 (Left) Schematic of interface roughness and ML fluctuation in the QW. (right) 3D schematic of the ML island and impact on the PL spectra .

The case of study is represented schematically by figure 4.2. Starting from the left, the picture shows the wafer and incident laser beam. The central image shows a focus on the wide laser spot size with an average area of ~300-100um^2, depending on the measurement condition and the pump power. As a result, multiple regions are covered and excited by the laser spot (green circle). Finally, the picture on the right highlights the sample response, the total luminescence is the sum of the emission from the different regions excited. As consequence the information given by the experimental PL spectra (and associated electronic band-structure) are spatially-averaged. This highlights the origin of the question proposed at the beginning of the chapter.

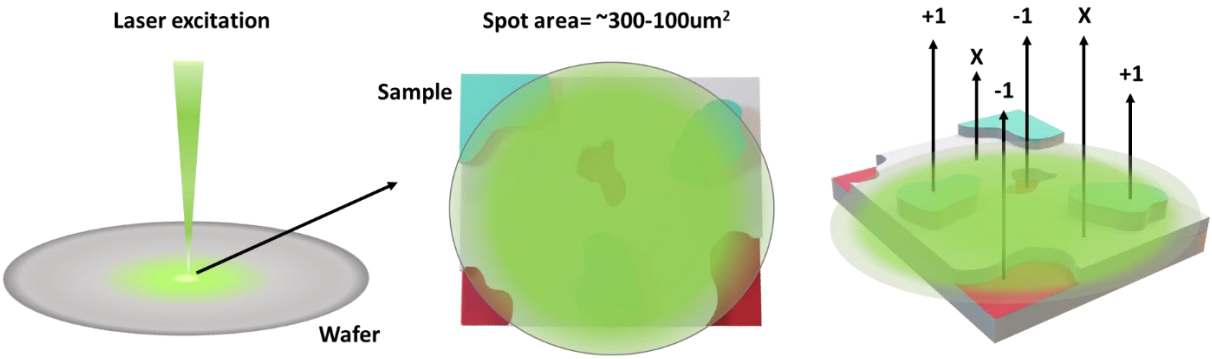

Figure 4.211 Schematic representation of macro-PL where the large laser spot is incident on the wafer and excites multiple islands at time.

4.1.1 ML fluctuations

Interface roughness and the formation of terraces of different height were observed to be dependent not only on the material system in use but also by the growth order. AlGaAs growth on GaAs has shown good heterointerface quality, the inverted heterointerface has proved to be rough [109-112].

Luminescence studies have indicated that heterointerface roughness disappears in favour of the formation of ML terrace using an interruption in the growth of AlGaAs on GaAs[113]. The origin of the roughness is been attributed to surface segregation of impurities from the Al source[114] and from the substrate[115]. Rough interfaces and terraces were observed in InGaAs/InP at high growth-rates due to non-integer ML growth[116]. Additional peaks were observed by PL[117] and by cathodoluminescence[118] corresponding to non-integer well thickness ML solutions.

4.1.2 Strain-induced imperfections

Quantum well imperfections are caused by several factors such as the substrate temperature[119], the growth techniques[120] and strain conditions [93]. Process optimization can eliminate/compensate for the systematic errors introduced by the reactor, but careful analysis is required when the structure is under high strain conditions. The relaxation of strain in epitaxial layers is a phenomenon that has gained importance with the growing application of highly mismatched materials in micro and nano electronics. Atomic

layers are formed on a semiconductor surface starting from the nucleation and the formation of 2D regions distributed along the plan of the surface[121]. Above a certain lattice mismatch and increasing thickness of the deposited materials, the 2D growth changes to 3D with the formation of 3D “island” regions [82], which may be caused by the strain relaxation to lower the energy of the system[122]. While in some cases the formation of islands is desirable, for example in the formation of self-assembled quantum dots, this phenomenon is undesired and represents an imperfection that can lead to crystal defect and consequently compromise the devices.

4.1.3 Layer thickness limitation for the AlAs/InGaAs/InP material system

The coherent growth of strained layers upon a substrate without the formation of imperfection is a key challenge for epitaxy, and worst-case scenarios are the formation of dislocations and/or interstitials. To the best of my knowledge, a model to simulate the undesired formation of islands has not been established at the time of writing, but two models are available to investigate the growth limit for the formation of dislocations. This limit is known as the *critical thickness* (Tc), defined as the maximum achievable thickness of a material X pseudo morphically grown on material Y. Figure 4.3 shows the critical thickness limits for the InGaAs/InP material system calculated applying the mechanical equilibrium model by Matthew and Blackeslee (in grey) [123] and the energy equilibrium model by People and Bean (in green) [124]. The graph plots the critical thickness expressed in Å varying the In mole fraction from 0 to 1. The second x axis on the top of the graph indicates the lattice mismatch with respect to the InP substrate expressed as a percentage. The P&B model gives a considerably higher value for the critical thickness, with experimental data having shown that the critical layer thickness is somewhere between both models [125-127].

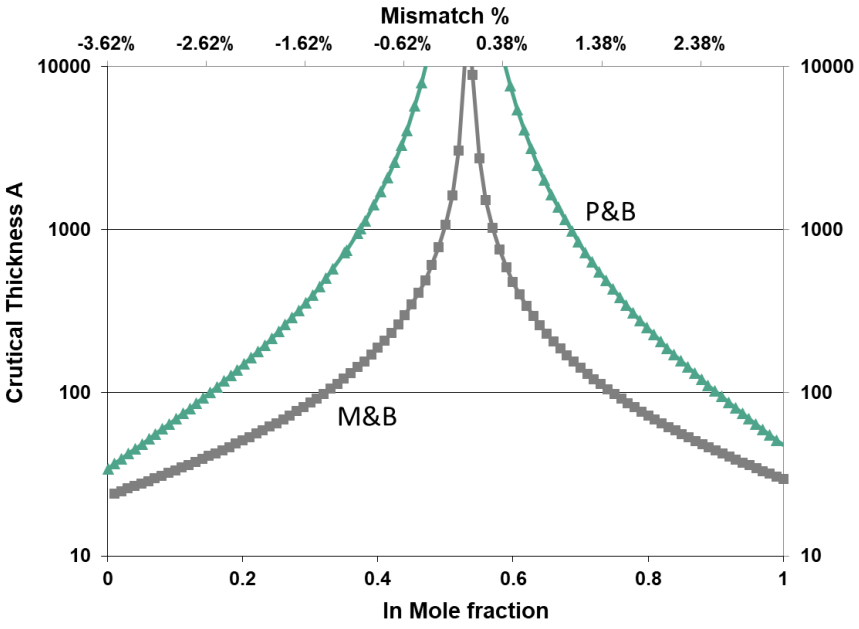

Figure 4.3 InGaAs on InP Critical thickness varying the In mole fraction. M&B model in grey and P&B model in green. Thickness reported in Å on log scale.

For a perfect lattice matched condition (In=0.532) the critical thickness is infinite and rapidly decreases to under 10nm when the In mole fraction is pushed to 0.9. This [In] range highlights the difference between the LM-InGaAs and highly strained InGaAs (In> 0.7), both present in our RTD structure as bulk and QW material respectively. As highlighted before, the critical thickness is considered as the limit after which the formation of dislocations is enhanced. For very thick strained layers the material may relax to the point the lattice constant does not match that of the substrate (plastic deformation). On this basis, it may be expected that more ML islands and corrugation of the surface may occur as the layer thickness approaches the critical thickness, followed by an increase in defect density as thickness is further increased.

The graph shown in figure 4.3 was obtained considering only the InGaAs/InP material system, it is important to include the role of our AlAs barriers in balancing the overall strain within the quantum well. AlAs has a lattice constant of 5.6611 Å, lower than the InP (5.8697 Å). With respect to the InP, the AlAs introduce a tensile strain while for InGaAs (In>0.532) the strain is compressive. This means that the overall stress in the QW can be compensated (or fully balanced) to surpass the limit imposed by the critical thickness. The concept has been successfully applied for the strain compensation and growth of thick multi QW stacks [128-130].

This model was previously investigated for the AlAs/InGaAs/InP material system to simulate and optimize the intrinsic resonator efficiency in high current density RTD design[39]. Figure 4.4 combines the InGaAs and the AlAs limits to calculate the critical thickness of the overall QW system. The graph shows which combination of QW thickness (expressed in ML) and indium mole fraction can be grown without a significant increase in misfit dislocations. The region in green is the where the growth is considered "safe". The grey zone is an extension of the previous one where the tensile AlAs barrier compensates the compressive InGaAs strain. The graph is obtained considering the limit of 4 AlAs ML. The red zone exceeds the calculated limit and where the growth may be possible, with the risk of introducing an increasing number of defects that may result in poor device performance.

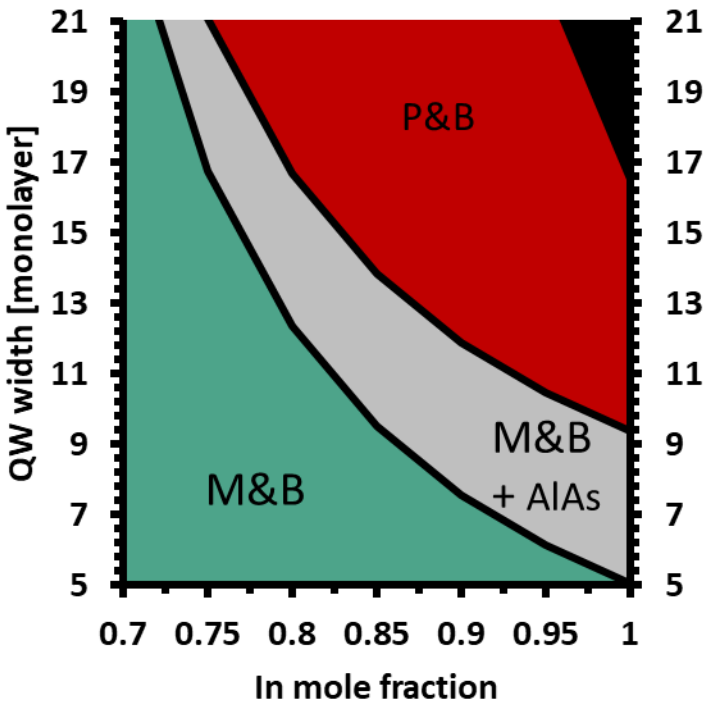

Figure 4.4 Modelled schematic of the critical thickness limits for QW width and crystalline alloy mole fractions, The green zone indicates uniform growth, grey region indicates uniform growth under strain-balancing, the red region exceeds the mechanical-equilibrium theory where an increase in dislocation density is expected.

4.2 Micro PL

ML islands have been analysed using luminescence techniques, and the most informative results have been obtained by cathode luminescence spectroscopy (CL) [67]. This technique is based on a scanning electron microscopy and offers high spatial resolution mapping thanks to the use of the electron beam (diameter 10nm) as the excitation source. Scanning the sample, different CL emission is detected depending on the thickness of the QW. Scanning an entire sample surface, Christen *et al* [68] obtained a complete mapping of an AlGaAs/GaAs sample that highlighted the presence of the ML islands, some of them with a lateral extension greater than $2\mu m^2$.

For the InGaAs/InP material system, under high strain conditions similar results were obtained using atomic force microscopy [131]. Resolution like the one offered by CL (10nm) cannot be reached using the PL system, but a lateral resolution of few micrometres (or around one micrometre) can be obtained and still be useful for a qualitative analysis of the ML islands.

Figure 4.5 shows a representation of the effect of a progressive reduction in spot size, ML islands are marked by the numbers, PL intensity is represented schematically by the black arrows. The goal is to reduce the spot size to isolate a small portion of the sample and reduce the background emission, moving from the left to the right the intensity of the ±1 ML island is reduced in comparison to the XML.

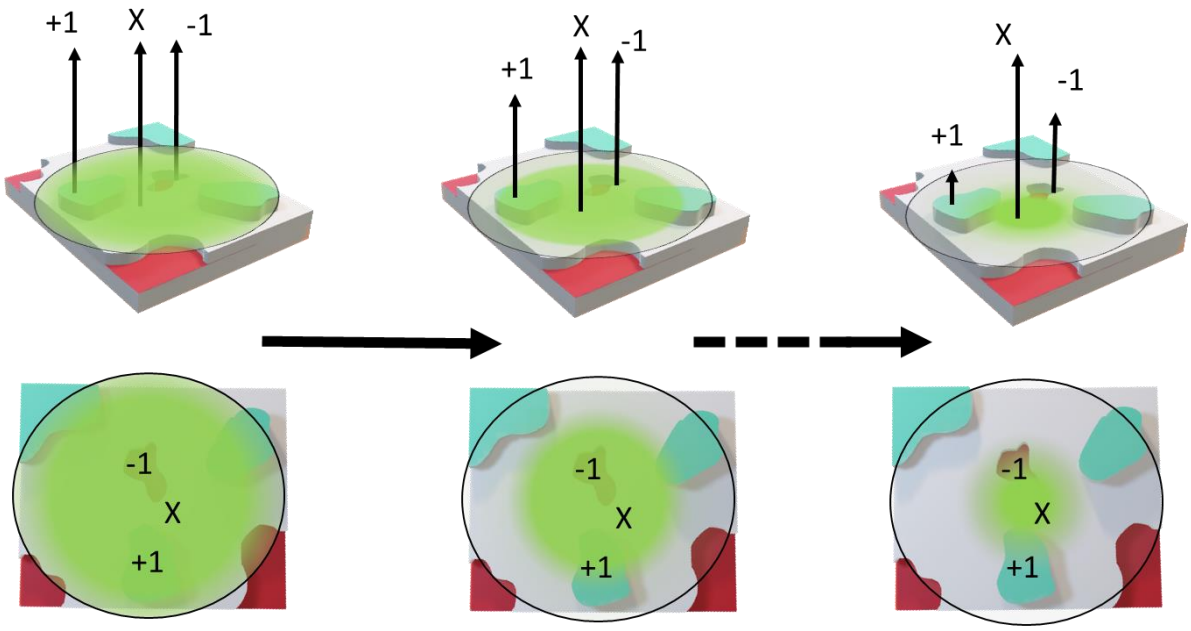

Figure 4.5 Laser spot size reduction concept. From left to right the pictures show the progressive spot size reduction and the ML island involved in the PL emission.

4.2.1 Micro-PL mask design

Improvement in the spatial resolution of the PL system is limited by the measurement conditions imposed by the RTD wafers. The use of a cryostat is fundamental to obtain a useful PL signal from samples, but the cryo-chamber creates a physical limit to the distance between the collimator and the sample on the stage. This precludes the use of a very high numerical aperture lens to improve the spatial resolution of the system. Even including this possibility there are other consideration that we need to consider. The PL system directs the laser light on the sample using a collimator, the incident light is focused on a spot of discrete dimension where the intensity profile is assumed to be Gaussian (i.e. greater at the centre and decreasing near the edge). Spatial resolution is therefore not a unique, well-defined parameter. Complete control of the light hitting the sample is needed. Apart from using a confocal microscope and spatial light filter, suffering from the issues above related to numerical aperture, two approaches were considered. The first one was to develop a series of fabrication process to create pinholes in a surface metallization layer. This presented several inconveniences, the most important was related to my effort to maintain the characterization as non-destructive and to limit human interaction/sample preparation (time consuming)/sample waste. The second option was to use a photolithography mask with a

pattern composed by several holes and markers to help with the alignment, and place this in contact with the epitaxial wafer surface.

Figure 4.6A show a schematic representation of the pattern imprinted on the mask. The designed pattern has 19 different holes, with dimensions providing areas from 100 to 10 μm^2 (step of 10 μm^2) and from 9 to 1 μm^2 (step of 1 μm^2). Each element in the pattern is separated by 300 µm to avoid any PL-contribution from more than one source. The mask is a common commercial 3 x 3 x 0.006 in. chrome/quarts photolithography mask. The pattern was repeated on areas <0.5 cm^2. The measurement set up is shown in figure 4.6B, to fit in the cryostat, a 5mm x 5mm piece of the mask was diced from the mask and positioned on the top of the sample.

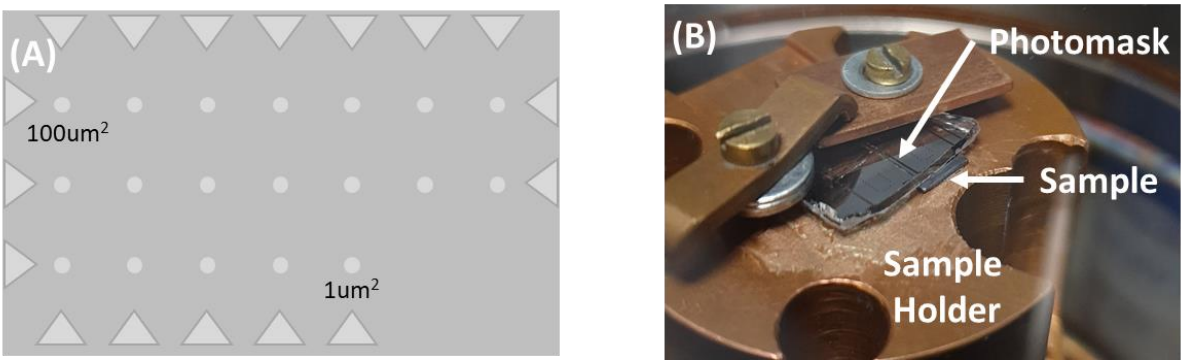

Figure 4.6 (A) Mask pattern design, pinholes and triangular markers for aligment. (B) photograph of the measurement set-up, from the top:copper blocking system, mask, sample and sample holder.

Figure 4.7 shows a schematic that illustrate the two possible mask mounting configurations. Diffraction effects are expected considering small apertures, extending the excited area beyond the aperture edges. The photomask and the chrome absorber have the task to limit both the excitation and detection region; consequently, unwanted lateral PL emissions from the pinhole surrounding area are blocked by the chrome absorber. To eliminate possible multiple reflections between the quarts and the sample, I chose configuration A with the photomask positioned with the chrome absorber on the top of the sample.

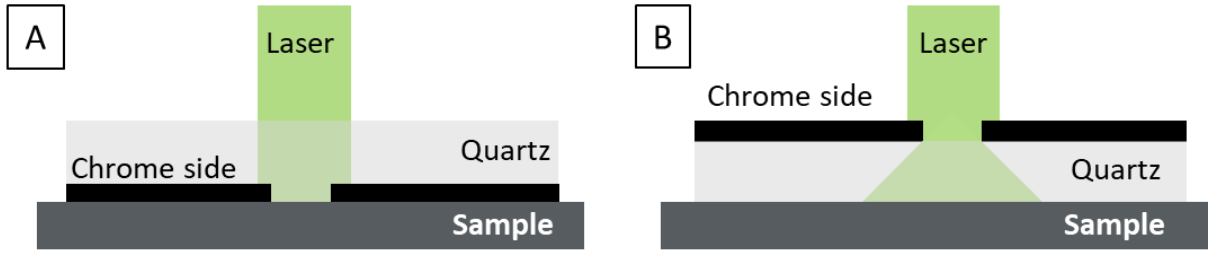

Figure 4.7 Mask mountimg configuration, (A) crhome absorber on the sample, (B) crhome absorber on the top. Configuration B may result in diffraction effects and poorer spatial resolution.

4.2.2 Micro PL measurement

Low-temperature PL was performed in a closed-cycle helium cryostat, with the sample at a temperature of 13K. A frequency doubled neodymium-doped yttrium-vanadium-oxide (Nd:YVO4) laser at 532 nm was used to excite the sample. The PL signal was filtered by a double-grating Bentham DMc150 monochromator and detected by an InGaAs trans-impedance photodetector. Measurements were conducted using a laser power density of ~0.5 mW/cm^2 with the photomask varying the excitation/detection spot size. The first sample under analysis has a QW thickness of 12ML and an indium mole fraction of 85% labelled as “sample A”. Figure 4.8 shows the PL experimental spectra obtained by varying the hole dimension. Curves are normalized and shifted in amplitude to help the reader. The holes reduce both the excitation and the detection area, and therefore affect the PL intensity. Data are normalized to focus attention on the changes in the overall PL line shape rather than peak intensity. Peak intensity and their differences will be analysed later in this chapter. Starting from low energy, a peak at 0.8eV is visible, associated with the bulk transition. Moving to higher energy the spectra is broad due to the ML fluctuation, as already explained in the previous chapters. We observe that with reducing the hole area, essentially identical spectra are obtained. The dominance of the bulk transition is observed to reduce with reducing holes size, but down to a 4 μm^2 hole size the contribution of the XML and +1 and -1 ML type-I transition remains almost unchanged. It is worth mentioning that the bulk transition (0.8eV) corresponds to a wavelength of 1.5μm, which is proportional to the diameter of the smallest area windows in the mask. This may cause diffraction, affecting the detection. This may contribute to the intensity reduction observed in the scans. The PL intensity seems equally distributed between the Type-I peaks. For the smallest hole used of 1 μm^2, small changes in the relative peak intensities are observed.

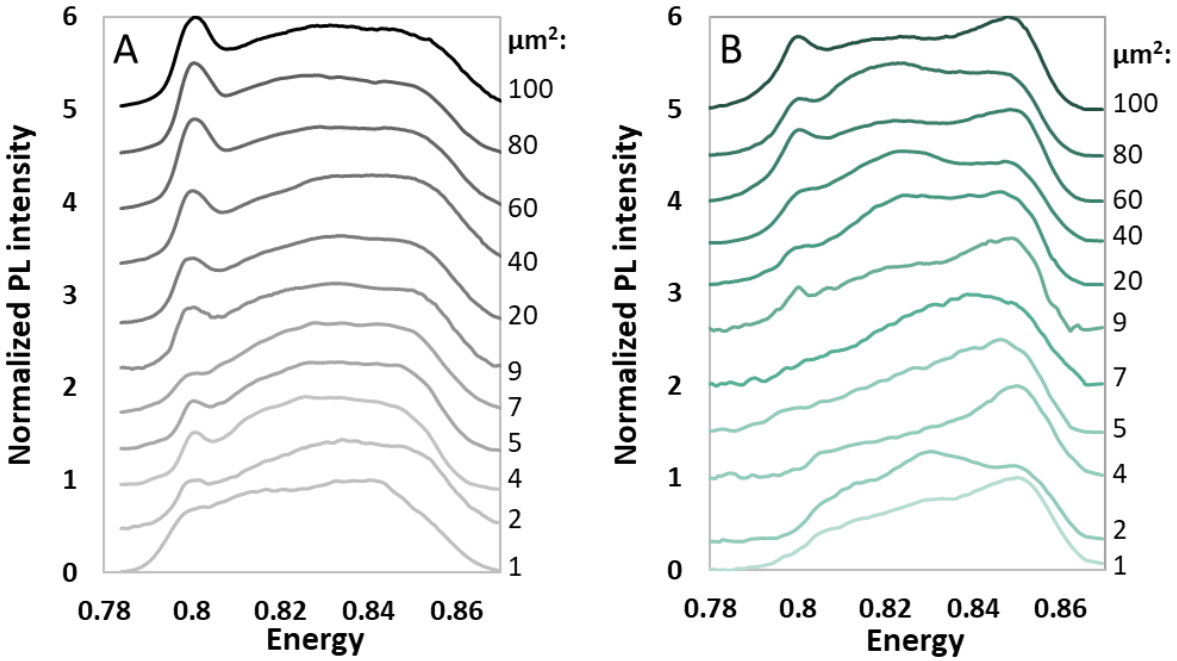

Figure 4.8 Experimental PL data from sample A (TS 2474-3) (A) and sample B (TS 2484-1) (B) reducing the laser spot-size, with the corresponding window dimension reported on the rightside. Spectral data normalized and offset for presentation purposes.

Figure 4.8B shows the micro PL results obtained from a second sample that has a QW thickness of 16ML and a In mole fraction of 80% and labelled as "sampleB". With respect to the previous sample, the dominance of the bulk transition is again observed to reduce with reducing hole size and disappears after a hole area of 9 μm^2. Strong changes are observed in the Type-I peak intensity with decreasing hole size. The peak at 0.85eV, associated with the -1ML thickness is persistent while reducing the area of observation, indicating a predominant distribution of this thickness. The length scale of this long-range disorder is observed to be quite different in these two samples. For sampleA this long-range disorder lengthy scale is 4 μm^2 as it shows PL line shape differences for a hole dimension lower than 4 μm^2. For sample B differences were observed already after the 100μm^2 area holes, the attributed length scale disorder for this sample is therefore around 100 μm^2. From these measurements we cannot measure the average dimension of the ML islands, but the line shape differences highlight the level of uniformity of the wafer. Multiple measurements were performed on other parts of the sample with similar results. At the current stage, I cannot scan the exact same spot on the sample whilst decreasing the aperture dimensions, as the mask is pressed on the sample, and holes are distributed on an area~0.5 cm^2. However, micro-PL variations are observed by scanning multiple regions of the wafer, highlighting

that the disorder is equally distributed on a macroscopic scale (wafer level), but additionally, randomly distributed on a microscale.

4.2.3 Strain Induced non uniformity

The growth conditions for the two samples were nominally identical, and therefore, these differences in PL (and hence structural uniformity) are attributed to the structural design itself. The active regions are highly strained, which is known to lead to corrugation of the growth plane prior to defect formation[123]. For the coherent growth of strained structures without the formation of dislocations, the limit has often been described in terms of the critical thickness, as discussed in section 4.1.2. Figure 4.9 recalls the calculated limits with the addition of markers to indicate the position of the samples characterized by micro PL. Sample A is approximately in the middle of the grey region while sample B is close to the extended limit obtained including the 4ML AlAs barrier. The calculations are made considering the worst-case scenario where only the first barrier strain compensates the well. During the growth process, the InGaAs is deposited on the first AlAs barrier, this barrier alone has to balance the QW 16ML stress until the second barrier is complete, and for highly mismatched designs, imperfection are more likely to occur[132]. This relative stack of MLs is more exposed to strain-induced relaxation [133] leading to the formation of islands [134].

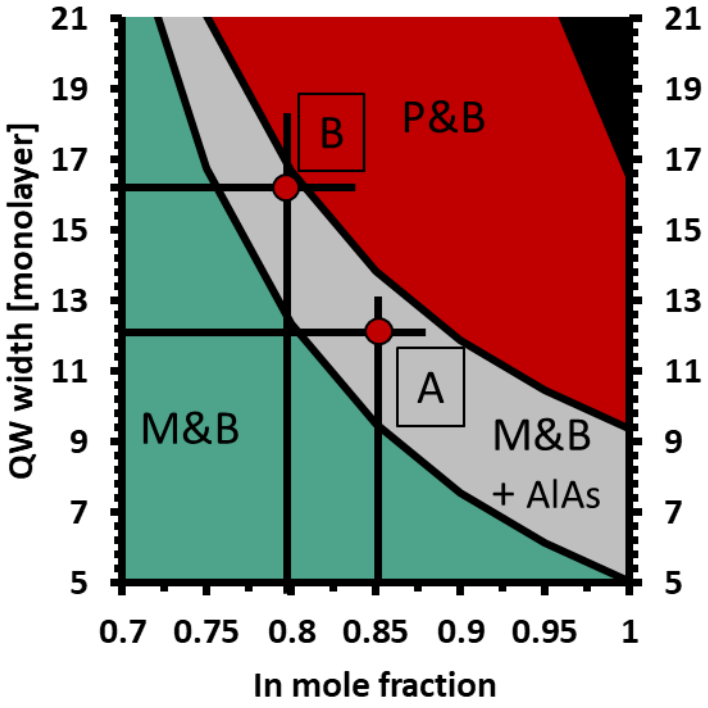

Figure 4.9 Same as 4.4, black lines and red dots are marking the position of sample A (TS 2474-3) and B (TS2484-1). Sample B is close to the modelled thickness limits.

In an attempt to provide a rigorous derivation for the strain balance criteria Ekins *et al.* developed the "zero stress method" based on the average in-plane stress derived from each strained layer adds on the overall stress of the stack [81]. The method is represented by the following formula:

$$a_0 = \frac{A_1 t_1 a_1 a_2^2 + A_2 t_2 a_2 a_1^2}{A_1 t_1 a_2^2 + A_2 t_2 a_1^2} \qquad \text{(eq. 4.1)}$$

Where:

- a_0 is the lattice constant of the substrate
- t_1 and t_2 are the thickness of the two layers
- a_1 is the lattice constant of the material 1
- a_2 is the lattice constant of the material 2
- A_1 and A_2 are the elastic stiffness coefficients for material 1 and 2 respectively

Starting from the desired QW characteristic (a_1, a_2, t_1, t_2) the formula indicated the theoretical ideal substrate lattice constant that balance the stress of the above layer. The limits imposed by this formulation are simply given by the impossibility in tuning the substrate characteristic. The formulation is applicable on structures grown on compliant and virtual substrates [81]. The above formula is derived by the average in-plane stress, caused by the biaxial strain in the combination of two layer and expressed by the following formula:

$$X = \frac{2}{t_1+t_2}\left(t_1 A_1 \varepsilon_1 + t_2 A_2 \varepsilon_2 \frac{a_1}{a_2}\right) \qquad \text{(eq. 4.2)}$$

Where:

- ε_1 is the strain component for material 1 calculated with respect to the substrate $\varepsilon_1 = \frac{a_0 - a_1}{a_0}$
- ε_2 is the strain component of the material 2 calculated as $\varepsilon_2 = \frac{a_1}{a_2}\varepsilon_1 + \frac{a_1 - a_2}{a_2}$

The stress limit that a structure can tolerate can be calculated combining the zero stress and the M&B model using the critical thickness as a limit. Assuming 4ML of AlAs barrier as material-1 and the InGaAs as material-2, figure 4.9 shows the in-plane stress varying the Indium mole fraction for 7 values of well thickness, from 10 to 17MLs. The graph focuses in the Indium mole fraction range from 0.7 to 1, as done for the graph in figure 4.8. Above zero the stress is tensile, below the zero the stress is compressive. The tensile AlAs barrier is the base and it compensates the compressive stress of the InGaAs. The cross markers are indicating the corresponding in-plane stress values calculated using Tc in the above formula (eq. 4.2). These are the limits under what we can assume the strain stress is too high to be tolerated by the structure and the curves are then indicated in black. The red triangles are highlighting the position of the two sample: sample A is near the x axis and so the strain balance condition, Sample B is close the limit indicated by the black cross for a 16ML structure. For sample B we calculated an in-plane stress of 0.00458 N/Å^2 against the limit of 0.00533 N/Å^2. This mathematically quantifies the stress in the structure, and explains the observed difference in long-range disorder observed experimentally.

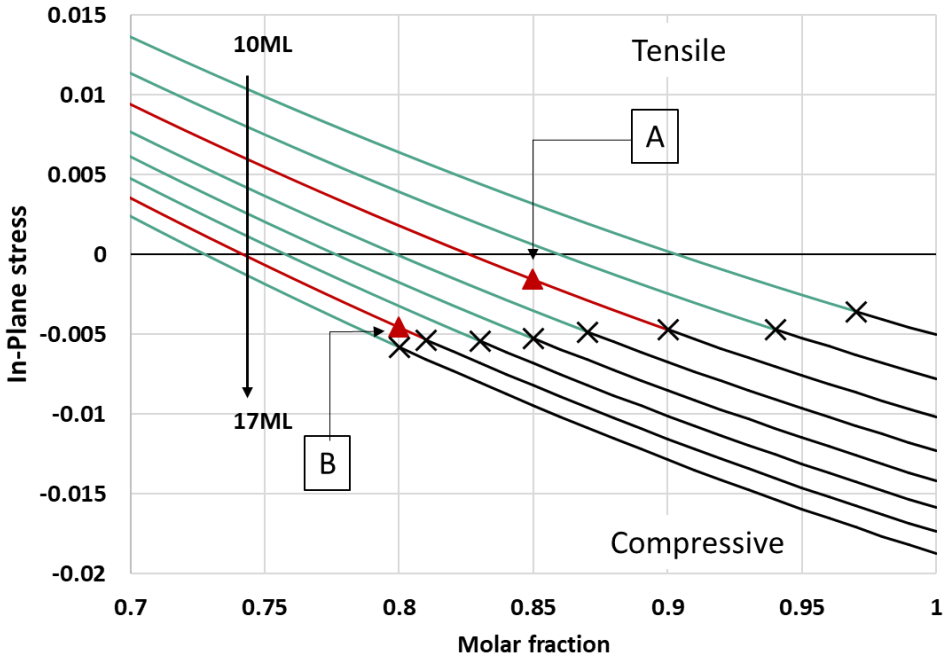

Figure 4.10 In plane stress calculated varying the molar fraction for well thicknesses from 10 to 17MLs. Red curves are highlighting the well thicknesses of the samples under test. X markers are indicating the in-plane stress values using the critical thickness calculated by M&B in equation 4.2 (see text).

4.3 Micro PL mapping

As I have demonstrated that PL is different moving from a macro to a micro scale the same can be extend for PL mapping. The designed mask offers a maximum area resolution of 1 μm^2 that we used to scan multiple point of the sample. We expect changes in the PL line shape moving from one point to the other, to quantify these differences the PL line shape fitting is used to deconvolute the peaks and micro-PL spectra were recorded from regions separated by several millimetres. Results are reported in the graphs in figure 4.11. Measured PL spectra are reported in black, and each micrograph shows a different line shape, confirming differences in the peak amplitude around the sample.

Fitting results are indicated by dashed red lines, purple lines indicate the doped InGaAs and the bulk LM-InGaAs, the Type-I components are indicated in red (-1ML), in grey (XML), and in green (-1). Lead by simulation, the XML peak is positioned at 0.825eV, the +1ML at 0.799eV and the -1ML at 0.843eV. The fitting is obtained using a Gaussian peak with a linewidth, $\sigma T1=7$ meV for the Type-I transitions. Type-II peaks are not observable in this sample. Horizontal coloured dashed lines are positioned to indicate the maximum intensity

reached by the -1ML, XML and +1ML peak respectively. The lines are also positioned to compare the peaks intensity between the 4 graphs. The fittings are obtained fixing the peak position on the energy axis and only regulating the peak intensity.

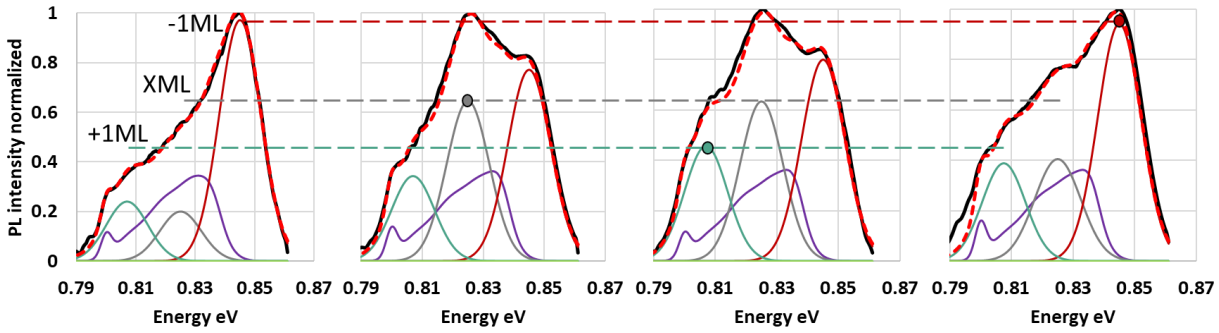

Figure 4.11 Micro-PL spectra (Black) and line shape fitting (red dashed line) from 4 different parts of the wafer with a spot size of 1μm^{2}sample TS2484-1

Figure 4.12A shows a standard macro scale PL (black line) and the four micro-PL curves for the sample, presented in figure 4.11. Data are normalized for comparison. For the macroscopic case, starting from the lower energy side of the spectrum, the bulk peak at 0.8 eV is strong, and at higher energy, the PL intensity is distributed between all the 3 Type-I peaks. The Bulk transition is weak in the micro-PL scans and the Type-I emissions have different intensities, depending on the ML island covered by the laser spot size. As mentioned previously, the emission wavelength is similar to the dimension of the holes in the photomask, and scattering may contribute to reducing the peak intensities. As no random fluctuations are observed in sample A, I omitted scattering from my analysis. Results presented in figure 4.11 for sample B are in line with fluctuations caused by long range imperfections in the QW rather than errors within the experimental set-up. It is noteworthy that a complete deconvolution between the reduction innintensity due to scattering and epitaxial imperfection is impossible. The schematic in figure 4.12B shows a macroscopic PL spot size, represented by the black dashed line and it is compared with two representative micro spot sizes, (black lines). ML islands are distributed uniformly on the wafer surface and their extension is arbitrary[108]. On this basis, each micro spot may cover multiple ML islands but in different proportions, the resulting spectra are characterized by the ML peak of the most covered island. As an example, we focus the attention on the red line in figure 4.12A (microPL-3), where the spectra is dominated by the -1ML transition at 0.84eV. For this curve we can assume a spot size like the one indicated as micro-1 in figure 4.12B, this area covers in great part a -1ML island and its contribution to the PL spectra is the highest.

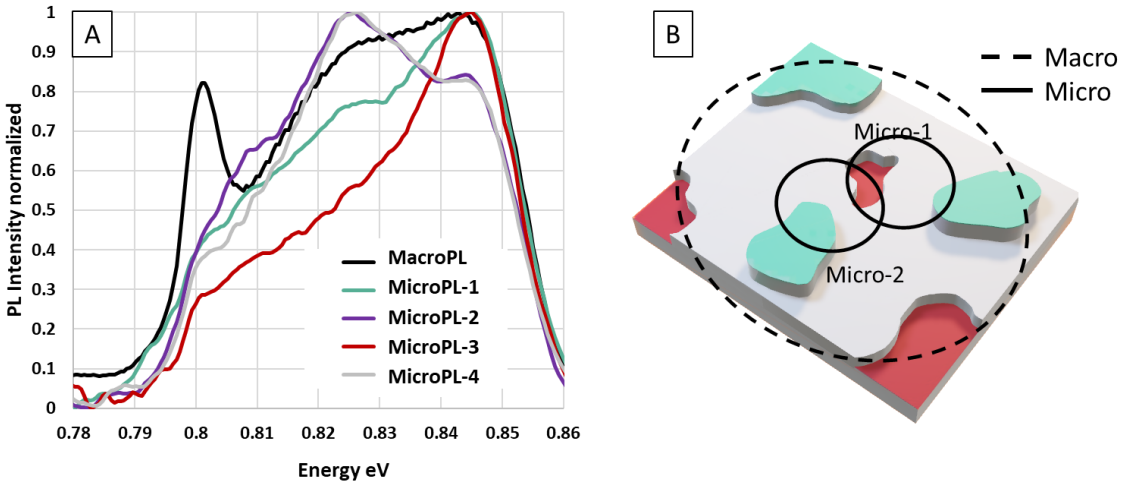

Figure 4.12 (A) PL comparison between the macro-scale and the 4 micro-scale measurement presented in figure 4.11. (B) schematic of the MLs covered by a macro spot size (black dashed circle) and 2 representative micro spots (black circles).

4.4 Impact on device performance

This section moves attention to the RTD device performances and correlates them with the structural imperfection identified by microscopic PL measurements and analysis. As for all the quantum-effect devices, the RTD performance is critically dependent on the crystal purity and heterointerface perfection[48]. For the specific case of the RTD device, it has been demonstrated that ~80% of the parasitic valley current is associated with non-thermal inelastic scattering [41] and as a consequence, the RTD output power is limited by crystal-related imperfections.

Figure 4.13 show the IV characteristics obtained from sample A and sample B respectively from the following mesa areas 1.2-1.4-1.6-1.8-2.0-2.4 and 3 μm^2. Mesa areas are not labelled in the graph so as not to compromise readability. A more detailed analysis between device performance and mesa area will be provided later in figure 4.15. IV results were provided by my collaborator Toshikazu Mukai at Rohm Semiconductors, Japan. Measurements were conducted in the third quadrant to minimize self-heating and prevent catastrophic failure (negative values for both bias and currents). Larger area mesas have been shown to demonstrate catastrophic failure due to the high drive current. In both graphs, we can observe a generally increasing shift of the IV characteristic with increasing mesa area, with both the peak and valley point moving toward higher bias. The same considerations are

true for the peak and valley currents. Curves in red in both graphs highlight the IV for which strong discrepancies in the valley current are observed. Starting from sample A, figure 4.13A shows the results obtained increasing the mesa area from 1.2, 1.4, 1.6, 1.8, 2.0 and 2.4 μm^2. The curve in red indicates the 2.4 μm^2 mesa, for which we observe a valley point (bias and current) out of step with the trend suggested by the other curves. Sample B in figure 2.13B exhibits some fluctuation in the valley current with scaling the mesa area. From the top, the second curve (mesa area of 2.4 μm^2) shows differences with respect to the other curves. The same occurs for the second curve from the bottom, obtained for a mesa area of 1.2 μm^2.

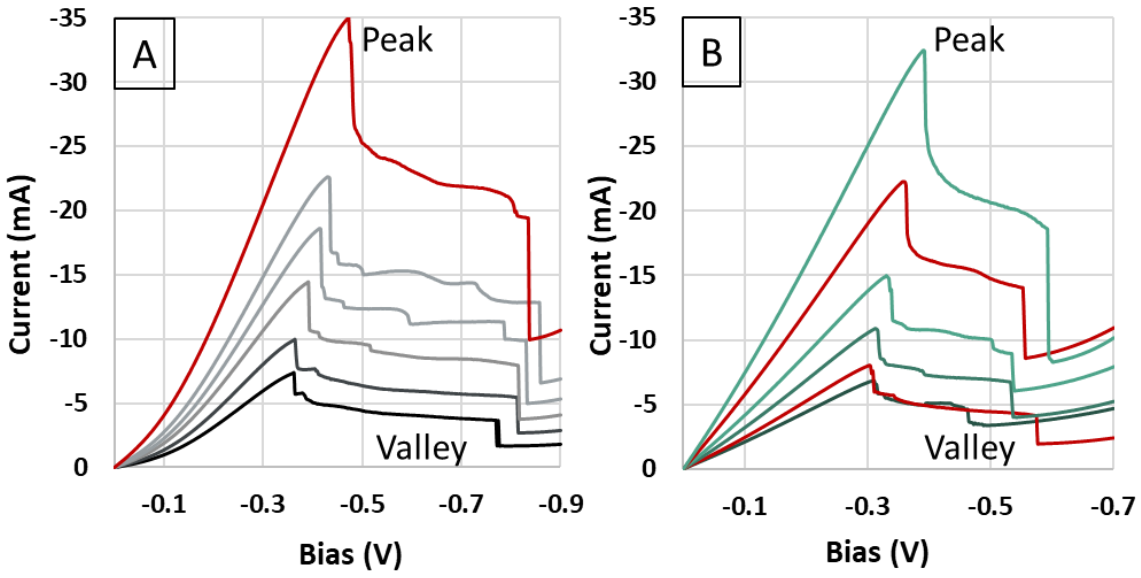

Figure 4.13 IV characteristics with the increasing of the mesa area for sample A (TS 2474-1) and B (TS2484-1) respectively Red curves are highlighting IV characteristics with strong discrepanicies on the valley current. Axes are in reverse order to help the reader as the 3rd quadrant is measured (see text). The mesa area for each curve is not reported in the graph so as not to compromise readability.

Figure 4.14 plots two IV characteristic obtained from sample A(black) and B(green) for a mesa area of 1.2μm^2 to compare the device performance. The peaks and valleys are labelled and marked by coloured dots. Sample A shows the highest current peak and also a higher intrinsic resonator efficiency[39]. This is attributed to the narrower well (12ML) reducing the electron transit time, increasing the peak current. The resonant condition is reached at lower voltage in sample B due to the wider well (16MLs) that moves the first quasi-bound state to lower energy. In sample A the effect of a narrow well is partially compensated with the higher molar fraction(85%) that reduces the e1 energy and increases the e_2 energy level.

Therefore, the peak voltage is similar to sample B. Valley voltage differences are expected to be related to the position of the second quasi-bound state. The e_2 state is at higher energy in sample A due to the QW characteristic described before, consequently, the valley point is reached at higher bias with respect to sample B. Despite the difference in the peak current, the samples show an unexpectedly similar valley current. This undesired current is in part attributed to the self-heating effect generated by the applied current. As this current is higher in sample A we expected sample B to have a much lower valley current with respect to the measured one. We, therefore, suspect that the structural non-uniformities highlighted by PL are also affecting the RTD device performance.

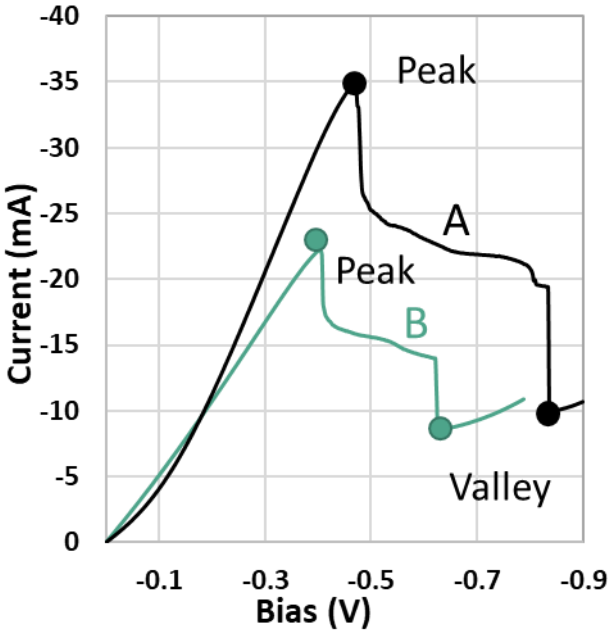

Figure 4.14 Measured I-V characteristics from sample A ((TS 2474-1) black) and sample B ((TS2484-1) green). The graph compares the device performance for equivalent mesa area. Valley and peak points are marked by coloured dots. Axes are in reverse order to help the reader.

To further investigate the non-linear variation in valley current with mesa area, additional sets of devices were tested for each structure. All devices were fabricated in the same fabrication runs to minimize the introduction of errors caused by the fab process. Figure 4.15 plots the peak and the valley current of three device sets from sample A with mesa areas of 1.2, 1.4, 1.6, 1.8, 2.0, and 2.4 μm^2. Larger area devices were shown to exhibit catastrophic failure under test. For sample A, we observe a monotonic increase in both peak and valley current increasing the mesa area. For sample B, while the peak current increases in a monotonic manner, the valley current fluctuates significantly, with only a general increasing

trend being observed in increasing the device area. The variations observed between the three device sets are pose significant reproducibility issues in terms of future manufacturing. Barrier and well heterointerface roughness has been shown to increase the valley current due to electron scattering[42]. In RTDs this was demonstrated by a step-by-step procedure of IV measurement and etching, where structural wafer imperfection impacted the RTD valley current[41].

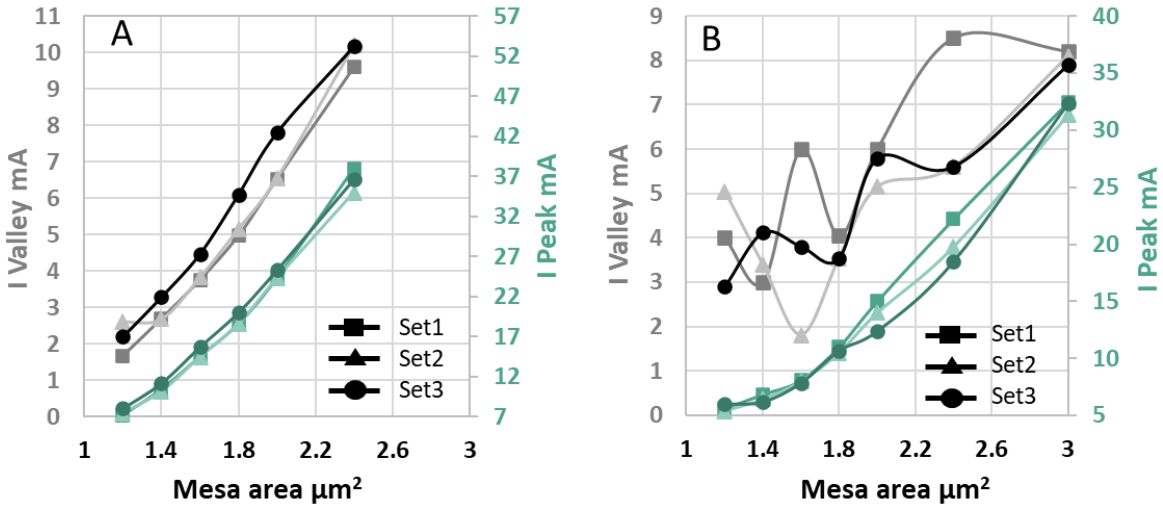

Figure 4.15 Peak (green) and valley (grey) currents varying the RTD mesa area for three different device fabrication runs. (A) Data for sample A (TS 2474-1), (B) data for sample B (TS2484-1),. Datasets indicated by markers (square, triangle, and dot). Lines as a guide for the eye.

The observed fluctuations in valley currents are consistent with the fluctuation observed in the micro PL characterization. Limited variation were observed in sample A and significant fluctuation are observed in sample B. Differences in the RTD characteristic due to island formation growth have been demonstrated in large area devices>100 µm^2 through variations in charge accumulation, observed by combining PL and I-V measurements[135]. In sample B, data showed PL fluctuation from 100 to 10 µm^2 while very strong differences are observed approaching 1 µm^2. Valley currents from mesas with these dimensions are observed to be quite different in three sets of devices similar to a macro-PL scan, large devices are expected to cover multiple ML islands, and the I-V characteristic are obtained from the average properties of the device area. By contrast, the comparatively small devices were fabricated on an area that is of a similar scale to a single ML island (XML,-1ML,+1ML) or parts thereof. Consequently, the local electronic properties may be expected to be different, affecting the valley current and consequently the scaling and reproducibility of the valley current. I, therefore, note that in tackling the challenge of reducing the valley current

in high J-peak RTDs for THz applications, the effect of long range disorder in the epitaxial material must be removed, with micro-PL allowing a route to understanding its effect on valley current. Figure 4.15 shows the theoretical maximum RF power $P_{RF} \approx \frac{3}{16}\Delta I \Delta V = A\Delta J \Delta V$ [40]of the measured RTD devices as a function of the associated mesa area of sample A and sample B, respectively. As plotted in figure 4.14A linear trend characterized sample A meaning that both available current density ΔJ and the voltage swing ΔV of the devices are the same. Moreover, the difference between the three sets of devices is negligible, indicating wafer structural uniformity and high yield. On the other hand, sample B presents a highly non-linear oscillatory behaviour due to the associated instability of the valley current and so ΔJ, which is caused by monolayers fluctuation in the QW and island formation as previously discussed. In addition, the three sets of devices do not present the same trends. This is detrimental in terms of oscillator performance since the major contribution to the RF power of high-current density RTD is provided by ΔJ, whose unpredictability and associated low reproducibility level inevitably lead to a large statistical deviation of output power performance. Based on the results reported here, improvements in output power can be achieved by improving the epitaxial perfection and by increasing the device mesa area. Chapter 5 will discuss possible epitaxial improvements in more detail. With regards to the device area, a trade-off exists between mesa area, output power, and maximum oscillation frequency. Increasing the mesa area, the contact resistance is reduced, improving the current flow. This notwithsatanding, the increase in area increases current in the mesa,and self-heating of the device, with the risk of catastrophic failure [12]. Additionally, the RTD equivalent capacitance increases with the mesa area, reducing the maximum oscillation frequency [136]. This is of critical importance when targeting frequencies near 1THz or above. For frequencies in the range 300-500GHz (0.3-0.5 THz), the area-performance trade-off is more relaxed. In this range of frequencies, large-area devices (> 10 μm^2) can be employed to increase the power, and hence data transmission distance. An example of link budget calculation can be found in [12], with an output power of 2.5mW at 300GHz the link distance can reach up to 1m, which increases to 5m if the power increases to 4mW. Limitations are also imposed by the detectors and the gain offered by the antenna. Among the detectors, RTD-based detectors are under investigation with the goal of a homogeneous technology for the THz trans-receiver. Unfortunately, RTD detectors are based on a different epitaxial design: triple barrier QWs with an intrinsic region to absorb the incident radiation.

Based on these considerations, RTDs for emitters and detectors cannot be manufactured on the same wafer.

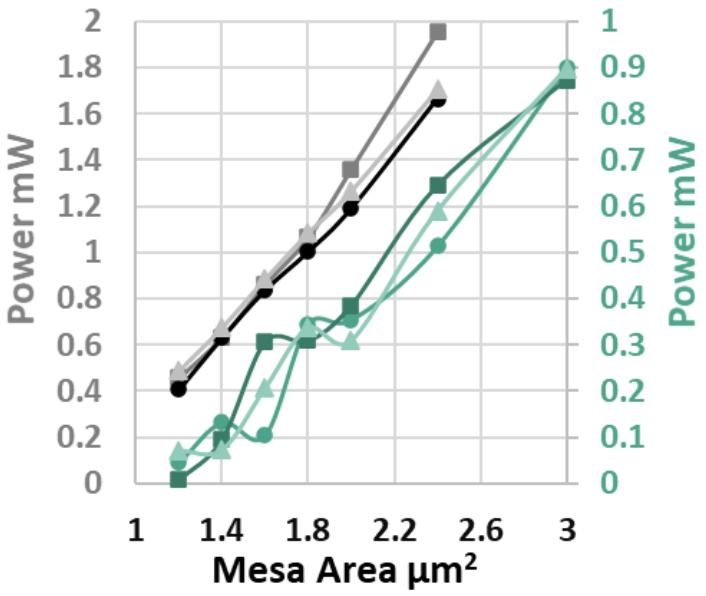

Figure 4.16 Max output power from sample A (gray) (TS2474-1) and sample B (green) (TS2484-1)

In summary, micro-scale PL has highlighted long range disorder in the structures under test, and RTD operating characteristics have been discussed in light of these findings. Despite the experimental critical thickness being calculated to between the M&B and M&P models [124, 125], and hence "safe", I conclude that the strain model limit overestimates the strain budget that can be incorporated in these devices.

4.5 Conclusions

In this chapter I demonstrated the importance of performing PL on a micro-scale to understand micro-scale uniformity of high J_{PEAK} RTD structures, not observable through standard macro-scale PL. The three-dimensional nature of the growth imperfection was analysed, and ML islanding was discussed in terms of strain relaxation. Two structure design

are shown to exhibit different long range disorder length scales through the variation of their PL line shape with reducing excitation/detection area. Through this micro-scale PL mapping, variations have been proven to be equally distributed on a macro-scale but randomly distributed on a micro-scale.

The last part of the chapter showed that devices fabricated from the material studied through PL showed poor valley current scaling and reproducibility, suggesting that the observed material variation is a critical factor in the device performance. Based on these findings I assume that epitaxy-related imperfections may be the real culprit of device failures wrongly attributed to fabrication-related errors in the past. The need for such characterization techniques to cast a light on material uniformity and future devices design and epitaxial process development to minimize the valley current was highlighted.

4.6 Future work

4.6.1 Wafer level mapping

The chapter analysed a small sample and a ~1cm^2 piece of mask was used for the measurement. Section 4.3 demonstrated the mapping capabilities as a proof of concept. For a wafer-level mapping, a custom wafer-size mask can be made to map micro variation on the sample using the smallest pinhole. Due to the required human interaction to align the system on the pinhole, such wafer mapping may be time consuming but still useful for occasional future tests.

4.6.2 Near field PL

Micro-PL was performed using a custom photomask mounted on the top of the sample. This increase the time required for measurement as sample and mask need to be mounted properly. This also limited the range of observation to only the areas covered by the mask. The alignment also constitutes a limitation as the system need to be positioned and focused on the selected hole. To minimize the human interaction system improvements are required to avoid the use of the mask. The development of a fiber optic PL probe similar to a near field optical microscope (NFOM) is considered as one of the possible solutions to provide

sub-micron spatial resolution. This solution will require the probe to fit inside the cryostat and so to be compatible with low temperature operation. Standard micro-PL using a high NA objective lens is also possible, but would require a confocal and spatial filtering approach to ensure high spatial resolution. Resolutions of a few microns diameter should be possible in this manner.

4.6.3 Short range disorder

Micro PL highlighted the lateral extension of long-range disorder while the micro-PL mapping showed their different distribution moving around the sample. This was highlight by their effect on the PL peaks. Short-range disorder is associated with heterointerfaces roughness, and affects the FWHM of the peaks. Fluctuations in this parameter were not observed in the measurements meaning that the length scale of this disorder cannot be determined with this experimental system.

As heterointerface imperfection still remain one of the main causes of electron scattering and peak current reduction, new measurement techniques are required to provide feedback to epitaxy. The main candidate techniques to resolve heterointerface roughness are cathodoluminescence (CL). This technique has already proved to be useful in observing islands [68], further analysis of the CL signal and the FWHM may quantify short-range disorder[93].

Chapter V: Comparison of Epitaxial Methods and Binary InAs/GaAs RTD structures

This chapter compares different epitaxial growth techniques and details alternative QW designs aimed at improving the RTD perfection. The previous chapters have illustrated samples grown by MOVPE and detailed various studies of growth-related effects such as

short and long-range islanding/roughness. Chapter,4 highlighted additional issues introduced by the high strain conditions of the structures.

In this chapter, a selected design grown by MOVPE, MBE and by MBE using a binary InAs/GaAs superlattice instead of the standard InGaAs alloy are discussed. I propose and demonstrate the substitution of the InGaAs QW with a series of InAs and GaAs layers between the AlAs barriers The proposed binary structure is designed to be electronically equivalent to the standard ternary structure but with differences in terms of strain balancing and crystal perfection. The design criteria and strain analysis are detailed using the models reported in chapter 4. XRD and PL analysis of MOVPE (ternary alloy) and a nominally identical MBE sample (ternary alloy) and the electronically equivalent MBE binary alloy sample indicates that ML islanding is reduced in the case of the MBE binary sample. Preliminary device results (courtesy Dr. Quasay) of the MBE binary sample are reported indicating that the device operates as an RTD.

In the first section of this chapter the differences between the MOVPE and the MBE growth processes are described with regard to interface perfection. In the second section the binary InAs/GaAs structure is designed, with the intention that it is electronically identical to a ternary alloy QW structure. Band profile simulation and strain analysis are reported for both types of RTD. The third section discusses structural characterization made by PL and XRD. XRD shows limited information to differentiate the structures, in part due to the small volume of the QW, but is shown for completeness. PL data from the 3 structures is then compared and evidence of improved epitaxial quality is highlighted by the PL line shape. The fourth section summarises the obtained results and discusses the expected benefits of MBE, and the binary superlattice structure in terms of device performance. Preliminary results from devices manufactured from the binary superlattice material are also discussed. Section 5 analyses additional improvements based on advanced growth techniques that can further maximize the heterointerface quality between binary compounds.

5.1 MBE and MOVPE

Both molecular beam epitaxy (MBE) and metalorganic chemical vapour deposition (MOCVD) have been shown to produce good quality RTD epitaxial structures [44, 47].

Differences between the growth methods were discussed in chapter 1 while the growth imperfections were discussed in chapter 2 and 4 with an emphasis on ML islands.

In both reactors the heterointerface abruptness is affected by the surface migration of molecules and the adsorption by the growing surface-layers. In MOVPE the interface abruptness is also affected by the flow rate and is dependent on the concentration of group III reactants in the gas phase flowing through the reactor. When growing the heterointerface, the gas flow must be changed from one component to the next one, this switching must be fast on the time scale of a ML growth in order to avoid the mixing of different elements [93].

This chapter focuses on a second class of growth issues, which are related to the growth of ternary compounds. In chapter 4 I discussed the example of the AlGaAs/GaAs heterointerface, and the imperfections introduced by the aluminium source due to surfaces segregation. For the InGaAs material system, imperfections are caused by alloy disorder such as indium clustering and segregation. Indium atoms are not equally distributed in the growth layer as they tend to segregate at the interface. Segregation causes enrichment of one of the constituent atoms[137] and consequently creates poor heterointerfaces as it modifies the indium-profile of the thin heterostructure. Alloy compositional variations at the heterointerface have previously been investigated by luminescence techniques, looking at the linewidth of the PL spectra[93, 94, 138]. In InGaAs bulk materials, the indium composition is close to the 50/50 ratio (0.532), and the spectral linewidth is attributed to statistical fluctuations of alloy composition on an atomic scale (alloy disorder)[138]. In strained structures (In≠0.532), the compositional fluctuation is on a larger scale, referred to as clustering[139]. Scanning tunnelling microscopy (STM) images revealed InAs clusters containing several indium atoms, affecting the heterointerface with a physical broadening of 2-4 layers [107]. In our structure, the same phenomena were observed by high-resolution TEM scans as shown in figure 5.1. The first figure highlights the wavy heterointerface at the second barrier, indicated by white arrows. Figure 5.1B shows the same picture enlarged and contrast-enhanced to highlight the indium segregation around the second barrier. Red dashes are equally separated, and they are highlighting the inhomogeneous composition (white areas) around the second barrier with respect to the first one.

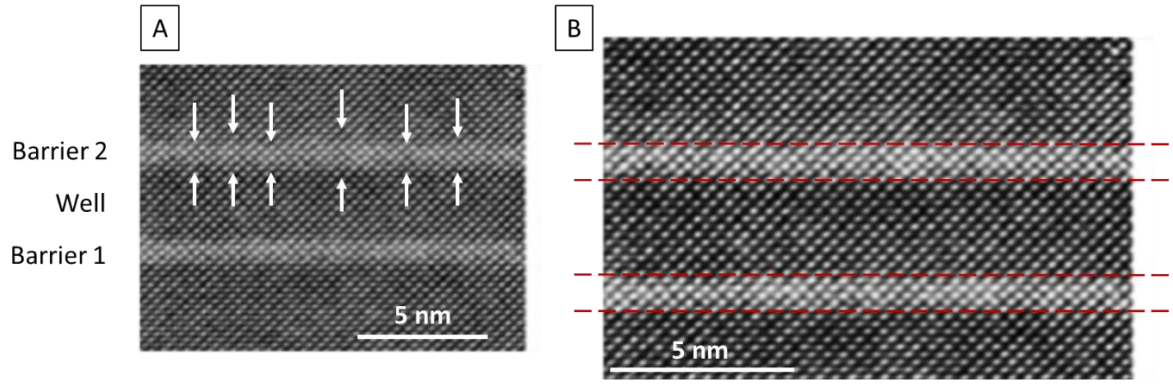

Figure 5.1 High-resolution TEM picture of an RTD QW (sample TS1902). White arrows in picture A are highlighting the thickness fluctuations before and after the second barrier. Picture B shows the same scan enlarged, red dashed lines are the highlighting differences in barrier thickness and indium concentration.

5.1.1 Binary RTD structure

Based on the above considerations it is evident that the use of ternary compounds offers several advantages, but they come with the introduction of issues not observed in binary compounds[138]. In InGaAs, indium clustering is observed since indium atoms are bonded to arsenic atoms, the clustering is in fact composed by chains of InAs within a QW composed of InGaAs[107]. A representation of the phenomena is depicted in figure 5.2. From the left, As, Ga and In atoms are represented by the coloured spheres and labelled. In the centre I represented the InGaAs bonding and the InAs chain. The last picture on the right side is a schematic of the InGaAs crystal, on the top the InAs chains are highlighted by the red arrows. The selective growth of binary semiconductors creates more predictable crystal pattern vs lattices where it is not possible to predict the state of a substitutional group III atoms (Al, Ga, In).

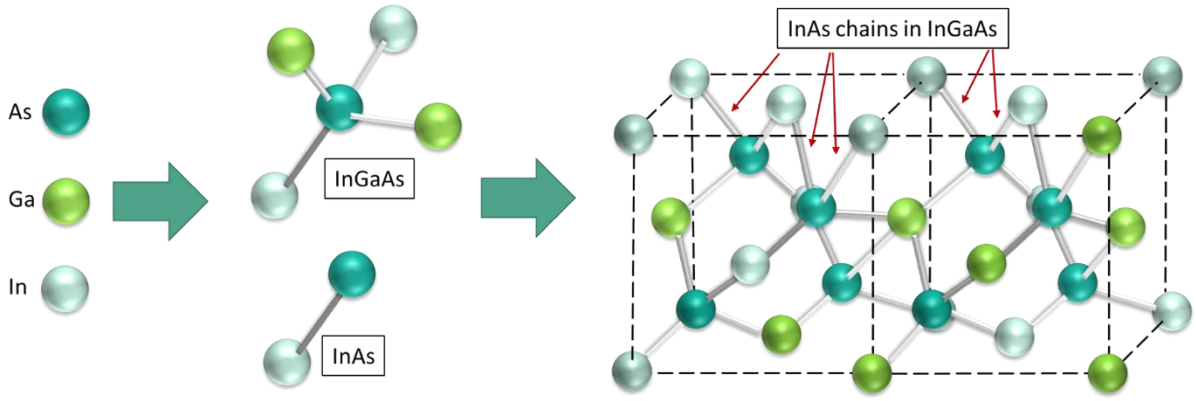

Figure 5.2 representation of As, Ga, and In atoms (left). Crystal base for the InGaAs and InAs (centre). InGaAs crystal structure (right). arrows are highlighting the InAs chain and the inhomogeneous In distribution in the structure.

Figure 5.3 shows an example of the structure design where the basic cell is composed by 3ML of InAs and 2ML of GaAs. The periodic structure is composed by 3 superlattice repeats for a total of 15ML of well thickness between the AlAs barriers. The equivalent molar fraction is obtained by interpolation to be In=60%.

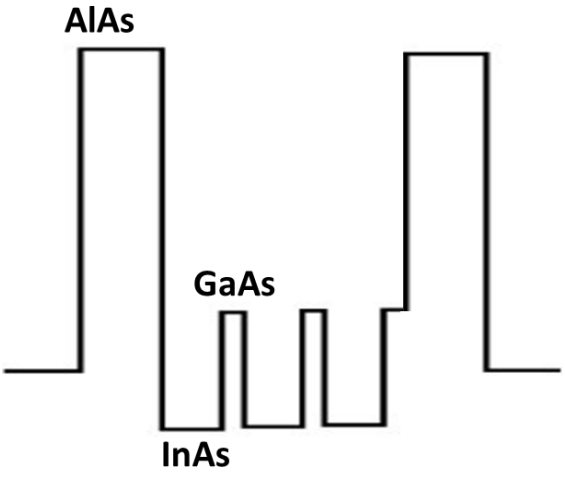

Name	Material	Thickness [ML]
Barrier	AlAs	4
Well	GaAs	2
	InAs	3
	GaAs	2
	InAs	3
	GaAs	2
	InAs	3
Barrier	AlAs	4

Figure 5.3 Example of Binary RTD QW, conduction band profile (left) and QW epilayers (right).

The desired target designs are structures with 15MLs of well thickness and [In]=80%, or 12MLs and 85%. These designs were already investigated in the past[41] and in previous chapters of this thesis, and they exhibited a negative differential resistance (NDR) region in their IV characteristic. The next section will describe the binary structure design.

5.2 Structure Design

In the previous section an example of the binary structure was presented. With respect to the ternary compound design, the equivalent molar fraction cannot be arbitrary controlled, but it is given by the number of InAs and GaAs MLs in the well. This limits the equivalent indium mole fraction that can be obtained using this type of design. The starting parameter is the well thickness, which dictates the possible indium concentration that can be obtained.

The following table shows the combination of InAs and GaAs MLs and their respective effective indium molar concentration. For the 15ML design column, a perfect match of In=80% is obtained by the combination 12MLs InAs and 3MLs GaAs, assisting me in my goal of designing a binary structure that can be compared with the growth of the ternary ones by MOVPE and MBE. The table reports several fractional values for the indium concentration which are difficult to obtain with the required accuracy. For these reasons the desired design is the one marked by the red rectangle.

15 ML design			12ML design		
InAs MLs	GaAs MLs	Equivalent [In]	InAs MLs	GaAs MLs	Equivalent [In]
15	0	1	12	0	1
14	1	0.933	11	1	0.916
13	2	0.866	10	2	0.833
12	**3**	**0.8**	9	3	0.75
11	4	0.733	8	4	0.666
10	5	0.666	7	5	0.583
9	6	0.6	6	6	0.5

Table 1 Equivalent indium mole fraction varying the number of InAs/GaAs layers. Result obtained for a well thickness of 15MLs and for 12MLs. Red rectangle

5.2.1Strain Analysis

The previous table highlighted the combination of MLs to obtain the molar fraction of 80%. Determining how to arrange the 12ML of InAs and the 3MLs of GaAs adds to the complexity of the design. The design criteria must take into account the QW symmetry and the QW strain.

The first proposed structure has the 12 InAs MLs split in two and separated by the 3 GaAs MLs. Based on the critical thickness model[123], and considering the InP as a substrate, the Tc for the InAs is ~4ML while the Tc for the GaAs is 4MLs. The proposed structure has two sections of 6MLs of InAs, 2ML higher respect the limit. We previously demonstrated how the AlAs can be used to partially compensate the strain in the QW but also that the strain modelling overestimated the amount of stress that can be incorporated by the device[73].

For the second proposed structure 3 GaAs MLs need to be distributed in the well, but this odd number puts additional limitations on the possible designs. Splitting the GaAs in 2 and 1 MLs will create asymmetry in the QW. Splitting the 3MLs in two parts will require the growth of fractional MLs (1.5ML). Chapter 4 described the challenges in growing fractional MLs numbers resulting in a high probability of creating ML islands and wavy heterointerfaces. The new proposed design has a periodic structure realized by 3 InAs MLs and 1 GaAs ML. To clarify the differences between the two proposed designs, figure 5.4 shows the conduction band profiles of the 6/3/6 design (left) and the superlattice 3/1 design (right).

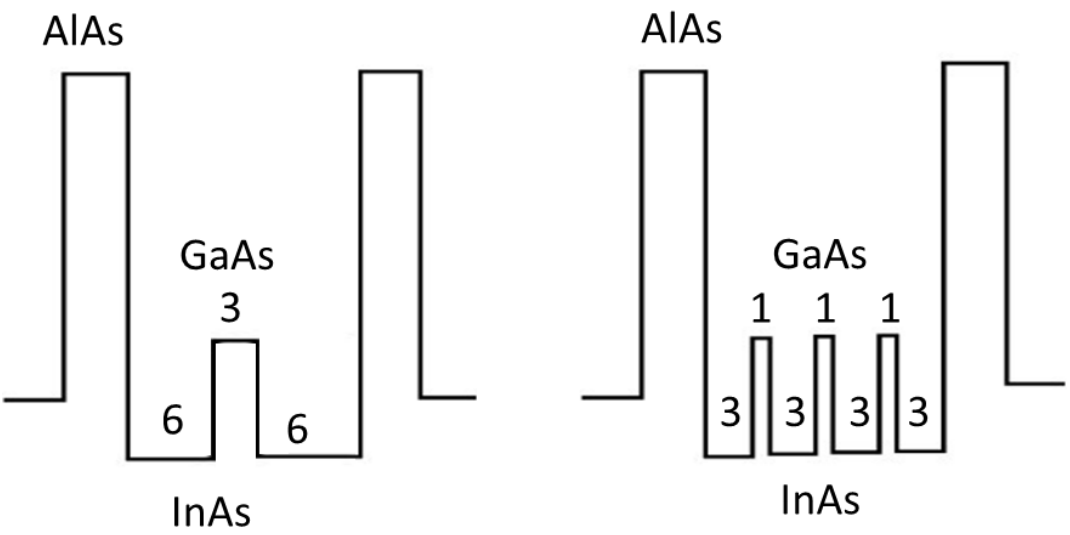

Figure 5.4 the conduction band profiles of the 6/3/6 design (left) and the superlattice 3/1 (right).

To simulate the strain and stress in the structure I used the average in-plane stress method reported in chapter 4, the formula is reported here to help the reader [81]:

$$X = \frac{2}{t_1+t_2}\left(t_1 A_1 \varepsilon_1 + t_2 A_2 \varepsilon_2 \frac{a_1}{a_2}\right) \quad \text{(eq 5.1)}$$

The above formula is referred to a two material system: material 1 on the substrate (or lattice match bulk), and material 2 growth on material 1 (M2/M1). The strain of the materials is dependent on the material combination, represented by the strain component **ε**, and the factor $\frac{a_1}{a_2}$. The $\boldsymbol{\varepsilon_1}$ strain coefficient takes into account the mismatch between material 1 and the substrate, while $\boldsymbol{\varepsilon_2}$ is calculated considering the substrate and material 1. For the current analysis, the formula is extended including the additional material combination and their respective coefficients **ε** and $\frac{a_1}{a_2}$: InAs/AlAs, GaAs/InAs, InAs/GaAs and AlAs/InAs terms.

The results for the two proposed binary design are reported in figure 5.5 and compared with the ternary design. The graph plots the product of in-plane stress and layer thickness (in MLs), this schematic representation makes it easy to plot and visualize each thickness-weighted strain contribution and the strain limits using straight lines and segments. The goal is to verify if the strain in the proposed structure does not exceed the limits imposed by the M&B model.

The AlAs and GaAs strain limits on InP is ~4 MLs, corresponding to a tensile strain stress of ~0.305 N/ Å (0.0755 N/Å²). therefore, this value is assumed as the "tensile stress limit" and it is indicated by the black dashed line. The compressive limit is calculated based on the InAs critical thickness (5ML) and that of $In_{0.8}Ga_{0.2}As$ (~12ML), corresponding to a strain stress of 0.2 N/ Å (0.05 N/Å²). This limit is indicated in the graph by a black wide dashed line.

The strain limits are not symmetrical respect to the origin of the axis, this is due to the stiffness and strain coefficient of the InAs, which are lower respect the GaAs and the AlAs. From 0 to 4ML the stress is equal for all the three structure, and it is caused by the first AlAs

barrier (4MLs). Starting from the ternary design (green curve and square markers), 15MLs of In=80% InGaAs have compensated all the barrier tensile strain, leaving a residual compressive stress within the compressive limit.

The binary 6/3/6 structure strain curve is entirely in the tensile part of the graph, the tensile limit is exceeded at 13 ML due to the 3 GaAs MLs (10 to 13 MLs) on the 6MLs of InAs. At the end of the QW the barrier strain shifts the overall strain close to the limit, but it will reduce again by the InGaAs contact cap.

Similar considerations apply for the binary superlattice, but in this case the periodic 3/1 structure gradually reduces the barrier tensile strain without reaching the strain limit. Both binary structures are equivalent at the end of the QW.

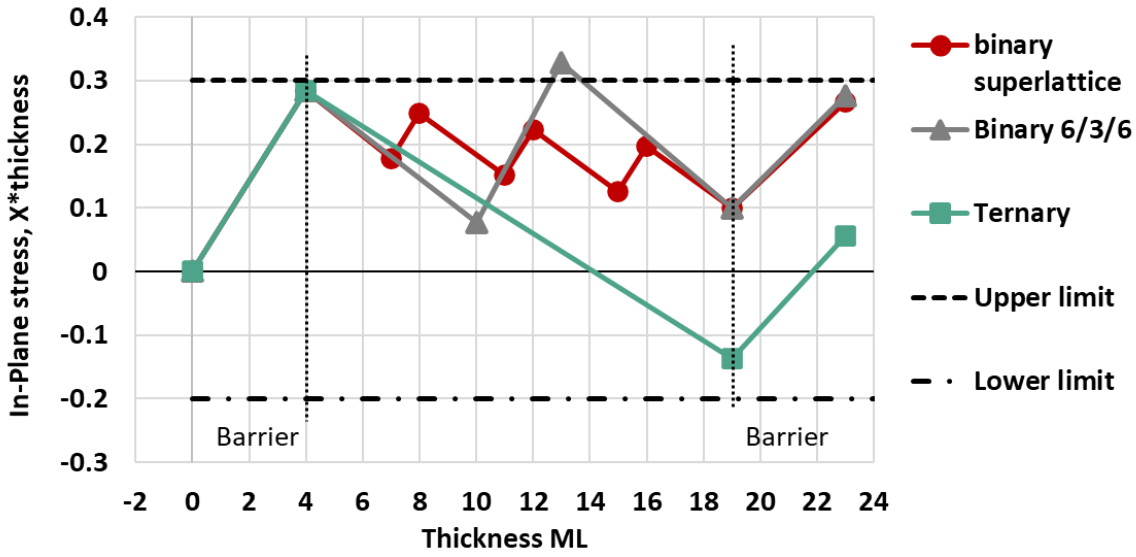

Figure 5.5 Strain stress evolution increasing the well thickness(in MLs). Ternary structure (green, square markers), binary 6/3/6 (grey triangles), and binary superlattice (red, dots). Vertical dashed lines are marking the barrier positions. Predicted stress limits are indicated by horizontal dashed lines.

Exceeding the critical thickness during the growth sequence puts the entire structure at risk due to an increase in defect formation and relaxation due to the high temperature[73, 81]. For this reason, the 6/3/6 structure is discarded at this stage. The superlattice structure has a strain evolution within these limits, and at the end of the well (19MLs) the strain is also closer to the strain balance condition with respect to the ternary structure. The strain introduced by the second barrier may create concern, but it will be compensated by the contact cap. If these limits are respected, ideal balancing of the overall QW strain is neither

desirable nor necessary [140], the critical part is mainly influenced by the first barrier plus the well sequence [81, 140].
The next section describes the simulation on the band profile and the expected electrical properties.

5.2.2 Band profile simulation

Table2 shows the simulation results obtained from the 2 structures under test. The simulations were computed in next nano, and a description of the simulation suite was presented in chapter 2. The table reports the simulated e1 and e2 quasi bound states energy and the $\Delta\mathbf{E}$ between them. The e_1 energy is approximately the same, with just a 1meV of difference between the binary and the ternary designs. The main difference involves the position of the e_2 level and consequently the difference between e_2 and e_1, $\Delta\mathbf{E}$**.** The highest $\Delta\mathbf{E}$ is obtained from the binary superlattice structure, 0.01eV higher than the ternary. A higher ΔE is a desirable parameter to increase $\Delta\mathbf{V}$ in the IV device characteristic [45].

Parameter	e_1 [eV]	e_2 [eV]	ΔE [eV] (e_2-e_1)
Ternary	~0.035	~0.736	~0.7
Binary superlattice	~0.034	~0.745	~0.71

Table 2 Simulation results for the 3 structures under test. The periodic binary structure presents the best ΔE.

5.3 Epitaxy Characterization

5.3.1 XRD characterization

The XRD characterization is reported in the next series of figures. From the top, figure 5.6A shows the experimental data obtained for the MOVPE structure while figure 5.6B shows the

results obtained from the ternary MBE structure. The total scan time was ~9hr, 0.0002arcsec, step size for 2s. The sharp central peak at 31.760 is the substrate peak, a second peak on the left side of the curve is observable in both traces, associated with the bulk InGaAs material. In the MOVPE structure, the second peak is at 31.728, which indicates a slightly higher molar fraction of 0.541, with a mismatch of 1.8% with respect to the substrate. In the MBE trace (figure 5.6B) the mismatch is higher, the bulk peak is at 31.680 which indicates a molar fraction of 0.549 with a mismatch of 3.1 %.

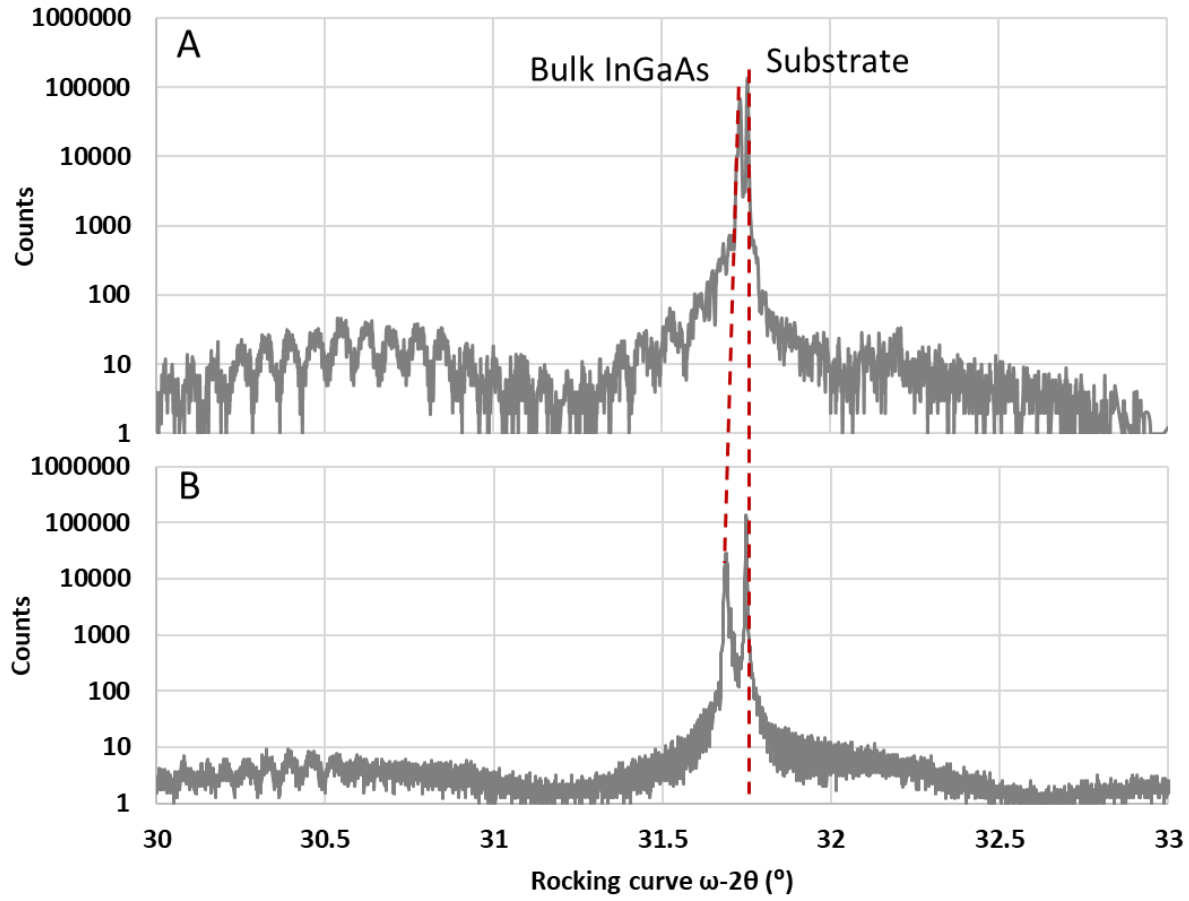

Figure 5.6 XRD rocking curve from the MOVPE ternary structure (A, sample TS2470-1) and the MBE ternary (B, TS1580-T). Substrate and LM InGaAs diffraction peaks highlighted by red dashed lines.

These MOVPE and MBE structures have the same active region design but there are slight differences in other part of the structure. For this reason the two structures present slightly different XRD curves. The MOVPE structure presents a better S/N ratio thanks to the additional undoped copy QW [74] buried on the bottom of the structure. This additional period of the QW improves the intensity of the XRD signal. With respect to the MOVPE

structure, the MBE has a thicker contact cap and does not have the buried QW. The XRD data fitting[84] indicates that the structure parameters are inside the growth tolerance. As discussed previously, more precision to the structural data will be provided by the PL characterization.

Figure 5.7 shows the data obtained from the binary MBE structure. The graph shows a generally poor S/N ratio. The sharp central peak is associated with the substrate, and no bulk peak can be distinguished in this graph. The inset shows a focus in the range 31.5-32, the secondary bulk peak is at 31.78, which indicates a mismatch < 1%, improved thanks to the feedback obtained from the ternary MBE structure. With respect to the XRD scans reported in figure 5.6, the count number for the bulk peak intensity is several orders of magnitude lower. This is due to a reduced scan time (measurement time was reduced by half with respect to the previous samples), which limits the number of counts per second measured by the detectors. An increase in exposure increases the number of counts with the sacrifice of fringe resolution. This is especially true in measuring the QW characteristics. The active region in this structure is composed of a few MLs of GaAs and InAs, such a small amount of material produces poor diffraction and consequently poor signal intensity. Future improvements in this direction are discussed in section 5.5 at the end of the chapter.

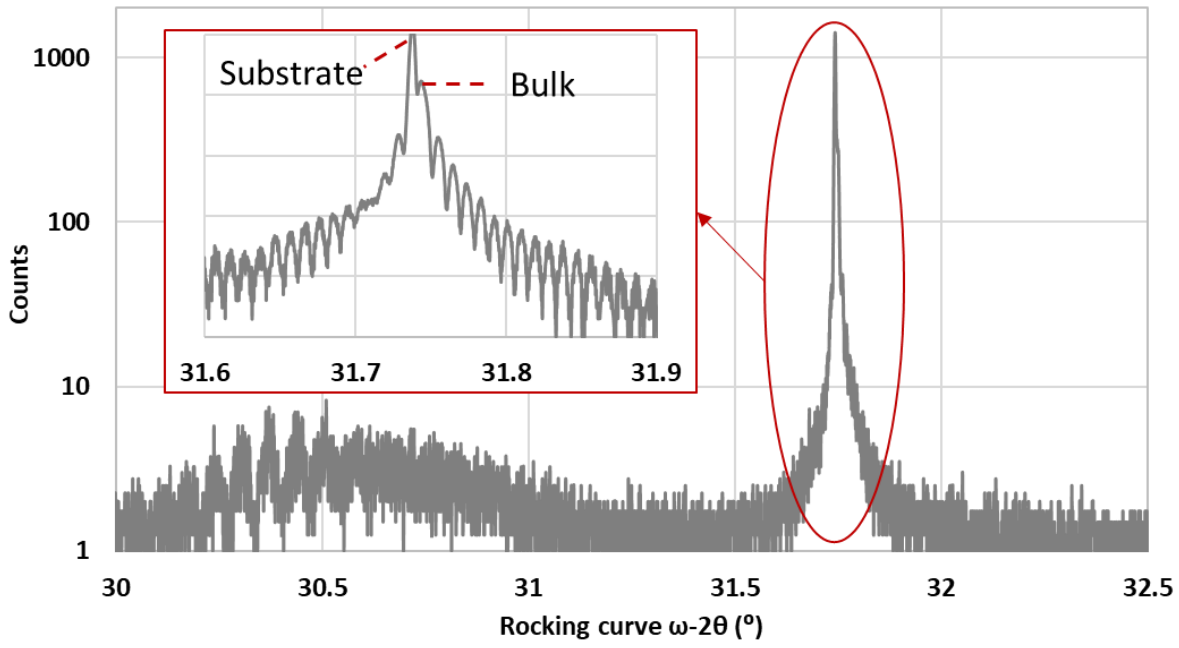

Figure 5.7 XRD rocking curves from the binary MBE structure. The inset shows a focus around the substrate diffraction peak. Sample TS1580-SL

5.3.2 PL characterization

Figure 5.8 shows the PL spectra measured from the 3 structures under test. The MOVPE structure (green) shows a sharp InGaAs bulk peak at 0.8eV and two other peak are observable at 0.815eV and 0.84eV. Starting from lower energy, the ternary MBE structure (grey) shows a broad spectra, the InGaAs bulk peak is observable at 0.8eV but with a wider shape in respect to the previous case. As highlighted by the XRD characterization, the observed blue shift is attributed to the slightly higher In mole fraction in the bulk InGaAs. The broad feature may be caused by the contribution of multiple effects, such as the convolution with the Type-II transition expected between 0.77 and 0.79 eV and the +1ML Type-I peak. Moving to higher energy, the peak at 0.815eV associated to the XML Type-I transition is in line with my expectation. The first important result is the absence of any feature above 0.84eV, a region where the -1ML Type-I transition was expected. The binary structure (red) does not show any clear feature related to the bulk peak and the intensity in the 0.76-0.8eV is weaker with respect to the ternary MBE structure. The peak at 0.815eV is associated with the XML Type-I peak. No other features are observable at high energy. The peak at 0.815eV, common in all the spectra, confirms that the designs are electronically equivalent, with very similar electronic properties.

With regard to the epitaxial quality, the results suggest that changes are required in the bulk InGaAs growth for the MBE structure, as highlighted by the XRD scan. The QW epitaxial quality have shown interesting results. The ternary MBE structure shows partial suppression of the ML fluctuation, especially for the -1ML valleys as compared to the MOVPE sample. The binary structure shows a better suppression of the overall ML fluctuation by comparison to both ternary samples (MOVPE and MBE).

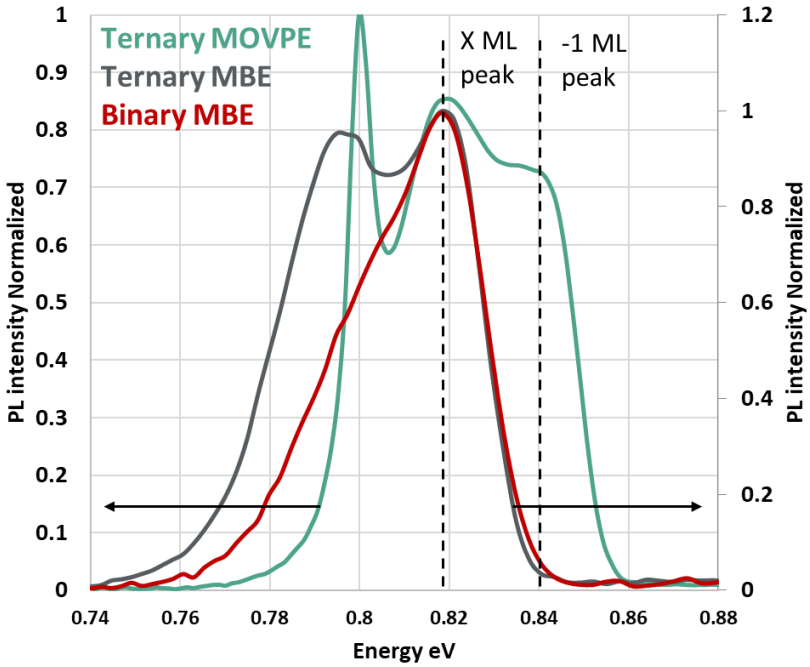

Figure 5.8 PL characterization of the MOVPE ternary structure (green, TS2470-1) compared with the ternary MBE(grey, TS1580-T) and Binary (red, TS1580-SL) structure.

5.3.3 Electrical Characterization: early results

This section briefly details the IV characteristics obtained from the binary MBE structure. The fabrication process was conducted at the University of Glasgow by Dr. Quasay, thanks to collaboration with Prof. Edward Wasige's group. Details about the fabrication are reported elsewhere[141].

Figure 5.9 shows the IV characteristics obtained from the superlattice design from a mesa diameter of 500nm. The peak is reached at 0.78V with a peak current of ~0.001A.

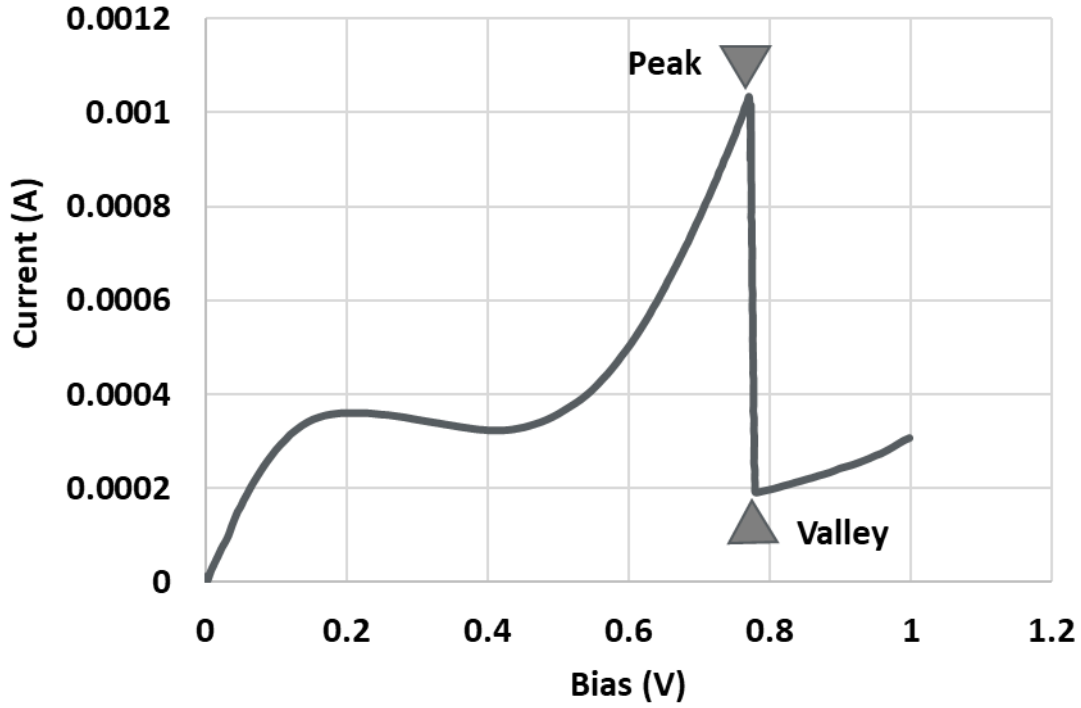

Figure 5.9 Binary superlattice IV characteristic, peak and valley points marked by triangles. Sample TS1580-SL

The proposed binary structure has been shown to exhibit an NDR region. Despite the result obtained from the PL characterization, the device performance is poorer than other devices reported in the literature. As discussed in chapter 2, the FWHM is correlated to the QW heterointerfaces perfection (well-barriers). The PL characterization highlighted a discrete suppression of the ML fluctuation but no evidence of a reduction or increase in the peak FWHM were observed. The entire NDR is at lower bias (V_{valley} < 1V), a condition desirable for low power consumption. The device exhibits a peak current of 0.001 A from a mesa area of 2 μm^2, this value is an order of magnitude lower with respect to the other device reported in chapter 4 with similar QW properties (~0.025 A). This poor result is attributed to issues related to the InGaAs contact cap and the metallization. The reported design has an InGaAs contact cap of 16nm, higher than the maximum limit imposed by the critical thickness for an indium mole fraction of 80%. This thickness was chosen to improve the XRD intensity and the S/N. The XRD scan reported in the previous picture does not show issues with this layer. Strong surface imperfections are observed by SEM imaging. Figure 5.10 shows an SEM picture focused on the sample surface and a contact pin after metallization. The roughness on the sample surface is attributed to strain relaxation on the shallow layers of the InGaAs contact cap. This did not leave appreciable traces in the XRD pattern but

compromised the device fabrication processes. This is particularly true for the metal deposition process; the roughness creates issues with the adhesion layer between the sample and the titanium (adhesion material before the gold deposition). Future designs will return to an InGaAs contact cap of 8nm.

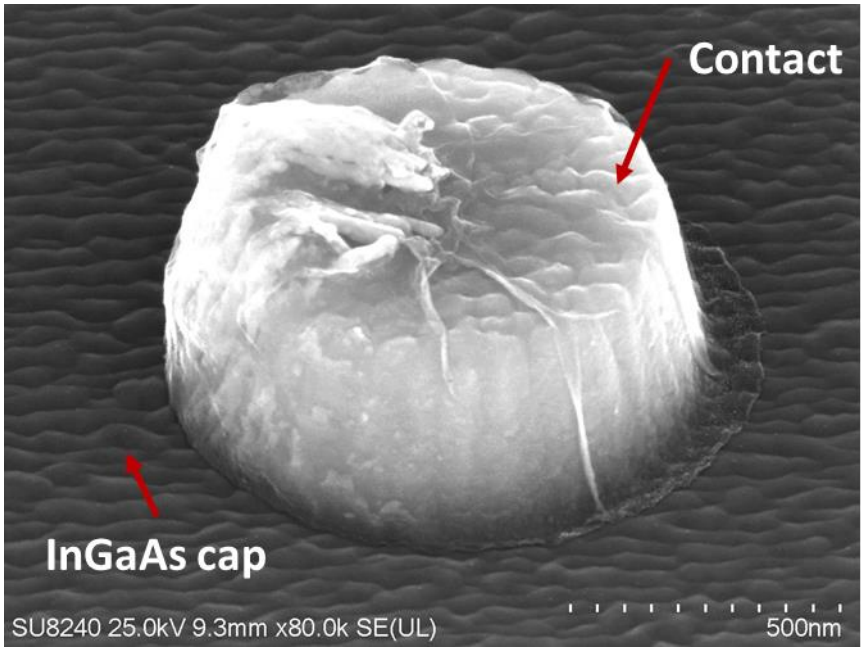

Figure 5.10 SEM picture focused on the InGaAs cap surface and a contact pin after metalization. The wave patterned surface is attributed to strain relaxation.

5.4 Conclusions

In this chapter I presented the different performance between MOVPE and MBE reactors for the growth of RTD structure with regard to non-destructive characterisation of the wafer and a I presented a different approach for the design and growth of high J_{PEAK} RTD active regions.

The binary design approach aims to reduce the epitaxial imperfection caused by ternary compounds but suffers from an increase in heterointerface number and loss of the arbitrary control of the molar fraction. The design criteria were presented using the well thickness as a starting parameter, consequently the equivalent molar fraction determines the number of

InAs and GaAs MLs if direct comparison to other structures is required. Different equivalent designs may be obtained organizing the GaAs and InAs MLs differently.

Strain equations were computed to test the structure stability. Results indicate that the stability depends on how the layers are disposed within the QW. Differences were also observed in the electronic characteristics by band profile simulation.

Characterization by XRD provides limited information. As XRD gives an S/N ratio and a signal intensity (number of counts) proportional to the thickness of the material under test, dealing with a QW composed of few MLs can only provide very noisy data. PL highlighted a partial suppression of the ML fluctuation in the ternary MBE structure with respect to the PL spectra measured from the equivalent ternary MOVPE structure. A strong suppression of the ML fluctuation was observed in the binary MBE design.
The binary design has proved to exhibit NDR in its IV characteristic, but the expected improvements in device performance were not observed at this early stage. Possible improvements will be discussed in the next section.

5.5 Future work

5.5.1 In depth characterization

The binary structure characterization was presented in section 5.3 and highlighted the need for an improved characterization scheme. X-ray rocking curves presented poor signal to noise ratio due to the small volume of the QW. A high-resolution X-Ray system can provide the required S/N ratio to analyse this even more challenge structure and keep the characterization as non-destructive.
PL has provided useful information about the ML fluctuation but improvements in the

heterointerface quality remains unclear. As planned in other section of this thesis, cathodoluminescence is the techniques of choice for improvements in spatial resolution.

As presented in chapter 3, PLE can provide e_2-releted transition from which the e_2 position can be deduced. The simulation of the band profile has highlighted differences in the position of the second quasi bound state between the ternary and the binary design. To confirm this difference PLE will be fundamental.

Considered the challenge in characterizing a QW composed by layers of just 1 atomic sheet of GaAs, HR-TEM imaging is still the best candidate to evaluate the epitaxial perfection.

5.5.2 Maximizing design efficiency

The 15ML In=80% was selected as a test as it was the only one with a perfect match with the ternary In=80% structure. As the binary design has proved to exhibit a NDR in its IV characteristic, new structures can be designed with less challenging growth condition (layer with thickness >1ML), or utilising closer strain balancing. The 6/3/6 design was discarded for this first test due to the strain limits. A decrease in the number of heterointerfaces is the first possible improvement for this structure.

5.5.3 Novel growth techniques

Migration enhanced epitaxy (MEE) is an MBE growth technique which has proved to grow structure with flat heterointerfaces for the GaAs/AlGaAs material system [120]. This technique improves the heterointerface quality increasing the migration of Ga and Al atoms. The improvement is obtained creating an As-free atmosphere during the Ga or Al supply in the reactor. The effect on the InGaAs compound were not studied at the time of writing, but MEE may highly improve the binary RTD epitaxy acting on the AlAs barriers, and GaAs and InAs well layers.

Chapter VI: Summary and Outlook

6.1 Thesis Summary

Chapter 2 investigated the origin of the multiple peaks that makes the PL spectra from RTD structures broad, complex, and difficult to analyse. The chapter proposed and demonstrated a method to deconvolute the PL spectra in a sum of multiple features originated by the LM-InGaAs layers, the doping, and the multiple QW radiative emission generated by the mono-layer fluctuation during the grow process [75]

Chapter 3 used the result from chapter 2 to investigate the use of PLE to characterize RTD structures and determine critical information about the conduction band offset in the highly strained QWs of the RTD [49]. As a result, a complete non-destructive characterization scheme is executed based on simulation, XRD, PL and PLE. Future design optimization relies on the ability to accurately discriminate which combination of design parameters and growth optimisation can improve the device performance[71].

Chapter 4 explored micro-PL to characterize RTD structures with a PL spot size comparable to the device mesa. RTD mesa area is moving from the micron scale to the sub-micron scale to minimized parasitic effects which are proportional to the device mesa area. ML islands are qualitatively observed by micro-PL and their spatial extent, and effect on the device performance was assessed [73].

In Chapter 5 a comparison of MOVPE and MBE growth processes indicated enhanced perfection in MBE. In the attempt to minimizing the imperfections introduced during the grow process and the material system in use, a superlattice (SL) RTD made by layers of InAs and GaAs was proposed and demonstrated. The aim being to drive down the (non-thermally activated) valley current. Characterisation techniques suggest an enhanced level of perfection, as compared to the ternary alloy equivalent. Devices fabricated from this novel material exhibited an NDR region, and early results have demonstrated interesting performance with room for improvement [Paper in preparation].

6.2 Outlook

Each of the previous chapter detail possible ways to improve the epitaxy characterization or RTD device engineering. This section adds more detail maintaining attention on the 3 key topics of this thesis: epitaxial processes, structure design and epitaxy characterization.

6.2.1 New epitaxial processes

Superlattice structures can contribute to enhancing the RTD state of the art and section 5.3.3 introduced MEE as a variant of the MBE growth technique to fabricate high quality crystals. As commercialization is the ultimate goal, we need a fabrication process more market-friendly with characteristic like high-volume cost-effective manufacture and MOVPE is the preferred growth method to this end. Flow modulation epitaxy is the MEE equivalent for the MOVPE.

6.2.2 New epitaxial structures

Chapter 1 highlighted how the conduction band offset plays an important role in defining which material system is the best for RTD devices. Chpater3 demonstrated how this parameter can be determined experimentally, with values different from those predicted by simulation. Understand the band-offset variations in highly-strained QWs will help future design optimization in avoiding design/procedures which reduce the band-offset in favour on the ones which can enhance design performance.

Previous considerations were made for ternary InGaAs structures but they are also valid for the superlattice design. Superlattice structure were designed with InAs layers after the AlAs barrier, which should correspond to higher band offset with respect to the ternary InGaAs. The equivalent conduction band offset value for the superlattice well made by InAs/GaAs layers was not determined experimentally. Simulation parameters for this type of structure are obtained by interpolation only. Further research is needed to explore the possibility to tune the conduction band offset by changing the layer combination or position.

Strain calculations in chapter 5 highlighted the QW strain evolution during the growth process. Calculations were based on the work reported in[81]. The AlAs barrier has a strong

impact on the QW strain budget, and future structures can be designed reducing the barrier thickness to 3 or 2 ML in an attempt to reach a perfect strain balance condition or to growth challenging, highly strained structures. Barrier thickness reduction has the additional benefit of increasing the peak current by reducing the electron transit time. Additionally, chapter 4 highlighted how the strain limits obtained from the mathematical models may overestimate the real strain limits, resulting in an increase of growth imperfection (e.g., ML islands). One of the reasons may be attributed to thermal effects. If high temperatures are involved during the growth process and if the thermal expansion coefficient of the material involved differ significantly**,** changes in the lattice parameter may occur, resulting in unexpected relaxation[81]. Therefore, simulation can be improved to include information from the growth process in use.

6.2.3 New Characterisation Processes

This thesis explored RTD epitaxial imperfection, their understanding through wafer level non-destructive characterisation, and their effect on device performance. The characterization process may not result in an unambiguous solution, i.e., PL may give multiple answers making manufacturing optimization impossible. PLE comes into play to improve spectroscopic characterization by providing additional transition energy values that limit possible solutions. Chapter 3 proposed the need for a PLE mapper to perform wafer-scale characterization. A PLE system can be used to perform standard PL but the contrary is not true. A PLE mapping tool can be used to improve our understanding of whether the electronic properties are varying across the wafer surface, as was done previously for the doping concentration [64]

Additionally, chapter 4 highlighted the need to move to micron scale characterization as the RTD scaling is already introducing more challenges in addition to the one detail in this thesis. As mentioned before, high J_{PEAK} design structures are becoming more challenging as QWs are becoming smaller and the indium concentration is higher than 85%. The barrier thickness has moved from 1.4-1.2 nm (approx. 4-5MLs) to 1nm (approx. 3ML), these dimensions are challenging to fabricate with precision as process optimization/calibration is more difficult, with possible errors/fluctuation that will certainly complicate characterization and impact the device performance. Chapter 3 highlighted how XRD can help in characterizing the barrier thickness, but an HR-XRD apparatus is required to obtain useful

S/N from the data. Investigating the effect of a barrier reduction on the PL will be critical to simplify the analysis. Figure 6.1 show the simulated Type-I transition for a generic RTD structure (AlAs/$In_{0.8}Ga_{0.2}As$) varying the barrier thickness. Above 4ML the transition energy is constant, under 4ML we observe a strong reduction in energy. Approaching a thickness of 1ML the barrier became "transparent" as the effect of the barrier disappears and the QW is more similar to a potential well made of LM-InGaAs/ $In_{0.8}Ga_{0.2}As$. Moving from 4 to 3ML the simulated change in energy is 0.0053eV, comparable to a change of ±1-1.5% in molar fraction. From 3 to 2ML the change is 0.022eV, comparable with a change of ±1ML in well thickness or ±3-4% in molar fraction. Chapter 3 highlighted the need to reduce the number of variables in order to simplify the characterization, a reduction in barrier thickness will re-introduce the barrier thickness into the equation.

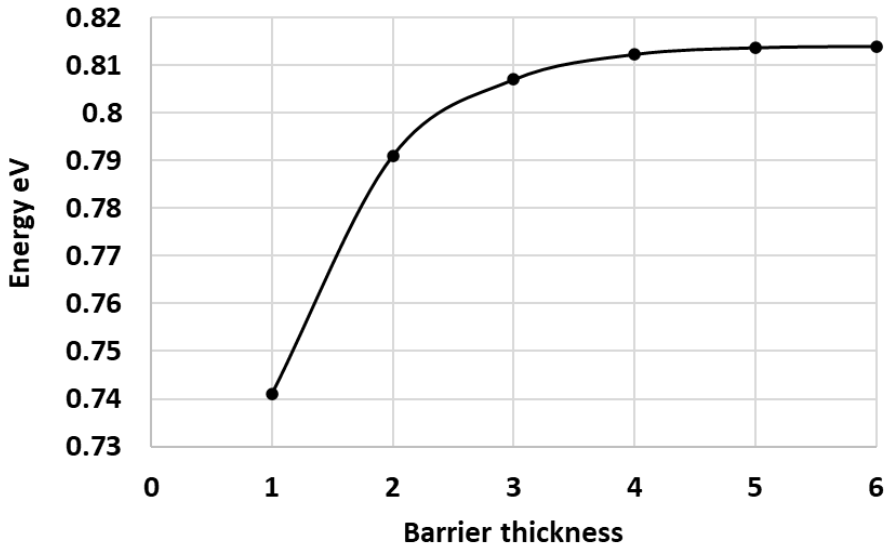

Figure 6.1 simulated Type-I transition energy varying the barrier thickness

Bibliography

1. Nagatsuma, T., *Terahertz technologies: present and future.* IEICE Electronics Express, 2011. **8**(14): p. 1127-1142.
2. Elayan, H., et al., *Terahertz band: The last piece of RF spectrum puzzle for communication systems.* IEEE Open Journal of the Communications Society, 2019. **1**: p. 1-32.
3. Kürner, T., D. Mittleman, and T. Nagatsuma, *THz Communications: Paving the Way Towards Wireless Tbps*. 2022: Springer.
4. Ito, H., et al., *High-speed and high-output InP-InGaAs unitraveling-carrier photodiodes.* IEEE Journal of selected topics in quantum electronics, 2004. **10**(4): p. 709-727.
5. Koenig, S., et al. *Wireless sub-THz communication system with high data rate enabled by RF photonics and active MMIC technology*. in *2014 IEEE Photonics Conference*. 2014. IEEE.
6. Izumi, R., S. Suzuki, and M. Asada. *1.98 THz resonant-tunneling-diode oscillator with reduced conduction loss by thick antenna electrode*. in *2017 42nd International Conference on Infrared, Millimeter, and Terahertz Waves (IRMMW-THz)*. 2017. IEEE.
7. Nagatsuma, T., et al. *300-GHz-band wireless transmission at 50 Gbit/s over 100 meters*. in *2016 41st international conference on infrared, Millimeter, and terahertz waves (IRMMW-THz)*. 2016. IEEE.
8. Shannon, C.E., *Communication in the presence of noise.* Proceedings of the IRE, 1949. **37**(1): p. 10-21.
9. Sun, Q., et al., *Recent advances in terahertz technology for biomedical applications.* Quantitative imaging in medicine and surgery, 2017. **7**(3): p. 345.
10. Kemp, M.C., et al. *Security applications of terahertz technology*. in *Terahertz for military and security applications*. 2003. SPIE.
11. Committee, I.L.M.S., *IEEE standard for high data rate wireless multi-media networks–amendment 2: 100 Gb/s wireless switched point-to-point physical layer.* IEEE Std. **802**: p. 1-55.
12. Cimbri, D. and E. Wasige, *Terahertz Communications with Resonant Tunnelling Diodes: Status and Perspectives*, in *Next Generation Wireless Terahertz Communication Networks*. 2021, CRC Press. p. 25-87.
13. Cherry, S., *Edholm's law of bandwidth.* IEEE spectrum, 2004. **41**(7): p. 58-60.
14. Preu, S., et al., *Tunable, continuous-wave terahertz photomixer sources and applications.* Journal of Applied Physics, 2011. **109**(6): p. 4.
15. Safian, R., G. Ghazi, and N. Mohammadian, *Review of photomixing continuous-wave terahertz systems and current application trends in terahertz domain.* Optical Engineering, 2019. **58**(11): p. 110901.
16. Deninger, A.J., et al., *2.75 THz tuning with a triple-DFB laser system at 1550 nm and InGaAs photomixers.* Journal of Infrared, Millimeter, and Terahertz Waves, 2015. **36**(3): p. 269-277.
17. Kim, N., et al., *Distributed feedback laser diode integrated with distributed Bragg reflector for continuous-wave terahertz generation.* Optics Express, 2012. **20**(16): p. 17496-17502.
18. Haidar, M.T., et al., *Systematic characterization of a 1550 nm microelectromechanical (MEMS)-tunable vertical-cavity surface-emitting laser (VCSEL) with 7.92 THz tuning range for terahertz photomixing systems.* Journal of Applied Physics, 2018. **123**(2): p. 023106.
19. Ravaro, M., et al., *Phase-locking of a 2.5 THz quantum cascade laser to a frequency comb using a GaAs photomixer.* Optics letters, 2011. **36**(20): p. 3969-3971.
20. Shiode, T., et al. *Giga-bit wireless communication at 300 GHz using resonant tunneling diode detector*. in *Asia-Pacific Microwave Conference 2011*. 2011. IEEE.
21. Ishibashi, T., et al. *Uni-traveling-carrier photodiodes*. in *Ultrafast Electronics and Optoelectronics*. 1997. Optical Society of America.

22. Wakatsuki, A., Y. Muramoto, and T. Ishibashi, *Development of terahertz-wave photomixer module using a uni-traveling-carrier photodiode.* NTT Technical Review, 2012. **10**(2).
23. Song, H.-J., et al., *Uni-travelling-carrier photodiode module generating 300 GHz power greater than 1 mW.* IEEE Microwave and Wireless Components Letters, 2012. **22**(7): p. 363-365.
24. Boyd, R.W., *Nonlinear optics*. 2020: Academic press.
25. Hebling, J., et al., *High-power THz generation, THz nonlinear optics, and THz nonlinear spectroscopy.* IEEE Journal of Selected Topics in Quantum Electronics, 2008. **14**(2): p. 345-353.
26. Nakanishi, A., et al., *Temperature-insensitive imaging properties of a broadband terahertz nonlinear quantum cascade laser.* Applied Sciences, 2020. **10**(17): p. 5926.
27. Leahy-Hoppa, M.R., et al., *Ultrafast laser-based spectroscopy and sensing: applications in LIBS, CARS, and THz spectroscopy.* Sensors, 2010. **10**(5): p. 4342-4372.
28. Lee, H.-J., et al. *Intel 22nm FinFET (22FFL) process technology for RF and mm wave applications and circuit design optimization for FinFET technology*. in *2018 IEEE International Electron Devices Meeting (IEDM)*. 2018. IEEE.
29. Mei, X., et al., *First demonstration of amplification at 1 THz using 25-nm InP high electron mobility transistor process.* IEEE Electron Device Letters, 2015. **36**(4): p. 327-329.
30. Heinemann, B., et al. *SiGe HBT with fx/fmax of 505 GHz/720 GHz*. in *2016 IEEE International Electron Devices Meeting (IEDM)*. 2016. IEEE.
31. Rode, J.C., et al., *Indium phosphide heterobipolar transistor technology beyond 1-THz bandwidth.* IEEE Transactions on Electron Devices, 2015. **62**(9): p. 2779-2785.
32. Nishizawa, J., et al., *706-GHz GaAs CW fundamental-mode TUNNETT diodes fabricated with molecular layer epitaxy.* physica status solidi c, 2008. **5**(9): p. 2802-2804.
33. Nishizawa, J.-i., et al., *GaAs TUNNETT diodes oscillating at 430-655 GHz in CW fundamental mode.* IEEE microwave and wireless components letters, 2005. **15**(9): p. 597-599.
34. Ino, M., T. Ishibashi, and M. Ohmori, *CW oscillation with p+-p-n+ silicon IMPATT diodes in 200 GHz and 300 GHz bands.* Electronics letters, 1976. **12**(6): p. 148-149.
35. Eisele, H., *Second-harmonic power extraction from InP Gunn devices with more than 1 mW in 260-320 GHz frequency range.* Electronics Letters, 1998. **34**(25): p. 2412-2413.
36. Eisele, H., A. Rydberg, and G.I. Haddad, *Recent advances in the performance of InP Gunn devices and GaAs TUNNETT diodes for the 100-300-GHz frequency range and above.* IEEE Transactions on Microwave Theory and Techniques, 2000. **48**(4): p. 626-631.
37. Suzuki, S., et al., *Fundamental oscillation of resonant tunneling diodes above 1 THz at room temperature.* Applied Physics Letters, 2010. **97**(24): p. 242102.
38. Asada, M. and S. Suzuki, *Terahertz emitter using resonant-tunneling diode and applications.* Sensors, 2021. **21**(4): p. 1384.
39. Baba, R., et al., *Epitaxial Designs for Maximizing Efficiency in Resonant Tunneling Diode Based Terahertz Emitters.* IEEE Journal of Quantum Electronics, 2018. **54**(2): p. 1-11.
40. Kim, C. and A. Brandli, *High-frequency high-power operation of tunnel diodes.* IRE Transactions on Circuit Theory, 1961. **8**(4): p. 416-425.
41. Jacobs, K., et al., *Valley current characterization of high current density resonant tunnelling diodes for terahertz-wave applications.* AIP Advances, 2017. **7**(10): p. 105316.
42. Bruno, J.D. and J. Hurley, *Effect of interface roughness on the current-voltage characteristic of a resonant tunneling diode.* Superlattices and microstructures, 1992. **11**(1): p. 23-26.
43. Kanaya, H., et al., *Fundamental oscillation up to 1.31 THz in resonant tunneling diodes with thin well and barriers.* Applied Physics Express, 2012. **5**(12): p. 124101.
44. Feiginov, M., et al., *Operation of resonant-tunneling diodes with strong back injection from the collector at frequencies up to 1.46 THz.* Applied Physics Letters, 2014. **104**(24): p. 243509.
45. Cimbri, D., et al., *Resonant Tunnelling Diodes High-Speed Terahertz Wireless Communications-A Review.* IEEE Transactions on Terahertz Science and Technology, 2022.

46. Sugiyama, H., et al., *Metal-organic vapor-phase epitaxy growth of InP-based resonant tunneling diodes with a strained In0. 8Ga0. 2As well and AlAs barriers.* Japanese journal of applied physics, 2005. **44**(10R): p. 7314.
47. Sugiyama, H., et al., *Extremely high peak current densities of over 1× 106 A/cm2 in InP-based InGaAs/AlAs resonant tunneling diodes grown by metal–organic vapor-phase epitaxy.* Japanese Journal of Applied Physics, 2010. **49**(5R): p. 051201.
48. Yachmenev, A.E., et al., *Arsenides-and related III-V materials-based multilayered structures for terahertz applications: Various designs and growth technology.* Progress in Crystal Growth and Characterization of Materials, 2020: p. 100485.
49. Cito, M., et al., *Photoluminescence excitation spectroscopy for structural and electronic characterization of resonant tunneling diodes for THz applications.* AIP Advances, 2021. **11**(3): p. 035122.
50. Huang, C., et al., *AlGaAs/GaAs double barrier diodes with high peak-to-valley current ratio.* Applied physics letters, 1987. **51**(2): p. 121-123.
51. Shewchuk, T., et al., *Resonant tunneling oscillations in a GaAs-Al x Ga1− x As heterostructure at room temperature.* Applied physics letters, 1985. **46**(5): p. 508-510.
52. Zhang, W., et al., *Fabrication and Characterization of GaN/AlN Resonant Tunneling Diodes.* High-Frequency GaN Electronic Devices, 2020: p. 249-281.
53. Aardvark, A., N. Mason, and P. Walker, *The growth of antimonides by MOVPE.* Progress in crystal growth and characterization of materials, 1997. **35**(2-4): p. 207-241.
54. Jacobs, K., et al., *A dual-pass high current density resonant tunneling diode for terahertz wave applications.* IEEE Electron Device Letters, 2015. **36**(12): p. 1295-1298.
55. Sollner, T., et al., *Quantum well oscillators.* Applied physics letters, 1984. **45**(12): p. 1319-1321.
56. Brown, E.R., et al., *Oscillations up to 712 GHz in InAs/AlSb resonant-tunneling diodes.* Applied Physics Letters, 1991. **58**(20): p. 2291-2293.
57. Yu, X., et al., *Highly efficient resonant tunneling diode terahertz oscillator with a split ring resonator.* IEEE Electron Device Letters, 2021. **42**(7): p. 982-985.
58. Orihashi, N., et al., *Experimental and theoretical characteristics of sub-terahertz and terahertz oscillations of resonant tunneling diodes integrated with slot antennas.* Japanese Journal of Applied Physics, 2005. **44**(11R): p. 7809.
59. Kasagi, K., S. Suzuki, and M. Asada, *Large-scale array of resonant-tunneling-diode terahertz oscillators for high output power at 1 THz.* Journal of Applied Physics, 2019. **125**(15): p. 151601.
60. Suzuki, S., et al., *Fundamental oscillation of up to 831 GHz in GaInAs/AlAs resonant tunneling diode.* Applied Physics Express, 2009. **2**(5): p. 054501.
61. Feiginov, M., *Frequency limitations of resonant-tunnelling diodes in sub-THz and THz oscillators and detectors.* Journal of infrared, millimeter, and terahertz waves, 2019. **40**(4): p. 365-394.
62. Sugiyama, H., et al., *Structural and electrical transport properties of MOVPE-grown pseudomorphic AlAs/InGaAs/InAs resonant tunneling diodes on InP substrates.* Japanese Journal of Applied Physics, 2014. **53**(3): p. 031202.
63. Jacobs, K.J., B.J. Stevens, and R.A. Hogg, *Photoluminescence Characterisation of High Current Density Resonant Tunnelling Diodes for Terahertz Applications.* IEICE Transactions on Electronics, 2016. **99**(2): p. 181-188.
64. Jacobs, K., et al., *Non-destructive mapping of doping and structural composition of MOVPE-grown high current density resonant tunnelling diodes through photoluminescence spectroscopy.* Journal of Crystal Growth, 2015. **418**: p. 102-110.
65. Yamanaka, K., et al., *Photocurrent spectroscopy in GaAs/AlGaAs multiple quantum wells under a high electric field perpendicular to the heterointerface.* Applied physics letters, 1986. **48**(13): p. 840-842.

66. Cardona, M. and R. Merlin, *Light scattering in solids IX*, in *Light Scattering in Solid IX*. 2006, Springer. p. 1-14.
67. Bimberg, D., et al., *Cathodoluminescence atomic scale images of monolayer islands at GaAs/GaAlAs interfaces.* Journal of Vacuum Science & Technology B: Microelectronics Processing and Phenomena, 1987. **5**(4): p. 1191-1197.
68. Christen, J., M. Grundmann, and D. Bimberg, *Scanning cathodoluminescence microscopy: A unique approach to atomic-scale characterization of heterointerfaces and imaging of semiconductor inhomogeneities.* Journal of Vacuum Science & Technology B: Microelectronics and Nanometer Structures Processing, Measurement, and Phenomena, 1991. **9**(4): p. 2358-2368.
69. Fewster, P.F., *Reciprocal space mapping.* Critical Reviews in Solid State and Material Sciences, 1997. **22**(2): p. 69-110.
70. Pereira, S., et al., *Strain and composition distributions in wurtzite InGaN/GaN layers extracted from x-ray reciprocal space mapping.* Applied physics letters, 2002. **80**(21): p. 3913-3915.
71. Cito, M., et al. *PL and PLE characterization of high current density resonant tunnelling diodes for THz applications*. in *Terahertz, RF, Millimeter, and Submillimeter-Wave Technology and Applications XV*. 2022. SPIE.
72. Cimbri, D., et al., *Modeling of High-Power Resonant Tunneling Diodes through the Non-Equilibrium Green's Function Method.* 2021.
73. Cito, M., et al., *Micro-PL analysis of high current density resonant tunneling diodes for THz applications.* Applied Physics Letters, 2021. **119**(7): p. 072102.
74. Baba, R., et al., *Non-destructive characterization of thin layer resonant tunneling diodes.* Journal of Applied Physics, 2019. **126**(12): p. 124304.
75. Cito, M., et al. *Fitting of photoluminescence spectra for structural characterisation of high current density resonant tunnelling diodes for THz applications*. in *Terahertz, RF, Millimeter, and Submillimeter-Wave Technology and Applications XIV*. 2021. International Society for Optics and Photonics.
76. Grober, R.D., et al., *Design and implementation of a low temperature near-field scanning optical microscope.* Review of scientific instruments, 1994. **65**(3): p. 626-631.
77. Skolnick, M., et al., *Optical spectroscopy of double barrier resonant tunneling structures.* Physica Scripta, 1991. **1991**(T39): p. 271.
78. Higuera-Rodriguez, A., et al., *Ultralow surface recombination velocity in passivated InGaAs/InP nanopillars.* Nano letters, 2017. **17**(4): p. 2627-2633.
79. Ledentsov, N., et al., *Radiative states in type-II GaSb/GaAs quantum wells.* Physical Review B, 1995. **52**(19): p. 14058.
80. Jacobs, K.J., et al. *Characterisation of high current density resonant tunnelling diodes for THz emission using photoluminescence spectroscopy*. in *2016 41st International Conference on Infrared, Millimeter, and Terahertz waves (IRMMW-THz)*. 2016. IEEE.
81. Ekins-Daukes, N., K. Kawaguchi, and J. Zhang, *Strain-balanced criteria for multiple quantum well structures and its signature in X-ray rocking curves.* Crystal Growth & Design, 2002. **2**(4): p. 287-292.
82. Jain, S., M. Willander, and H. Maes, *Stresses and strains in epilayers, stripes and quantum structures of III-V compound semiconductors.* Semiconductor science and technology, 1996. **11**(5): p. 641.
83. Landgren, G., J. Wallin, and S. Pellegrino, *Optimal growth interrupts for very high quality InGaAs (P)/InP superlattices grown by MOVPE.* Journal of electronic materials, 1992. **21**(1): p. 105-108.
84. Baba, R., et al. *Characterisation of thin-layer resonant tunnelling diodes grown by MOVPE*. in *Quantum Dots and Nanostructures: Growth, Characterization, and Modeling XVI*. 2019. International Society for Optics and Photonics.

85. Vilkotskii, V., et al., *Burstein-Moss effect and near-band-edge luminescence spectrum of highly doped indium arsenide.* physica status solidi (b), 1979. **91**(1): p. 71-81.
86. Birner, S., et al., *Nextnano: general purpose 3-D simulations.* IEEE Transactions on Electron Devices, 2007. **54**(9): p. 2137-2142.
87. Vurgaftman, I., J.á. Meyer, and L.á. Ram-Mohan, *Band parameters for III–V compound semiconductors and their alloys.* Journal of applied physics, 2001. **89**(11): p. 5815-5875.
88. Sugiyama, Y., et al., *Conduction Band Edge Discontinuity of In0. 52Ga0. 48As/In0. 52 (Ga1-xAlx) 0.48 As (0≦x≦1) Heterostructures.* Japanese journal of applied physics, 1986. **25**(8A): p. L648.
89. Van de Walle, C.G., *Band lineups and deformation potentials in the model-solid theory.* Physical review B, 1989. **39**(3): p. 1871.
90. Duggan, G., *A critical review of heterojunction band offsets.* Journal of Vacuum Science & Technology B: Microelectronics Processing and Phenomena, 1985. **3**(4): p. 1224-1230.
91. Dawson, M.D. and G. Duggan, *Exciton localization effects and heterojunction band offset in (Ga, In) P-(Al, Ga, In) P multiple quantum wells.* Physical Review B, 1993. **47**(19): p. 12598.
92. Brasil, M., et al., *Roughness at the interface of thin InP/InAs quantum wells.* Applied physics letters, 1993. **63**(19): p. 2688-2690.
93. Herman, M., D. Bimberg, and J. Christen, *Heterointerfaces in quantum wells and epitaxial growth processes: Evaluation by luminescence techniques.* Journal of Applied Physics, 1991. **70**(2): p. R1-R52.
94. Singh, J. and K. Bajaj, *Role of interface roughness and alloy disorder in photoluminescence in quantum-well structures.* Journal of applied physics, 1985. **57**(12): p. 5433-5437.
95. Fernando, J.G. and A.S. Somintac, *X-Ray Diffraction Analysis of Strained IngaAs/GaAs Superlattices Grown on GaAs (001) Substrates Via Molecular Beam Epitaxy.* WMSU Research Journal, 2011. **30**(1): p. 1-1.
96. Pickering, C., et al., *Non-destructive characterisation of (Ga, In, Al, As, P)-based ternary multilayer structures using spectroscopic ellipsometry.* Applied surface science, 1991. **50**(1-4): p. 346-352.
97. Nittono, T., S. Sugitani, and F. Hyuga, *Photoluminescence characterization of InGaP/GaAs heterostructures grown by metalorganic chemical vapor deposition.* Journal of applied physics, 1995. **78**(9): p. 5387-5390.
98. Velling, P., et al., *InAlAs/InGaAs/InP heterostructures for RTD and HBT device applications grown by LP-MOVPE using non-gaseous sources.* Journal of crystal growth, 2000. **221**(1-4): p. 722-729.
99. Gozu, S.-i., et al., *Critical layer thickness study in In0. 75Ga0. 25As/In0. 5Al0. 5As pseudomorphic resonant tunneling diode structure grown on GaAs substrates.* Journal of crystal growth, 2001. **227**: p. 161-166.
100. Dingle, R., W. Wiegmann, and C.H. Henry, *Quantum states of confined carriers in very thin Al x Ga 1− x As-GaAs-Al x Ga 1− x As heterostructures.* Physical Review Letters, 1974. **33**(14): p. 827.
101. Kroemer, H., *Band offsets at heterointerfaces: Theoretical basis, and review of recent experimental work.* Surface Science, 1986. **174**(1-3): p. 299-306.
102. Bhattacharya, P., *Properties of lattice-matched and strained indium gallium arsenide*. 1993: IET.
103. Fobelets, K., et al., *Determination of the band line-up for strained InGaAs/AlAs heterojunctions using resonant tunnelling diodes.* Superlattices and microstructures, 1992. **11**(1): p. 27-29.
104. Jogai, B. and P. Yu, *Energy levels of strained In x Ga 1− x As-GaAs superlattices.* Physical Review B, 1990. **41**(18): p. 12650.
105. Skolnick, M., et al., *Investigation of InGaAs-InP quantum wells by optical spectroscopy.* Semiconductor science and technology, 1986. **1**(1): p. 29.
106. Fox, M., *Optical properties of solids*. 2002, American Association of Physics Teachers.

107. Zheng, J., et al., *Interface segregation and clustering in strained-layer InGaAs/GaAs heterostructures studied by cross-sectional scanning tunneling microscopy.* Physical review letters, 1994. **72**(15): p. 2414.
108. Cito, M., et al. *Micro-photoluminescence characterisation of structural disorder in resonant tunneling diodes for THz applications*. in *Low-Dimensional Materials and Devices 2021*. 2021. International Society for Optics and Photonics.
109. Alexandre, F., et al., *GaAs/Ga1− xAlxAs and Ga1− xAlxAs/GaAs heterointerfaces grown by molecular beam epitaxy.* Surface Science, 1986. **168**(1-3): p. 454-461.
110. Cho, N.M., et al., *Realization of high mobility in inverted Al x Ga1− x As/GaAs heterojunctions.* Applied physics letters, 1988. **52**(24): p. 2037-2039.
111. Singh, J. and K. Bajaj, *Role of thin multiquantum wells in controlling intrinsic interface quality in molecular beam epitaxially grown heterostructures.* Applied physics letters, 1985. **47**(6): p. 594-596.
112. Chen, H., et al., *Effect of substrate tilting on molecular beam epitaxial grown AlGaAs/GaAs lasers having very low threshold current densities.* Applied physics letters, 1987. **51**(25): p. 2094-2096.
113. Bimberg, D., et al., *Kinetics of island formation at the interfaces of AlGaAs/GaAs/AlGaAs quantum wells upon growth interruption.* Superlattices and Microstructures, 1987. **3**(1): p. 79-82.
114. Chand, N. and S. Chu, *Origin and improvement of interface roughness in AlGaAs/GaAs heterostructures grown by molecular beam epitaxy.* Applied physics letters, 1990. **57**(17): p. 1796-1798.
115. Petroff, P., et al., *Impurity trapping, interface structure, and luminescence of GaAs quantum wells grown by molecular beam epitaxy.* Applied physics letters, 1984. **44**(2): p. 217-219.
116. Seifert, W., et al., *Analysis of growth conditions for the deposition of monolayers of GaInAs, GaAs and InAs in InP by LP-MOVPE.* Journal of crystal growth, 1992. **124**(1-4): p. 531-535.
117. Taira, K., et al., *Noninteger InAs monolayer well InAs/GaAs single quantum well structures grown by metalorganic chemical vapor deposition.* Applied physics letters, 1988. **53**(6): p. 495-496.
118. Gustafsson, A. and E. Kapon, *Cathodoluminescence in the scanning electron microscope: application to low-dimensional semiconductor structures.* Scanning Microsc, 1998. **12**(2): p. 285-299.
119. Solomon, G., J. Trezza, and J. Harris Jr, *Substrate temperature and monolayer coverage effects on epitaxial ordering of InAs and InGaAs islands on GaAs.* Applied physics letters, 1995. **66**(8): p. 991-993.
120. Horikoshi, Y., M. Kawashima, and H. Yamaguchi, *Migration-enhanced epitaxy of GaAs and AlGaAs.* Japanese journal of applied physics, 1988. **27**(2R): p. 169.
121. Schaffer, W., et al., *Nucleation and strain relaxation at the InAs/GaAs (100) heterojunction.* Journal of Vacuum Science & Technology B: Microelectronics Processing and Phenomena, 1983. **1**(3): p. 688-695.
122. Leonard, D., et al., *Direct formation of quantum-sized dots from uniform coherent islands of InGaAs on GaAs surfaces.* Applied Physics Letters, 1993. **63**(23): p. 3203-3205.
123. Matthews, J. and A. Blakeslee, *Defects in epitaxial multilayers: I. Misfit dislocations.* Journal of Crystal growth, 1974. **27**: p. 118-125.
124. People, R. and J. Bean, *Calculation of critical layer thickness versus lattice mismatch for Ge x Si1− x/Si strained-layer heterostructures.* Applied Physics Letters, 1985. **47**(3): p. 322-324.
125. Temkin, H., et al., *Critical layer thickness in strained Ga1− x In x As/InP quantum wells.* Applied physics letters, 1989. **55**(16): p. 1668-1670.
126. Holec, D., et al., *Critical thickness calculations for InGaN/GaN.* Journal of Crystal Growth, 2007. **303**(1): p. 314-317.
127. Tabuchi, M., S. Noda, and A. Sasaki, *Strain energy and critical thickness of heteroepitaxial InGaAs layers on GaAs substrate.* Journal of crystal growth, 1991. **115**(1-4): p. 169-173.

128. Doi, T., et al., *Strain-compensated effect on the growth of InGaN/AlGaN multi-quantum well by metalorganic vapor phase epitaxy.* Japanese Journal of Applied Physics, 2013. **52**(8S): p. 08JB14.
129. Miller, B., et al., *Strain-compensated strained-layer superlattices for 1.5 μm wavelength lasers.* Applied physics letters, 1991. **58**(18): p. 1952-1954.
130. Dries, J.C., et al., *Strain compensated In 1− x Ga x As (x< 0.47) quantum well photodiodes for extended wavelength operation.* Applied physics letters, 1998. **73**(16): p. 2263-2265.
131. Porte, L., *Stress and surface energies versus surface nanostructuring: the InGaAs/InP (0 0 1) epitaxial system.* Journal of crystal growth, 2004. **273**(1-2): p. 136-148.
132. Tu, Y. and J. Tersoff, *Origin of apparent critical thickness for island formation in heteroepitaxy.* Physical review letters, 2004. **93**(21): p. 216101.
133. Tersoff, J. and F. LeGoues, *Competing relaxation mechanisms in strained layers.* Physical review letters, 1994. **72**(22): p. 3570.
134. Nabetani, Y., et al., *Island formation of InAs grown on GaAs.* Journal of crystal growth, 1995. **146**(1-4): p. 363-367.
135. Gobato, Y.G., et al., *Spectroscopy of growth islands in G a A s/I n 0.1 Ga 0.9 A s/A l A s double-barrier structures from photoluminescence and resonant tunneling studies.* Physical Review B, 1999. **60**(8): p. 5664.
136. Cimbri, D., et al. *In 0.53 Ga 0.47 As/AlAs Double-Barrier Resonant Tunnelling Diodes With High-Power Performance in the Low-Terahertz Band*. in *2022 Fifth International Workshop on Mobile Terahertz Systems (IWMTS)*. 2022. IEEE.
137. Muraki, K., et al., *Surface segregation of In atoms during molecular beam epitaxy and its influence on the energy levels in InGaAs/GaAs quantum wells.* Applied Physics Letters, 1992. **61**(5): p. 557-559.
138. Charreaux, C., G. Guillot, and A. Nouailhat, *Alloy broadening in photoluminescence spectra of Ga0. 47In0. 53As.* Journal of applied physics, 1986. **60**(2): p. 768-772.
139. Dimoulas, A., et al., *Alloy disorder effects in III–V ternaries studied by modulation spectroscopy.* Applied surface science, 1991. **50**(1-4): p. 353-358.
140. Houghton, D., M. Davies, and M. Dion, *Design criteria for structurally stable, highly strained multiple quantum well devices.* Applied physics letters, 1994. **64**(4): p. 505-507.
141. Al-Taai, Q.R.A., et al., *Analysis of stability of nano-vs micro-sized resonant tunnelling diode (RTD) devices for future neuromorphic computing applications.* International Journal of Nanoelectronics and Materials, 2021.